Energy system integration of Dynamic Power to Gas systems with 3 Phase Methanation for effective sector coupling.

Zur Erlangung des akademischen Grades eines

DOKTORS DER INGENIEURWISSENSCHAFTEN (DR.-ING.)

von der KIT-Fakultät für Chemieingenieurwesen und Verfahrenstechnik des
Karlsruher Instituts für Technologie (KIT)
genehmigte

DISSERTATION

von

Praseeth Prabhakaran, M.Sc.

aus Thiruvananthapuram, Indien

Tag der mündlichen Prüfung: 8.12.2025
Erstgutachter: Prof. Dr.-Ing. Thomas Kolb
Zweitgutachter: Prof. Dr. Veit Hagenmeyer

Abstract

This work aims to develop an integrated energy system for analysing sector coupling in de-central energy systems. To achieve this, a dynamic numerical model of the de-central energy system has been developed with the aim of integrating different renewable energy sources and consumption sectors, including buildings, mobility and industry. The numerical model includes several components from the electricity, gas and heating sectors. Some of these components have already been described in the literature. Of the required numerical components, one that is of particular importance but missing from the existing literature is the three-phase methanation reactor (3-PM). Therefore, a dynamic numerical model of the 3-PM process was developed using the axial dispersion method. Thermodynamic and mathematical adaptations were made to ensure compatibility of the model with other models in the energy system. In addition to methanation, this work addresses the modelling and grouping of buildings. This is achieved by first developing standard load profiles for different building types. The standard load profiles are then integrated with different heating systems into building energy systems to enable flexible variation of building types, heating systems and energy sources. The newly modelled numerical components, together with existing components from the literature like the electrical, gas and district heating networks, various forms of storage and control systems, were then integrated into a comprehensive energy system. In order to address the issue of spatio-temporal complexity in this overall energy system, a co-simulation interface was developed to couple dynamic system models with high-resolution gas, power and district heating networks. The overall energy system was then simulated under a series of prospective energy scenarios, including those in which gases such as SNG and hydrogen assume a more prominent role or those where a significant proportion of electrification becomes a more likely outcome. This was complemented by location-specific parameter studies to evaluate the efficacy of molecule-based storage strategies and compare them to purely electrical approaches. The results highlight the critical importance of molecule-based storage and sector coupling strategies and compare them to purely electrical approaches specific to a de-central energy system. Furthermore, the sector coupling tool developed in this work offers customisation capabilities to simulate future de-central energy systems effectively under different energy scenarios.

Kurzfassung

Ziel dieser Arbeit ist die Entwicklung eines integrierten Energiesystems zur Analyse der Sektorkopplung in dezentralen Energiesystemen. Zu diesem Zweck wurde ein dynamisches numerisches Modell des dezentralen Energiesystems entwickelt, das verschiedene erneuerbare Energiequellen und Verbrauchssektoren wie Gebäude, Mobilität und Industrie integriert. Das numerische Modell umfasst mehrere Komponenten aus den Bereichen Strom, Gas und Wärme. Einige dieser Komponenten wurden bereits in der Literatur beschrieben. Von den erforderlichen numerischen Komponenten fehlt jedoch in der vorhandenen Literatur der Dreiphasen-Methanisierungsreaktor (3-PM). Daher wurde ein dynamisches numerisches Modell des 3-PM-Prozesses mit Hilfe der axialen Dispersionsmethode entwickelt. Thermodynamische und mathematische Anpassungen wurden vorgenommen, um die Kompatibilität des Modells mit anderen Modellen des Energiesystems zu gewährleisten. Neben der Methanisierung befasst sich diese Arbeit mit der Modellierung und Gruppierung von Gebäuden. Dazu werden zunächst Standardlastprofile für verschiedene Gebäudetypen entwickelt. Die Standardlastprofile werden dann in Gebäudeenergiesysteme mit verschiedenen Heizsystemen integriert, um eine flexible Variation von Gebäudetypen, Heizsystemen und Energiequellen zu ermöglichen. Die neu modellierten numerischen Komponenten werden dann zusammen mit bestehenden Komponenten aus der Literatur wie Strom-, Gas- und Fernwärmenetzen, verschiedenen Speicherarten und Steuerungssystemen in ein umfassendes Energiesystem integriert. Um die raum-zeitliche Komplexität in diesem Gesamtenergiesystem zu lösen, wurde eine Co-Simulationsschnittstelle entwickelt, um dynamische Systemmodelle mit hochaufgelösten Gas-, Strom- und Wärmenetzen zu koppeln. Das Gesamtenergiesystem wurde dann unter einer Reihe von prospektiven Energieszenarien simuliert, einschließlich solcher, in denen Gase wie SNG und Wasserstoff eine größere Rolle spielen oder in denen ein erheblicher Anteil an Elektrifizierung wahrscheinlicher ist. Ergänzt wurde dies durch standortspezifische Parameterstudien, um die Effizienz molekülbasierter Speicherstrategien zu bewerten und mit rein elektrischen Ansätzen zu vergleichen. Die Ergebnisse unterstreichen die wesentliche Bedeutung von molekülbasierten Speicher- und Sektorkopplungsstrategien und vergleichen diese mit rein elektrischen Ansätzen, spezifisch für ein dezentrales Energiesystem. Darüber hinaus bietet das in dieser Arbeit entwickelte Sektorkopplungstool Anpassungsmöglichkeiten, um zukünftige dezentrale Energiesysteme unter verschiedenen Energieszenarien effektiv zu simulieren.

Acknowledgement

I want to express my sincere gratitude to my primary supervisor, Prof. Dr.-Ing Thomas Kolb, who gave me this opportunity and for his support. I also thank Dr.-Ing Frank Graf and Dipl-Ing Wolfgang Köppel for always hand-holding me back to simplicity in complex discussions. I thank Dr.-Ing Christian Schulze (TLK Thermo, Braunschweig) for introducing me to the world of Modelica and simulation of thermodynamic systems. Special gratitude to Prof. Dr.-Ing Gerhard Schmitz (TU Hamburg) for answering all my difficult questions with references even during christmas vacation.

I would also like to thank Dr-Ing Siegfried Bajohr and Prof. Dr-Ing Veit Hagenmeyer for their support. Special regards to Prof Dr. Raghurama Rao (IISc) for hosting me in India and the really late-night discussions on Partial Differential Equations, which helped me overcome some very tricky hurdles. Special thanks to my best friends, Jithin Mohan and Hari, for listening patiently and suggesting ideas in many situations.

I also thank DAAD Scholars Dr. Ushnik Mukherjee (University of Waterloo, Canada) and Gopal Remesh (Exxon Mobil) for assisting me. I also thank Volkan Isik for his help with energy scenario datasets and Christian Hotz for providing valuable feedback. I would also like to acknowledge the funding provided by the Federal Ministry of Education and Research (BMBF), Germany, under the SEKO research project.

Who makes the mind perceive objects?
Who causes vitality?
Under whose will comes speech?
Who sees through my eyes and hears through my ears?

- The disciple asks the teacher.
- Kena Upanishad. Ancient Indian Philosophy

Contents

Acronyms and symbols

Acronyms

Acronym	Description
3-PM	3-Phase Methanation
API	Application Programming Interface
ASHP	Air Source Heat Pumps
ASU	Air Separation Unit
BDEW	Bundesverband der Energie- und Wasserwirtschaft
BES	Building Energy Systems
BEV	Battery Electric Vehicles
BLT	Block Lower Triangular
BMWK	Bundesministerium für Wirtschaft und Klimaschutz (Federal Ministry for Economic Affairs and Climate Action)
BPS	Building Performance Simulations
BW	Baden-Württemberg
CCU	Carbon Capture and Utilisation
CEB	Chemische Energieträger - Brennstofftechnologie
CFD	Computational Fluid Dynamics
CHP	Combined Heat and Power
COP	Coefficient of Performance
COP	Conference of the Parties of the UNFCCC
DAE	Differential Algebraic Equation
DBT	Dibenzyl Toluene
DENA	Deutsche Energie Agentur
DH	District Heating (also used as a sector label)
DOE	Design of Experiment
E-Fuels	Electric (Electro) Fuels, often used synonymously with synthetic fuels
EHB	European Hydrogen Backbone
ENNOH	European Network of Network Operators for Hydrogen
EBI-ceb	Engler Bunte Institut-Chemische Energieträger-Brennstofftechnologie
ECS	Extended Corresponding States
EOS	Equations of State

Continued on next page

Acronym	Description
EU	European Union
EV	Electric Vehicle
FCH	Fuel Cell and Hydrogen Joint Undertaking
FIRC	Flow Indicating Recording Controller
FLH	Full load hours
FMI	Functional Mock-up Interface
FMU	Functional Mock-up Unit
GBA	Bakery
GBD	Other operational services
GBH	Accommodation
GGB	Horticulture
GGA	Restaurants
GHA	Retail and wholesale
GHD	Gewerbe, Handel, Dienstleistung (commercial/services sector)
GHG	Greenhouse Gases
GMK	Metal and automotive
GN	Gas Network
GPD	Paper and print
GSHP	Ground Source Heat Pumps
GWA	Laundries, chemicals, cleanings
GWP	Global Warming Potential
HEF	Single-Family Households (sector label)
HMF	Multi-Family Households (sector label)
HKO	Cooking gas
HP	Heat Pump
HVAC	Heating Ventilation and Air Conditioning
IEA	International Energy Agency
IBPSA	International Building Performance Simulation Association
KIT	Karlsruhe Institute of Technology
LCA	Life Cycle Analysis
LCOE	Levelised Cost of Energy
LFS	Langfristszenarien (Long-Term Scenarios)
LHS	Latin Hypercube Sampling
LOD	Level Of Detail
MOB	Mobility (sector label)
MOP	Measure of Performance
MOSAIK	Co-simulation framework

Continued on next page

Acronym	Description
NRW	Nordrhein-Westfalen (North Rhine-Westphalia)
NTP	Normal temperature and pressure
ODE	Ordinary Differential Equation
OPEX	Operating Expenditure
PCR	Primary Control Reserve
PDE	Partial Differential Equation
PEM	Polymer Electrolyte Membrane
PID	Proportional Integral Derivative
PtG	Power to Gas
PtL	Power to Liquids
PtX	Power to X
PV	Photovoltaic
QIR	Gas Chromatograph (GC)
RED	Renewable Energy Directive
REFPROP	Reference Fluid Thermodynamic and Transport Properties Database
RFNBO	Renewable Fuels of Non-Biological Origin
RMG	Road Map Gas
SCADA	Supervisory Control and Data Acquisition
SLP	Standard Load Profiles
SME	Small and Medium-scale Enterprises
SNG	Synthetic Natural Gas
SOC	State of Charge
SOEC	Solid Oxide Electrolyzer Cell
STANET	Gas and District Heating Grids tool
TMY	Typical Meteorological Year
WSHP	Water Source Heat Pumps
XML	Extensible Markup Language

Latin variables

Symbol	Description	Reference
A_H	Empirical coefficient for Henry's law calculation	A.16
A_{cs}	Column cross-sectional area in m^2	A.9
A_{eff}	Effective coil area in m^2	2.8
a	Specific gas–liquid interfacial area in $m^2\,m^{-3}$	2.3, 2.4, A.1, A.14
a_{cool}	Cooling surface area in m^2	2.8
B_H	Empirical coefficient in K for Henry's law calculation	A.16
C_H	Empirical coefficient in K^2 for Henry's law calculation	A.16
$C_{GL,i}$	Concentration of the species i at gas–liquid interface in $kg\,m^{-3}$	3.1, 3.2
$C_{sl,i}$	Concentration of the species i in the slurry phase in $kg\,m^{-3}$	3.1
$c_{i,g}$	Concentration of species i in gas phase	A.1
$c_{i,L}$	Concentration of species i in liquid phase	A.1
$C_{p,L}$	Specific heat capacity of the liquid in $J\,kg^{-1}\,K^{-1}$	2.8
COP	Coefficient of Performance (–)	4.1, 6.13
CV	Solid volume fraction	A.11, A.3
d_P	Catalyst particle diameter	A.10, A.11, A.3
D_{AB}	Binary diffusion coefficient of A in B in $m^2\,s^{-1}$	A.15
$D_{g,ax}$	Axial dispersion coefficient for gas phase in $m^2\,s^{-1}$	2.3, 2.12, A.1, A.8
$D_{sl,ax}$	Axial dispersion coefficient for slurry phase in $m^2\,s^{-1}$	2.4, 2.9, 2.10
d_O	Sparger-orifice diameter in m	A.12, A.15
E_{def}	Cumulative grid import in MWh	7.2
$E_{\text{def,norm}}$	Normalized annual cumulative grid import	7.3, 7.1
E_{DH}	Annual heat demand from district heating in MWh	6.13, 6.14
$E_{\text{H}_2\text{,dem}}$	Annual H_2 demand in MWh	7.4
$E_{\text{SNG,dem}}$	Annual SNG demand in MWh	7.4
$E_{\text{H}_2\text{,gen}}$	Cumulative H_2 production in MWh	7.4, 7.5
$E_{\text{SNG,gen}}$	Cumulative SNG production in MWh	7.4, 7.5

Continued on next page

Symbol	Description	Reference
$E_{\text{annual,el}}$	Total annual electricity demand in MWh (region)	6.4, 6.5
$E_{\text{annual,heat}}$	Total annual heat demand in MWh (region)	6.2, 6.3
E_{norm}	Normalised energy value (–)	6.27
$E_{s,ec,\text{annual,heat}}$	Annual heat demand in MWh for sector s and carrier ec	6.10
$E_{s,\text{annual,heat}}$	Annual heat demand in MWh for sector s	6.8
$E_{s,\text{annual,heat–H2}}$	Annual H_2 demand in MWh for sector s	6.11
$E_{s,\text{annual,heat–SNG}}$	Annual SNG demand in MWh for sector s	6.11
$E_{s,\text{annual,heat–el}}$	Annual heat demand in MWh for sector s using electric heating	6.11
$E_{s,\text{annual,el}}$	Annual electricity demand in MWh for sector s	6.5
E_{surp}	Cumulative grid feed-in in MWh	7.1
$E_{\text{surp,norm}}$	Normalized annual cumulative grid feed-in	7.3, 7.1
$\text{error}_{s,ec}$	Relative load-profile error (%)	6.20, 6.21
FLH	Full load hours in h	6.13
h	Specific enthalpy in $\text{J}\,\text{kg}^{-1}$	1.8, 1.15, 1.19, 1.20
H	Total enthalpy in J	1.14, 1.15
$\dot{H}$	Enthalpy flow rate in W	1.17, 1.18
H_i	Henry's-law coefficient for species i in $\text{Pa}\,\text{m}^3\,\text{mol}^{-1}$	3.2
$H_{i,cc}$	Dimensionless Henry's-law constant	2.3, 2.4,A.1, A.8, A.16
h_{SLP}	Standard load profile function	4.5
i	Electric current in A	1.1
JVP	Yearly load demand in kW h	4.5
K	Empirical lumping factor in the 3-PM kinetic rate (–)	A.17
K_d	Distributor (sparger) constant (–)	A.12
k_L	Liquid-side mass-transfer coefficient in $\text{m}\,\text{s}^{-1}$	2.3, A.1, A.8
$k_L a$	Volumetric gas–liquid mass-transfer coefficient in s^{-1}	A.15
M_i	Species molecular mass in $\text{kg}\,\text{mol}^{-1}$	2.4, 3.2
MW	Mean molecular weight of the liquid mixture in $\text{g}\,\text{mol}^{-1}$	A.10, A.3
m	Mass in kg	1.7, 1.8
$\dot{m}$	Mass flow rate in $\text{kg}\,\text{s}^{-1}$	1.7, 1.8, 1.1
m_{cat}	Mass of catalyst in kg	2.4, 2.8, 3.1

Continued on next page

Symbol	Description	Reference
$\vec{m}_g$	Species-mass vector in gas phase	2.3
$\vec{m}_{sl}$	Species-mass vector in slurry phase	2.4
N	Number of variables in the matrix (–)	1.3
n_{cells}	Number of cells in the spatial grid	2.21
N_O	Number of sparger orifices (–)	A.12, A.13, A.3
N_{EV}	Number of electric vehicles in the region (–)	6.5
$n_{BES(i)}$	Number of building-energy systems per profile	5.2
$n_{EV(i)}$	Number of EVs in the region	5.1
n_{ec}	Units or share allocation for carrier ec in sector s	6.17
n_s	Number of units/buildings in sector s	6.9, 6.18
n_{total}	Total number of buildings in the region	6.9, 6.18
p	Pressure in Pa	1.11, 1.12, 1.13, 1.1
$\vec{p}$	Parameter vector	1.3
$P(t)$	Power at a given time t	6.16, 6.25
p_i	Partial pressure of the species i in Pa	3.2
$P_{CHP,el}$	Electric power from CHP in MW	6.24
P_{def}	Power deficit in MW	6.24
$P_{EV}(t)$	Time-dependent charging profile of a single EV	6.5
P_i	Standard load profile corresponding to building or mobility type i	6.16
P_{met}	Installed methanation-plant capacity in MW	6.23, 4.3, 6.24, 7.5
$P_{\mathrm{met,median}}$	Median methanation capacity in GW	7.1
$P_{mobility}(t)$	Total EV charging demand at time t	6.19
P_{PtG}	Power-to-Gas plant capacity	5.3
$P_{\mathrm{PV,median}}$	Median PV capacity in GW	7.1
P_S	Static bed pressure in Pa	A.11
P_{surp}	Power surplus in MW	6.24, 7.1
P_T	Total bubble-bed pressure in Pa	A.11
P_{wind}	Installed on-shore/off-shore wind-turbine capacity in MW	7.1, 6.2
$P_{\mathrm{wind,median}}$	Median wind capacity in GW	7.1
P_{DH}	Installed district-heating capacity in MW	6.13
P_{ely}	Electrolyser capacity in MW	6.23, 4.3, 6.24, 7.5
$P_{\mathrm{ely,median}}$	Median electrolyser capacity in GW	7.1

Continued on next page

Symbol	Description	Reference
$P_{\text{gen,r}}$	Installed renewable capacity (source r) in MW	6.1
$P_{\text{gen,PV}}$	Installed PV capacity in GW	A.5
$P_{\text{gen,Wind}}$	Installed wind capacity in GW	A.5
$P_{\text{load,el}}$	Total electric load in MW	6.24
P_{ren}	Total installed renewable capacity (wind + solar) in GW	7.1, 7.1
$P_{\text{total,r}}$	Maximum regional capacity (source r) in MW	6.1
P_{norm}	Normalised power (–)	6.25, 6.26
P_{res}	Residual load in MW	6.24, 4.3
$\dot{Q}$	Heat flow rate in W	1.16, 1.20, 1.1
R	Universal gas constant in $\mathrm{J\,mol^{-1}\,K}$	A.17
r_{3PM}	Reaction rate in $\mathrm{mol\,kg^{-1}\,s^{-1}}$	2.4, 2.8, A.17
S	Stoichiometric ratio	3.1
t	Time in s	1.7, 1.3
t_0	Start time of annual integration in h	6.27
t_{end}	Final time of annual integration in h	7.1, 7.2, 6.27
t_{max}	Upper time limit for gas-production integrals in h	7.5
T	Temperature in K	1.1, 1.8
T_{cool}	Coolant temperature	2.8
u	Specific internal energy in $\mathrm{J\,kg^{-1}}$	1.9, 1.8
u_g	Gas-phase velocity in $\mathrm{m\,s^{-1}}$	A.1, A.8
U_G	Superficial gas velocity in $\mathrm{m\,s^{-1}}$	A.9, 2.10, A.3
V	Volume in $\mathrm{m^3}$	1.8, 1.9
V	Voltage in V	1.1
V_i	Total volume of discretised cell i	A.3, A.4
$V_{i,g}$	Gas-phase control volume of cell i in $\mathrm{m^3}$	A.2, A.3
$V_{i,sl}$	Slurry-phase control volume of cell i in $\mathrm{m^3}$	A.4
V_{cat}	Catalyst volume in $\mathrm{m^3}$	2.16
V_g	Volume of gas phase	2.17
V_L	Volume of liquid phase	2.16
V_{mpm}	Expanded multiphase-mixture volume in $\mathrm{m^3}$	2.17
V_{sl}	Slurry volume in $\mathrm{m^3}$	3.1, 2.16
$\dot{V_G}$	Volumetric gas-flow rate in $\mathrm{m^3\,s^{-1}}$	A.9
$\dot{V}_{H_2}$	Hydrogen volume flow rate	3.1
X	Mass fraction for mixtures (–)	1.5
$\vec{X}_g$	Vector of gas-phase mass fractions	2.3

Continued on next page

Symbol	Description	Reference
X_{g,CO_2}	Mass fraction of CO_2 in gas phase (–)	2.3
X_{g,H_2}	Mass fraction of H_2 in gas phase (–)	2.3
X_{g,CH_4}	Mass fraction of CH_4 in gas phase (–)	2.3
X_{g,H_2O}	Mass fraction of H_2O in gas phase (–)	2.3
$\vec{X}_{sl}$	Vector of slurry-phase mass fractions	2.4
X_{sl,CO_2}	Mass fraction of CO_2 in slurry phase (–)	2.4
X_{sl,H_2}	Mass fraction of H_2 in slurry phase (–)	2.4
X_{sl,CH_4}	Mass fraction of CH_4 in slurry phase (–)	2.4
X_{sl,H_2O}	Mass fraction of H_2O in slurry phase (–)	2.3
X_W	Primary-liquid mass fraction (–)	A.10, A.3
x	General variable in DAE system	1.5, 1.6
$\vec{x}_s$	Vector of steady states	1.3
y	General variable in DAE system	1.5, 1.6
$\vec{y}$	State variable vector	1.4
z	Slurry height at no-load in m	3.1
z	Spatial dimension	A.1, A.8
z_{mpm}	Height of expanded multiphase mixture in m	2.21
z_{cell}	Discretisation step length in m	2.21

Greek variables

Symbol	Description	Reference
α	Sparger exponent (Lemoine)	A.12, A.3
α_{cool}	Cooling heat-transfer coefficient in $\mathrm{W\,m^{-2}\,K^{-1}}$	2.8
β	Isobaric expansion coefficient in $\mathrm{K^{-1}}$	2.24, 2.25
χ	Percentage conversion in %	
χ_{in}	Input gas composition	3.1
$\Delta H_{\text{f}}^{\circ}$	Standard enthalpy change of reaction in $\mathrm{kJ\,mol^{-1}}$	1.1, 1.2, 2.1, 2.2
ΔH_{r}	Heat of reaction in $\mathrm{kJ\,mol^{-1}}$	2.8
Δp_f	Pressure loss due to friction in Pa	1.12
δT	Temperature difference between source and sink	4.1
ε	Gas holdup coefficient (dimensionless)	2.3, 2.4, A.3, A.4, A.5, A.7
ε_{g}	Gas holdup for the bulk gas phase (dimensionless)	A.1, A.3, A.5, A.7, A.11, A.3
ε_{P}	Catalyst-pellet porosity (dimensionless)	A.10, A.11, A.3
ε_{sl}	Holdup of dissolved species in the slurry phase (dimensionless)	2.8, 2.13, A.4, A.5
η_{cat}	Catalyst efficiency (dimensionless)	2.4, 2.8
η_{CHP}	CHP efficiency (–)	6.13
Γ	Sparger parameter, $K_d N_O d_O^{\alpha}$ (dimensionless)	A.10, A.11, A.12
κ	Isothermal compressibility in $\mathrm{Pa^{-1}}$	2.24, 2.25
$\lambda_{\text{sl,eff}}$	Effective thermal conductivity of slurry in $\mathrm{W\,m^{-1}\,K^{-1}}$	2.8, 2.9, 2.14
μ_L	Dynamic viscosity of the liquid in Pa s	A.11
ν_{i}	Stoichiometric coefficient of species i (dimensionless)	2.4
$\vec{\nu}_{\text{i}}$	Vector of stoichiometric coefficients	2.4
ϕ_C	Bubble column diameter in m	2.10, A.9, 2.17, A.10, A.11, A.13, A.15, A.3
ρ	Density in $\mathrm{kg\,m^{-3}}$	1.9, 1.10, 1.8
ρ_G	Density of the bulk gas phase in $\mathrm{kg\,m^{-3}}$	A.11, A.15
ρ_P	Density of catalyst particles in $\mathrm{kg\,m^{-3}}$	A.10, A.11, A.3
ρ_L	Density of liquid in $\mathrm{kg\,m^{-3}}$	A.10, A.11, A.15
ρ_S	Density of solid phase in $\mathrm{kg\,m^{-3}}$	2.8

Continued on next page

Symbol	Description	Reference
ϱ_{sl}	Density of slurry phase in $\mathrm{kg\,m^{-3}}$	2.8, 3.2
σ_L	Surface tension of the liquid in $\mathrm{N\,m^{-1}}$	A.10, A.11, A.15
τ	Empirical factor for gas–sparger influence (dimensionless)	A.11
φ	Volumetric solid fraction (dimensionless)	2.4, 2.8
φ_S	Volumetric solid fraction of solids in % (dimensionless)	2.4, 2.8
ϑ_{alc}	Weighted average temperature in °C	4.5, 4.4
$\omega_{cu,r}$	Capacity-utilisation factor for renewable source r (dimensionless)	6.1, A.6
ω_{DH}	Share of district heating in annual energy supply (dimensionless)	6.10,A.6
ω_{el}	Share of electricity in annual energy supply (dimensionless)	6.11
$\omega_{\mathrm{H_2}}$	Ratio of H_2 production to demand (dimensionless)	7.4, A.6
ω_s	Sectoral energy ratios	6.3, 6.5, 6.8
$\omega_{s,ec}$	Ratio of carrier ec in annual heat demand of sector s (dimensionless)	6.10
ω_{SNG}	Ratio of SNG production to demand (dimensionless)	7.4, A.6
ω_X	Energy carrier share (X is H_2, SNG, el, DH)	A.5
ω_{PtX}	Ratio from scenario dataset to size electrolysis/methanation capacities (dimensionless)	6.23, 7.1
ζ	Sparger open-area ratio (dimensionless)	A.11, A.13

Counters

Variable	Type	Context	Domain/Range
s	Sector index	Energy system integration	$s \in \{1, 2, 3\}$ (HEF, HMF, SME)
evt	EV type index	Network modelling	$evt \in \{1, 2\}$ (regular, fast charging)
ec	Energy carrier index	Energy system integration	$ec \in$ {SNG, H_2, el}
i	Building type index	Energy system integration	$i \in \{1, 2, \ldots, 15\}$ (BDEW categories)
i	Species index	Dynamic PtG modelling	$i \in \{H_2, CO_2, CH_4, H_2O\}$
i	Normalization index	Scenario analysis	$i \in \mathbb{N}$ (result processing)
i	Parameter index	Sensitivity analysis	$i \in \{1, 2, \ldots, n_{\text{DOE}}\}$
j	Spatial cell index	Dynamic PtG modelling	$j \in \{1, 2, \ldots, n_{\text{cells}}\}$
r	Renewable source index	Energy system integration	$r \in$ {PV, Wind}

Indices

Symbol	Description
$3PM$	3-Phase Methanation
ax	Axial
b	Building
bat	Related to battery storage
$cool$	Coolant cell
el	Electric
ely	Electrolysis
f	Friction (as in Δp_f) or Formation (as in ΔH_f)
g	Gas phase
G/L	Gas–liquid interface
in/out	Inlet or outlet flow
L	Liquid phase
met	Methanation system
mpm	Multiphase mixture
nom	Nominal or rated value (e.g. $P_{\mathrm{DH}}^{\mathrm{nom}}$)
$norm$	Normalised quantity
r	Renewable source index (PV or Wind)
R	Reactor
rel	Relative
S	Solid phase
Sc	Scenario
sl	Slurry phase

Introduction

Discussions at COP 29 reaffirmed the need to limit the global-temperature increase to 1.5 °C. In order to achieve this goal, renewable-energy strategies must address the energy trilemma, where energy systems need to: (i) achieve GHG-emission reductions across multiple sectors, (ii) ensure that supply security is not compromised even if renewable power production is intermittent, and (iii) ensure that the transformation is cost-effective. In this context, the concept of sector coupling, where renewable power is used to produce sustainable energy carriers or feedstocks which can be used in multiple sectors, becomes relevant. Among the various sector-coupling technologies, the power-to-gas (PtG) process uses gaseous chemical energy carriers such as substitute natural gas (SNG) or H_2 produced from renewable power to couple the sectors. The potential of power-to-gas technology in distributed energy systems is high, as it can be used for the on-site conversion of surplus renewable power into chemical energy carriers which in turn can be used for long-term energy storage. However, future energy systems are expected to be heterogeneous in terms of geographical distribution, energy mix, technologies used and operational strategies. The integration of power-to-gas technology into such distributed energy systems requires a modelling framework that can be adapted to the individual requirements of each system. These requirements include analysing the interactions between local weather conditions, intermittent renewable-energy production, demand from different types of buildings, and fluctuations in industrial demand. Insight into such dynamic interactions specific to each de-central system is important to decide the capacities of the power-to-gas units and the control strategies required. The analysis of future energy systems also needs to take into account the so-called “energy scenarios”, which outline the changes in the energy mix needed to meet sustainability goals. Therefore, the modelling tool must also be able to simulate energy systems under different future energy scenarios, where the shares of different energy carriers in the energy mix are subject to change.

Analysing the impact of implementing the energy scenarios also answers key questions such as the impact of direct electrification versus a molecule-based seasonal-storage strategy in the energy system. The overall objective of this work is to assess how future energy scenarios affect gas-based sector coupling in de-central energy systems under dynamic and site-specific operating conditions. To achieve this overall objective, this thesis describes a modelling framework capable of simulating the integration of power-to-gas technology into de-central energy systems. The modelling framework can simulate the dynamic interactions between the different components of the system. In addition, it can be adapted to analyse the impact of implementing future energy scenarios specific to each de-central energy system.

Research questions and strategies adopted to address them

Achieving the overall objective of this work requires answers to different research questions regarding the integration of power-to-gas technology into de-central energy systems. They can be divided by scale into three progressive parts of the energy system. The simplest blocks of the energy system are the components that are aggregated into the energy system on which the scenarios are implemented. Therefore, it is necessary to separate the research questions and the methods used in this thesis to address these three aspects. The research questions and strategies adopted can be summarised as:

1. **Research questions – Component level:**

    a) What core models (e.g. PV systems, storage elements, building-energy systems, energy networks) are needed to simulate dynamic processes in de-central energy systems, and how can missing components such as a dynamic three-phase methanation process be modelled and integrated?

    b) What should the level of detail (LOD) of the components be so that the de-central energy system is simulated without missing features of individual components?

    Strategy adopted: The component models that are already available, such as wind and PV models, are adopted as such. Others, such as building-energy systems, are modified to keep the level of detail just sufficient to simulate the de-central energy system without losing individual building characteristics such as weather dependence and user behaviour.

    Models, such as three-phase methanation, which are not available at all in the literature, are developed and validated from scratch.

2. **Research questions – Integrated energy systems:**

    a) How can multiple building types be integrated into the energy-system model without compromising on variability in the building types?

    b) How can the integrated energy system incorporate multiple component time scales (temporal aspects) and the distribution of components across multiple geographic locations (spatial aspects) in the same energy system without compromising simulation performance?

    Strategy adopted: Building models are categorised by energy carriers used, allowing buildings connected to electricity, gas or district-heating networks to be grouped in the energy-system model. To enable simulation of multiple time scales and high spatial resolutions, a co-simulation approach is adopted that allows the energy-system model to be co-simulated with dedicated network-simulation models for multi-nodal networks (gas, electricity or district-heating) with high spatial resolution.

3. **Research questions – Energy scenarios in de-central systems:**

    a) How can the energy scenarios be implemented in the de-central energy system to analyse the impact of different energy mixes and technologies in the future?

    b) How can location-specific aspects like the scale-up of renewable capacities be addressed?

    Strategy adopted: De-central energy systems are adapted to the technology mix from the energy scenarios. The resulting energy systems (corresponding to each scenario) are simulated and compared using location-specific boundary conditions. To analyse scaling up, a parameter sensitivity study is carried out where the capacities of renewable plants are varied to analyse their impact.

Structure of this dissertation

To address the research questions, an incremental approach is adopted, starting from the component level, then moving to the integrated system, and finally to the scenarios and parameter studies analysed using the integrated energy system. The dissertation is structured as follows:

1. Chapter 1 provides an overview of the fundamentals of energy-system modelling.
2. Chapter 2 describes the modelling of the three-phase methanation (3-PM) reactor, the various assumptions used and the thermodynamic reformulation required to integrate the model into the energy system.
3. Chapter 3 describes the validation of the dynamic three-phase methanation model.
4. Chapter 4 describes the integration of the component models into the de-central energy system and the adaptations required in building-energy systems to integrate them without compromising on the level of detail.
5. Chapter 5 describes the clustering methods to group the components according to sectors and energy carriers. It also describes the co-simulation approach and defines how models with multiple time scales interact with network models having high spatial resolutions.
6. Chapter 6 describes the implementation of energy scenarios specific to the de-central energy system and case studies analysing the impact of location, renewable potential, different energy mixes and technologies on the sector-coupling strategies in the region.
7. Chapter 7 presents parameter-sensitivity studies that analyse the impact of scaling up renewable capacities within the de-central energy system.

1 Fundamentals

Given varying interpretations for sector coupling in the literature, it is essential to establish clear definitions for the concepts and terms related to sector coupling as applied in this work. Therefore, in the first part of this chapter, concepts such as sector coupling, power-to-gas, de-central energy systems, and energy system modelling are defined as they are used in this work. This chapter then outlines the basic concepts and methods required for the modelling and analysis of de-central energy systems. Studies using integrated energy system models with components having different time scales are then reviewed. Further, the chapter also examines studies analysing methods to incorporate numerical models of multiple building types into the integrated energy system model. Following this, the chapter introduces the Modelica environment as the tool for carrying out the simulations, with special emphasis on its acausal modelling paradigm, multi-physical connection capabilities, and the use of equations of state (EOS) based fluid property calculations.

The use of differential algebraic equations (DAEs) in Modelica for modelling dynamic systems is then introduced. Finally, the numerical and thermodynamic adaptations required for the effective use of DAEs in the context of de-central, multi-carrier energy system modelling are briefly introduced. These adaptations are used in the following chapter to integrate the dynamic 3-PM model into the overall energy system.

1.1 Sector coupling

The concept of sector coupling (Figure 1.1) refers to the integration of different energy sectors to enhance the efficiency and sustainability of energy systems. The coupling of sectors allows surplus renewable power to be stored and reused for balancing energy supply and demand. According to Ramsebner et al. [1], the definition and scope of sector coupling is not uniform in the literature.

Some studies limit the scope of sector coupling to individual sectors such as residential heating or mobility [2–4] while others also consider sectors like industry, buildings, electricity production and mobility [5–7]. The use of chemical energy carriers (Figure 1.2) from renewable energy sources is one of the many methods of sector coupling. Among the energy scenarios predicted for 2050, those that involve sector coupling and use renewable chemical energy carriers have the greatest potential to reduce greenhouse gas emissions [8] and avoid costly infrastructure overhauls [9].

Sector coupling methods include both short-term storage strategies to mitigate power fluctuations and long-term strategies to store renewable energy as hydrogen and its derivatives [10]. Renewable power can be used to produce liquids such as long-chain hydrocarbons via the Fischer-Tropsch process [11] or renewable methanol [12], as well as gases like Substitute Natural Gas (SNG) and H_2 (Figure 1.2). Renewable gases such as SNG or H_2 play a key role in sector coupling, as they can be transported to different sectors using the gas grid. They can be used for seasonal energy storage, as an energy source in sectors such as transportation, chemical industry, and residential heating and as both an energy source and as feedstock in the chemical industry.

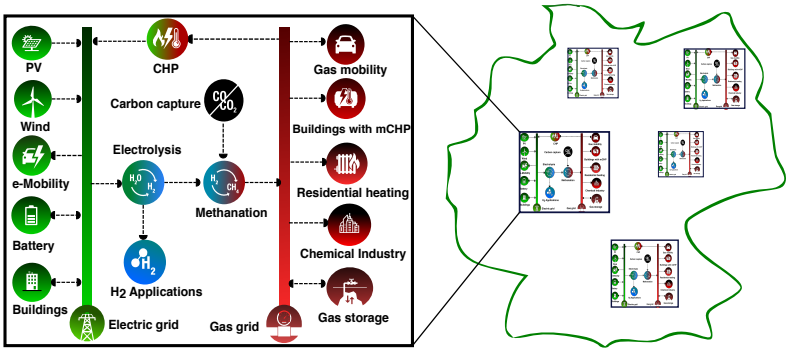

Figure 1.1: Concept diagram. Sector coupling in de-central energy systems. Image source (Own publication): Prabhakaran et al. [13]

Transporting and distributing SNG involves the least amount of infrastructure changes, while introducing 100% H_2 requires new infrastructure and further adaptations to existing networks [14]. In this work, sector coupling is defined as the use of technologies that enable the conversion of renewable power into sustainable feedstock or energy carriers, which can be utilised in sectors such as mobility, industry, or residential buildings. Using power-to-gas for sector coupling focuses on gaseous chemical energy carriers, specifically SNG or H_2.

1.2 The Power to Gas process

Power to Gas (PtG) refers either to processes using an electrolysis step to produce H_2 (Eq. 1.1) or processes with an additional methanation step where H_2 is converted into CH_4 (Eq. 1.2) using CO or CO_2. The term 'Power to Gas' has been used in published literature both for the production of H_2 and SNG [15–17].

$$H_2O_{(l)} \longrightarrow H_2 + \frac{1}{2}O_2 \qquad \Delta H_f^\circ = 285.8\,\mathrm{kJ\,mol^{-1}} \tag{1.1}$$

$$CO_2 + 4H_2 \rightleftharpoons CH_4 + 2H_2O_{(g)} \qquad \Delta H_f^\circ = -165.1\,\mathrm{kJ\,mol^{-1}} \tag{1.2}$$

The PtG process for hydrogen production has been receiving attention in various decarbonisation strategies [18–20]. FCH-JU estimates H_2 demand in the EU to range from 780 to 2251 TWh by 2050 [19]. The EU expects 25% of electricity generation to be used to produce H_2 by 2050 [18]. The German national H_2 strategy [21] projects an H_2 demand in the range of 90 TWh to 110 TWh by 2030. For Germany, imported H_2 is expected to play a significant role in the national hydrogen supply with an estimated 50% to 70% of the total demand expected to be realised through imports by 2030 [22].

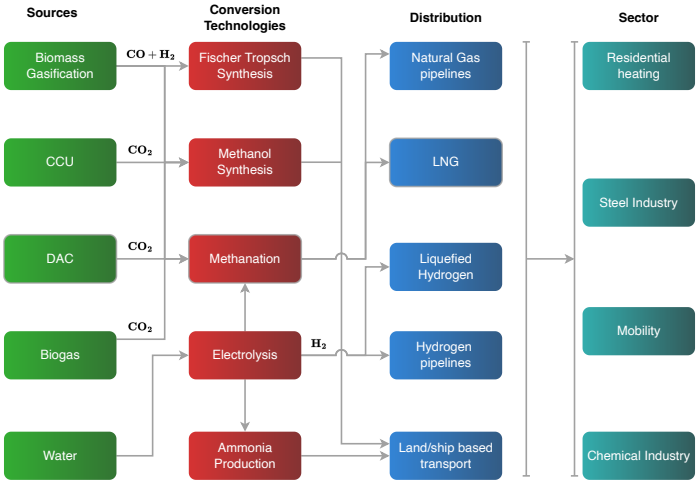

Figure 1.2: Various liquid and gaseous chemical energy carriers possible in sector coupling

By 2045 a demand of about 360-500 TWh for H_2 and 200 TWh for H_2 derivatives is expected to be met through imports in Germany [22]. Implementing the hydrogen strategy requires a new or modified infrastructure for hydrogen storage, transport and consumption [23]. The large-scale use of H_2 is just one of the many proposed sector coupling strategies. Several EU decarbonisation studies for the year 2050 also investigate the potentials of biomethane and biomass gasification. These two processes have the potential to meet up to 26% of the overall gas demand in the EU and can be implemented in parallel to electrolysis-based H_2 technologies [24, 25]. In addition, both processes generate CO and CO_2, which can be used to produce green hydrogen derivatives like SNG or Methanol. PtG plants may also be connected to existing industrial processes. Eveloy and Gebreegziabher [26] investigated PtG systems with biomass co-fired CHP units. In addition, O_2 from the PtG process can be used in industries to reduce the use of dedicated air separation units (ASUs) that supply oxygen [26]. Other applications of PtG have been explored in sectors such as district heating, refinery applications, in combination with nuclear power plants, and in the chemical industry [26].

One promising application of PtG plants is to provide control reserve as a service to the power grid [27]. During power fluctuations in the grid, the transmission system operator is expected to provide the primary control reserve (PCR) within a 30 s time period [27]. The secondary control reserve is expected within 5 min, and further control known as the minute reserve takes around 15 min [27]. The control reserve is required both for the mitigation of surplus power generation and for the compensation of power deficits. During surplus power production, PtG plants can provide flexibility if they are capable of dynamic operation. In PtG plants producing H_2, the Proton Exchange Membrane (PEM) or Alkaline electrolysers can ramp up very fast to mitigate surplus power production [28]. The same is possible in PtG plants producing SNG if the methanation units are also capable of dynamic operation. The OPEX of the PtG process is highly dependent on the price of electricity [29] which depreciates rapidly in the control reserve market [27]. Participation in the control reserve market is lucrative for the PtG plant, as electricity spot prices decrease when renewable power generation is in surplus (due to the merit order system [30]). The PtG plant at Energiepark Mainz showed significant economic gains when operating in the control reserve market [27]. [1.1]

1.3 De-central energy systems

Several studies predict that future energy systems will be more regional and de-central [31–34]. Weinand et al. [35] reviewed the interpretations of de-central energy systems in publications around the world and found two distinct categories. In lower- to middle-income countries, de-central networks are analysed in most publications as standalone microgrids designed for rural areas which are not connected to the high pressure gas transport network or the high voltage power transmission grids. In contrast, most studies involving high-income countries analysed de-central systems as connected to the transport grids [35].

Within the German context, surveys conducted with stakeholders for future energy systems [31] resulted in predictions that included a mix of centralised and de-central solutions. Alstone et al. [36] categorised de-central systems into a uniform set of micro hydro power-based energy systems, solar home systems, microgrids and regional grids across countries of different income levels. Some studies, on the other hand, predict a more centralised future scenario in which chemical energy carriers generated from offshore wind parks or large-scale PV plants are injected into transport networks [37, 38]. In this work, the de-central energy system is interpreted as an energy system within a region that includes electric, gas, and district heating networks. Local solar and wind farms provide renewable power to the region. PtG plants convert power surplus to gas, which is then stored. Combined heat and power plants convert gas back into electricity and heat. Buildings, mobility, and industry in the region are clustered into groups with similar dynamic load profiles. Local storage systems, such as gas storage, thermal energy storage, and batteries, provide the storage option.

[1.1] The study was based on H_2, and the plant did not have a methanation unit capable of dynamic operation.

If local storage is not sufficient, the de-central energy system draws either electrical power or gas from the respective transport networks. Future demand centres, such as major cities, are expected to be geographically separated from areas with high renewable energy generation [39, 40]. This will also affect transmission and distribution networks [41, 42]. According to Reuß et al. [43], a separate evolution of hydrogen distribution and transport networks is more likely with hydrogen distribution networks more prominent in areas with enough H_2 fuelling stations. However, separate hydrogen distribution and transport networks are expected to evolve in areas with sufficient H_2 infrastructure demand.

A significant reduction in the size of the existing natural gas distribution networks is plausible if the present energy systems, which are supplied with natural gas by the distribution networks, are electrified.[1.2] In comparison, only a slight reduction is predicted if synthetic gases and sector coupling become prominent [41]. Wachsmuth et al. [42] present similar results and predict that not all natural gas distribution networks will exist as of today, but the transmission network will still be required.

In any future scenario, the de-central energy systems (and the models that analyse them) are expected to handle dynamic fluctuations in production and demand. The term 'flexibility' is often used to determine the ability of an energy system to handle fluctuations. The International Energy Agency (IEA) defines flexibility as the extent to which a power system can modify electricity production or consumption in response to fluctuations in renewable power generation [44]. For de-central energy systems flexibility depends on the following aspects:

1. Share of renewables which is the primary cause of intermittent power generation in the energy system
2. The nature of the gradients in renewable power generation, power demand and heat demand. The gradients differ depending on the nature of the timescales inherent to the process. For example, heat demand in a building is a slow process compared to frequency changes in the distribution network.
3. The availability of local energy storage units and demand side management which can be used to counter the intermittency.

1.4 European Hydrogen Backbone and Hydrogen Valleys

The European Hydrogen Backbone (EHB) is a cross-border hydrogen transmission network proposed by European Transmission System Operators to connect production hubs, ports, and major industrial demand centres [45, 46].

[1.2] Direct electrification in this context implies that the residential sectors and industries requiring low grade process heat switch to electric heat pumps.

The EHB targets a total coverage of 28000 km by 2030 and over 50,000 km by 2040, with approximately 60% repurposed from natural gas pipelines [45, 47]. Repurposing offers the advantage of reducing capital costs by 50–70% compared with building entirely new infrastructure [46] and enables transport at €0.11–€0.21/kg per 1,000 km [45], making it cost-competitive over long distances. The network design is based on five strategic supply corridors linking regions with strong renewable generation potential, such as the Iberian Peninsula and North Sea, to major demand clusters in central and northern Europe [46, 48]. These corridors also include port connections for importing hydrogen from global suppliers, supporting both energy diversification and market liquidity.

Future renewable hydrogen production and imports can be transported through the EHB to reduce dependence on fossil fuels and enhance resilience against external supply shocks [48]. To ensure efficient integration across borders, the EHB must operate under technical rules for gas quality, pipeline conversion, and safety [49]. Integrating multiple hydrogen valleys into the EHB, either as consumers or as suppliers of H_2, is planned to enable synchronising local production and demand through the backbone network [50].

Hydrogen valleys can be conceptualised as decentralised energy systems that integrate renewable hydrogen production, storage, distribution, and multiple end-use sectors within a defined geographic area [50]. They are designed to function as both receivers of imported hydrogen from ports and as suppliers of regionally produced hydrogen feeding into the EHB [50]. By enabling the co-location of generation, storage, and consumption, hydrogen valleys reduce the need for long-distance transport in early market phases, and also provide a platform for testing technical solutions [50].

The Renewable Energy Directive (RED III) [51] proposes imposing binding consumption targets for Renewable Fuels of Non-Biological Origin (RFNBOs). The share of RFNBOs is expected to be up to 42% of hydrogen use in industry by 2030, rising to 60% by 2035 [51]. Compliance is governed by specifying strict additionality, temporal, and geographical correlation requirements for hydrogen production [52]. To ensure compliance, future hydrogen valleys must satisfy the spatial and temporal clauses [50]. With intermittent power generation and varying demand, compliance with such clauses is feasible only if the hydrogen valleys can handle dynamic fluctuations in both production and consumption. This requires advanced modelling techniques to simulate the interactions between different components, such as electrolysers, storage systems, and end-use applications, ensuring that the system can respond effectively to changes in supply and demand. Further, the integration of hydrogen valleys into the EHB necessitates a robust framework for managing the flow of hydrogen across the network at multiple spatial points, making the spatial analysis in energy system modelling important. Taken together, spatio-temporal modelling of the energy system is crucial to analyse various aspects of implementing this strategy.

1.5 Energy system modelling

A purely experimental method of analysis is not possible in sector coupling due to the scale of the energy systems. In addition, it is difficult to conduct real-time experiments in existing energy systems without risking security of supply. It is therefore necessary to develop dynamic numerical energy system models. Various interpretations exist for the term 'energy system' in the literature. According to Herbst et al. [53], the definition of an energy system varies between target groups (policy makers, academics, and energy supply companies), intended use cases (cost calculation, simulation, optimisation, and forecasting) and coverage areas (local, regional and international). Some models are developed to minimise greenhouse gas emissions or costs, while others analyse technical aspects such as grid stability or security of supply [54].

Modelling strategies can be categorised as either top-down or bottom-up. The top-down approach refers to modelling scenarios at the national or international level with few technical details regarding individual components. In top-down models, the time intervals and the area under consideration are usually large [55, 56]. The bottom-up method comprises models that represent the physical behaviour of individual components. They can simulate energy systems consisting of interacting components with varying dynamics. Bottom-up models are better suited to evaluating aspects like the resilience of the energy system during dynamic perturbations [57–60]. Ringkjøb et al. [61] reviewed existing energy system models and showed that the time scales used in the models vary depending on the type of use. Grosspietsch et al. [62] and Weinand et al. [35] in their respective reviews found only a small set of models capable of analysing real-time interactions between different components. Prina et al. [63] categorised the models using four different aspects: resolution in time, resolution in space, techno-economic detail and sector coupling. Models were classified as low, medium or high for each field. Heider et al. [64] reviewed energy system models using the same method and reported the Modelica-based Transient library [59] and Python-based PyPSA [65] libraries to cover most of the evaluated fields. In de-central energy systems, the ability of a model to handle energy system "complexity" is often the deciding factor in its selection for modelling.

The definition of energy system complexity varies widely in the literature. Kotzur et al. [66] define the complexity of energy system modelling using the following aspects:

1. Complexity of the energy system as a whole
2. Complexity of the part of the energy system that is being analysed
3. Complexity of the computational model used to simulate the energy system

The first two aspects are not defined uniformly in most publications. For example, Lloyd [67] has tabulated a non-exhaustive list of at least 50 ways to describe complexity. However, complexity of the computational models can be described using the Big $\mathcal{O}$ notation [66, 68] which quantifies the number of individual elementary operations which in turn affects the total time required to complete an algorithm.

Most energy system models involve solving a system of equations that contain N equations and N variables aggregated into a NxN matrix. The final solution involves inverting these matrices. In the final matrix of N equations and N variables, the Big $\mathcal{O}$ notation for inversion can be between $\mathcal{O}(N^{2.3})$ and $\mathcal{O}(N^3)$. This means that the inversion requires between $N^{2.3}$ and N^3 individual elementary operations. This can be computationally expensive and, in most cases, render the models too slow for practical use.

For highly complex systems, if the complexity is mathematically reduced to $\mathcal{O}(N)$, the solution involves only N steps which is highly beneficial. Modelling languages like Modelica [69] have a mathematical backend[1.3] capable of doing this. The complexity of the energy system model depends also on the temporal and spatial resolution that it attempts to simulate. Analysing dynamic aspects like the interoperability of components require varying time scales [72]. For example, the frequency changes in the electricity grid are much faster compared to the time taken for changes in a thermal storage and the overall energy system model may need to simulate both. Priesmann et al. [73] determined that coupling various storage systems with different ramping rates further increases the system complexity. The complexity also increases if the spatial level of detail (LOD) is high [74].

At the component level, Building Performance Simulations (BPS) like the Buildings [75] and the AixLib libraries in Modelica [76] can be used for detailed simulations of individual buildings. BPS models can be classified as white box or black box [77]. Black box models use measured time series data from buildings, while white box models use balance equations to simulate building parameters. Two different guidelines are used in Germany for modelling white box models. ISO 13790 [78] simplifies building models using thermal capacities. The VDI 6007 [79], in comparison, specifies norms for detailed transient models involving multiple thermal masses [80, 81]. Both approaches are difficult to scale up to an urban level with multiple buildings. On the other hand, obtaining time series data for individual buildings in black box models is also challenging. The grey box model can be considered a middle ground [74, 82]. In this approach, the building energy systems use black-box data mostly for load estimation, with selected subsections like energy conversion and storage components using white box models. Data collection for individual buildings needs to be separated from the building simulations to scale up individual grey box models to urban systems [81]. Different approaches are used here.

The aggregation approach classifies buildings into standard types and builds urban regions using the standard types multiplied with a total number of buildings for each type [83–85]. The generation of archetype buildings often requires additional data like material properties and internal loads to be more accurate [84]. Some tools like TEASER [84] generate building parameter datasets for multiple buildings from known parameters. Further, the simulation of urban energy models with multiple buildings also requires simplified equation systems [76, 80].

[1.3] The Modelica compilers generally use a so-called frontend for modelling and a backend for mathematical optimisation of the equations. The frontend handles the initial processing of Modelica code, including lexical analysis of equations, parsing, and semantic analysis. The backend performs symbolic optimisations to improve performance, including pre-optimisation [70] (partitioning and alias removal in the equations), causalisation (matching, sorting, and index reduction), and post-optimisation (tearing and Jacobian computation [71]) making the equations solvable.

An efficient sector coupling model must also simulate deviations from the operational tolerances of all the energy system components. These include operating temperatures and pressures in thermal components, voltages and frequencies in electric components, quality of the gas product in the gas grid, and household comfort temperatures. Finally, the overall energy system must also have a mathematical back-end capable of reducing complexity and making the whole system solvable. In this work, the dynamic modelling tool is expected to handle multiple sectors, building types, energy carriers, and device types with different individual dynamics.

Furthermore, the number of equations is expected to be in the order of 10^4 to 10^5 depending on the complexity of the energy system.[1.4] To handle such energy systems, Modelica [69] is chosen as the modelling tool in this work.

1.6 Modelica

Modelica is a modelling language for systems with interacting physical components. Modelica, unlike traditional programming languages, is a modelling language intended to simulate dynamic systems. According to Fritzson [69], Modelica is a modelling language that allows specification of mathematical models of complex natural or man-made systems, for example, computer simulation of dynamic systems whose behaviour evolves as a function of time. Modelica has capabilities like index reduction, acausal connections, and an object-orientated programming structure [69, 71, 86]. These features make it suitable for simulating coupled energy systems across various physical domains. Multiphysical modelling using Modelica has been implemented in building energy systems [75], electric networks [87], thermal systems [88, 89], and integrated energy systems [59, 90]. It can simulate coupled energy systems with varying time scales in multiple physical domains.

Examples of integrated energy system models include coupled electrical storage and PV systems [91], electrical systems coupled to district heating and cooling [92] and even models coupling slow processes such as simulations of biological crop growth to energy systems [93]. Braun et al. [94] also tested the ability of Modelica to solve large transmission grids with high spatial complexity simulating systems of up to half a million DAEs. Rapid virtual prototyping of energy systems is possible with Modelica [95] as the modelling language uses object-orientated concepts. Modelica separates mathematical operations such as symbolic manipulation and index reduction from modelling. This ensures that the emphasis is more on equations that describe the physical behaviour of the component [69]. Modelica uses the so-called 'acausal connections' between components without specifying which way the information flows. This is one of its distinguishing features. Other modelling tools, such as Simulink [96] and Aspen Plus [97], use block- or signal-based connections with a fixed source, destination, and direction of the information flow.

[1.4] When all the individual component equations, connections and boundary conditions are flattened into a single system of equations, the total number of equations lies between 10^4 to 10^5 for all the models used in this work

Acausal connections avoid this by using conservation laws between the components. This reduces the number of connections between components compared to signal-based tools. Conserved quantities such as mass flow $\dot{m}$ or heat flow $\dot{Q}$ in a physical system require an interface between higher and lower potentials. For example, mass flow occurs between higher and lower pressures in fluid systems, and current requires an interface between higher and lower voltages in electrical systems. Modelica uses the concepts of flow and potential to enable acausal linkages between components. Conserved quantities seek to equalise the potential between two points when they are coupled.

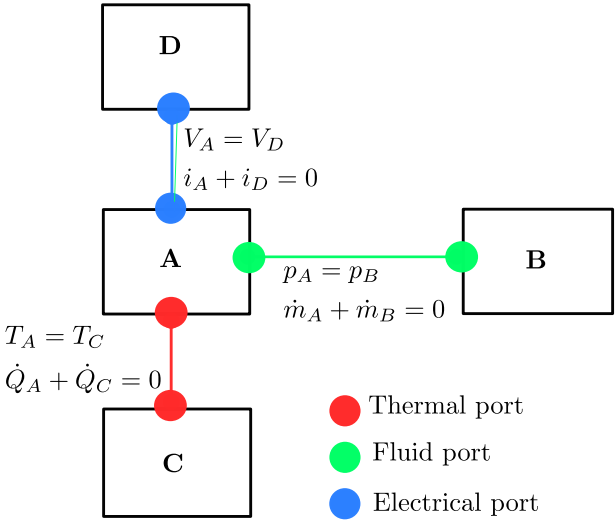

Figure 1.3: Concept diagram showing equality operation to potential variables and sum to zero operation to flow variables across three different domains

The equality operator is applied to the potential variables as shown in Figure 1.3. Flow is a conserved quantity. Therefore, a sum-to-zero operator is applied to the flow variables. The sum-to-zero operator ensures that the flow entering one component is negative of the flow exiting the component to which it is connected, as shown in Figure 1.3. This enforces the conservation laws between each connection. The acausal connectors use conservation laws and therefore they work only in pairs. The potential and flow variables for different physical domains are defined in Table 1.1. In Modelica, different potential and flow variables can be used in the same model. This enables multi-physical connections. Figure 1.4 shows a power plant model in the open source Thermopower library [98]. The axial connections in the fluid (compressors, combustion chamber), mechanical (turbines, generators), and electrical (generators, turbines) ports are always in pairs. However, one-sided signal connections are also required in several parts of the model. The direction specified signal connectors are typically used to provide ramping inputs or taking outputs from sensors as a time series array.

Table 1.1: Potential and flow variables across physical domains.

Domain	Potential variable	Flow variable
Thermal	Temperature T in K	Heat flow $\dot{Q}$ in W
Electrical	Voltage V in V	Current i in A
Hydraulic	Pressure p in bar	Mass flow rate $\dot{m}$ in kg s^{-1}

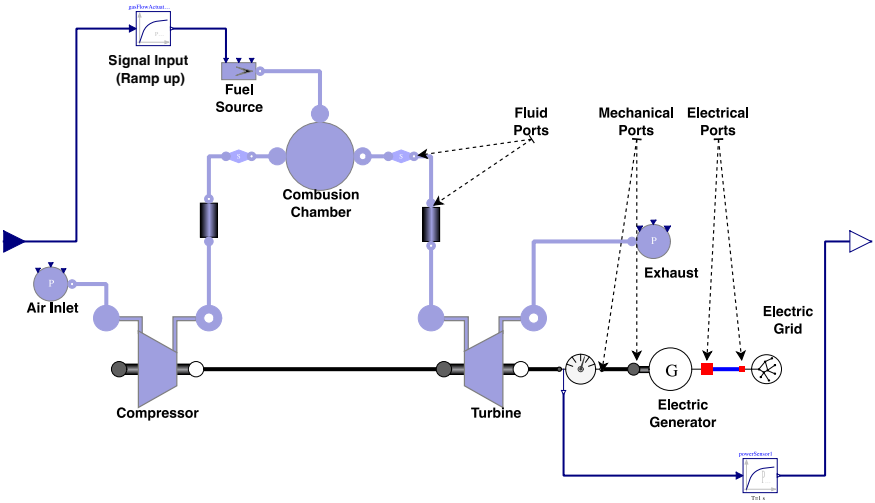

Figure 1.4: Turbine model showing signal port for controlling fuel input and multi physical connections across the fluid, mechanical and electrical domains. Image source. Thermopower Library [98]

To enable one-sided interaction with the system, Modelica also provides signal connections where the direction is specified. These ports are called block connectors and are mostly used for signal-based control or sensing (see fuel source control in Figure 1.4).

1.7 Numerical solution of DAEs

Calculating changes in reactant or product concentrations under varying temperature and pressure is essential in chemical engineering. These processes can be modeled using steady-state or dynamic models. Equation 1.3 represents the steady-state model, where $\vec{x_s}$ is the vector of steady states and $\vec{p}$ are the influencing parameters.

$$0 = f(\vec{x_s}, \vec{p}) \tag{1.3}$$

Dynamic processes involve transient changes, simulated using state variable and their derivatives. Equation 1.4 represents the dynamic process, where $\frac{d\vec{y}}{dt}$ are the derivatives of the state variables. Equation 1.4 is a set of explicit Ordinary Differential Equations (ODEs).

$$\frac{d\vec{y}}{dt} = f(\vec{x}, \vec{y}, t) \tag{1.4}$$

Many chemical engineering applications require algebraic equations to calculate transport properties and hydrodynamic coefficients. Therefore in the final equation set, differential and algebraic equations must be combined. Such equation sets known as Differential Algebraic Equations (DAEs) can be represented as:

$$\dot{y} = f(x, y, t) \tag{1.5}$$

$$0 = g(x, y, t) \tag{1.6}$$

DAEs cannot be solved in their original form, where the differential and algebraic equations are combined. They can only be solved by converting all the algebraic equations into their corresponding differential forms and solving the resulting system of ODEs. The index of a DAE is the number of times that the system has to be differentiated before the DAE system is transformed into a set of ODEs. DAEs have an index of 1 or greater. Therefore, an index reduction is required to reduce the DAE index to 0. Index reduction algorithms vary between Modelica compilers. Many of them use variations of the Pantalides algorithm [99].

Additional mathematical reformulations, such as symbolic sorting of equations, equation variable matching, tearing, and relaxation algorithms, may also be required before the system of equations is reduced to solvable ODEs [70]. For thermofluid models, index reduction is challenging. In these models, the calculation of transport and hydrodynamic properties require the state of the fluid. This implies that the adaptations depend heavily on the "state variables" used to calculate fluid properties. From a mathematical standpoint, any variable whose derivatives are defined in the DAEs can be considered as a state.

Elmqvist et al. [100] use the term ‘model states’ to define them. From a physical point of view, the state of a fluid is determined by thermodynamic state variables such as absolute pressure p, temperature T, density ρ, specific enthalpy h, and specific internal energy u. In several chemical engineering processes with connected components like reactors, storage vessels and pumps, thermodynamic state variables and their derivatives are a part of conservation equations. The same state variables are also needed in the algebraic equations to calculate fluid and hydrodynamic properties.

1.8 Calculation of fluid properties

The conservation equations for incompressible liquids, real gases, ideal gases, and two-phase mixtures are an integral part of thermofluid components. The equations of state (EOS) are often used to calculate the properties of fluids. The EOS takes two independent thermodynamic state variables from pressure p, temperature T, internal energy u, density ρ, or specific enthalpy h as inputs. Using the input state variables, the EOS calculates the dependent variables which can then be used in thermodynamic relations to calculate hydrodynamic properties.

The choice of independent variables influences the computational efficiency of EOS-based fluid property calculations [88]. Pressure p and specific enthalpy h are used in various commercial fluid property tools as reference input variables [101–104]. They can be calculated using the energy and momentum balance equations from the model. The EOS based fluid property calculations are also used in commercial tools such as ASPEN Plus [97], ChemCAD [105] and ANSYS [106]. Commercial fluid property libraries, such as REFPROP [102] include a list of fluids that can be used in chemical engineering applications.

It uses explicit Helmholtz energy equations for pure fluids, the modified Benedict-Webb-Rubin equation [107], and an extended corresponding states (ECS) model for high-accuracy calculations [108]. Other commercial tools like TIL-Media use the accurate multi-parameter EOS developed by Span et al. [109]. All component models in this work use the TIL Media Suite [104] for fluid property calculations, which provides the option of choosing between different EOS-based tools depending on the accuracy and computational speed required [88, 89, 110]. The challenge in thermofluid systems is to reduce the index of DAEs where the algebraic equations are coupled to external EOS-based tools for fluid property calculations.

Index reduction is a mathematical operation that attempts to convert algebraic equations to their differential form. The fluid property calculations in EOS tools are black boxes as far as the DAE is concerned. This is because they are external tools and the EOS equations themselves are not a part of the DAE system. Therefore, attempting to get the derivatives of the equations numerically can lead to either the index reduction itself failing, or worse, the index reduction taking place but with errors in the fluid properties. If the fluid property calculations produce even small errors, these can accumulate during the integration of the ODEs, leading to drastically different results. In Modelica, the solution is to provide the derivatives of the state properties explicitly in the DAE system. This allows index reduction to be carried out without differentiating the equations that are coupled to external EOS-based tools [89, 111].

The importance of this critical aspect can be illustrated using the example of a flow element shown in Figure 1.5. The flow element is an integral part of several components like heat exchangers, reactor elements or flow pipes. The states of the incoming and outgoing flows are determined using variables: $(\dot{m}, p, h, X)$.[1.5] Balance equations are used to determine the dynamic behaviour of the state variables: (p, h, X) within the control volume.

[1.5] The variable X is the state variable for mass fraction which is used in cases where mixtures are involved

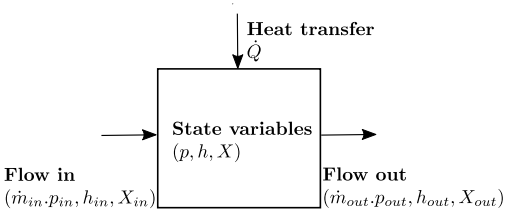

Figure 1.5: The flow element showing input, output and state variables

The mass balance equation can be written as:

Mass balance:

$$\frac{dm}{dt} = \dot{m}_{\text{in}} + \dot{m}_{\text{out}} \tag{1.7}$$

where:

$$\frac{dm}{dt} = \frac{d(\rho \cdot V)}{dt} = \rho \cdot \frac{dV}{dt} + V \cdot \frac{d\rho}{dt} \tag{1.8}$$

As the volume does not change, eq. 1.8 simplifies to:

$$\frac{dm}{dt} = V \cdot \frac{d\rho}{dt} \tag{1.9}$$

where:

$$\rho = f_{\text{EOS}}(p, h) \tag{1.10}$$

Momentum balance:

$$\frac{dp_{\text{in}}}{dt} = \frac{dp_{\text{out}}}{dt} \tag{1.11}$$

$$p_{\text{out}} = p_{\text{in}} - \Delta p_f \tag{1.12}$$

$$p = \frac{p_{\text{in}} + p_{\text{out}}}{2} \tag{1.13}$$

where Δp_f is the pressure loss due to pipe friction.

Energy balance:

$$\frac{d}{dt}(H - p \cdot V) = \dot{H}_{\text{in}} + \dot{H}_{\text{out}} + \dot{Q} \tag{1.14}$$

since:

$$H = m \cdot h \tag{1.15}$$

$$\frac{d}{dt}(m \cdot h) = \dot{H}_{\text{in}} + \dot{H}_{\text{out}} + V \cdot \frac{dp}{dt} + \dot{Q} \tag{1.16}$$

where:

$$\dot{H}_{\text{in}} = \dot{m}_{\text{in}} \cdot h_{\text{in}} \tag{1.17}$$

$$\dot{H}_{\text{out}} = \dot{m}_{\text{out}} \cdot h_{\text{out}} \tag{1.18}$$

which transforms eq. 1.16 into:

$$m\frac{dh}{dt} + h\frac{dm}{dt} = \dot{m}_{\text{in}} \cdot h_{\text{in}} + \dot{m}_{\text{out}} \cdot h_{\text{out}} + V \cdot \frac{dp}{dt} + \dot{Q} \tag{1.19}$$

Using the mass balance equation eq. 1.8, the energy balance can be rearranged as:

$$\frac{dh}{dt} = \frac{1}{m} \cdot \left[\dot{m}_{\text{in}} \cdot (h_{\text{in}} - h) + \dot{m}_{\text{out}} \cdot (h_{\text{out}} - h) + V \cdot \frac{dp}{dt} + \dot{Q} \right] \tag{1.20}$$

The mass, momentum[1.6] and the energy balances are represented in equations 1.7, 1.11 and 1.20. It can be seen that in the balance equations, the derivatives $\left[\frac{dm}{dt}, \frac{dp}{dt}, \frac{dh}{dt}\right]$ of the state variables $[m, p, h]$ are integrated. Of these, two of the state variables (p, h) can be used as input in the equations of state. Therefore, the mass balance in eq. 1.7 is reformulated in terms of density ρ. As density ρ is a dependent variable, it can be calculated from the independent variables (p, h) using a function call to the EOS tool as shown in Equation 1.10. $f_{EOS}(p, h)$ is a call to a function to calculate fluid properties outside the DAE. The function in the EOS tool is a black box that uses the independent state variables (p, h) to return the dependent variable ρ. Index reduction is a mathematical operation to convert the algebraic equations within the DAE into its differential form. Therefore, if the algebraic equations use external EOS tools, the index reduction fails as the DAE solver can only access the system inside Modelica and cannot numerically differentiate the algebraic equations that call external functions. However, if the derivative $\frac{d\rho}{dt}$ is reformulated in (p, h) and provided explicitly in the DAE itself, index reduction does not require numerical differentiation of external functions.

Richter [89] explains a method to provide the derivatives explicitly as :

$$\frac{d\rho}{dt} = \left(\frac{\partial \rho}{\partial p}\right)_h \frac{dp}{dt} + \left(\frac{\partial \rho}{\partial h}\right)_p \frac{dh}{dt} \tag{1.21}$$

$\left(\frac{dp}{dt}\right)_h$ and $\left(\frac{\partial \rho}{\partial h}\right)_p$ are functions of the state variables (p, h) and are available in many of the standard equation of state-based fluid property calculation software such as Helmholtz Media [112], REFPROP [102] and TIL Media [104].

[1.6] Richter [89] shows that if spatially varying dynamic processes such as sound propagation do not occur in the model, the momentum balance can be simplified by assuming the state point p to be the average of the inlet and outlet pressures (Equation 1.13) and the pressure derivatives can be assumed to be uniform along the axis of the control volume (Equation 1.11).

$\frac{dp}{dt}$ and $\frac{dh}{dt}$ in eq. 1.21 can be determined from the energy and momentum balances. Here, the index reduction does not fail as it does not need to differentiate the external EOS based functions. The use of explicit functions for the density derivative also reduces the number of state variables in the overall system to just p and h with all the other hydrodynamic parameters derived from them. The method of providing explicit derivatives can be generalised to any new thermofluid model in Modelica. Elmqvist et al. [100] define the general logic of using state variables in chemical and thermofluid systems. The first step is converting the 'model states' like mass m or concentration C into 'thermodynamic states' by reformulating the balance equations. With the reformulated balance equations, the derivatives should then be provided as explicit functions of the state variables (p, h) to make index reduction possible.

The model for the 3-PM reactor developed in this work is integrated into Modelica using the same method. The 3-PM model developed in this work is adapted by first reformulating the balance equations so that p and h are the mathematical state variables in the DAE, as well as the thermodynamic state variables that define the physical system. Subsequently, the derivatives of the state variables are provided to make index reduction possible. The biggest advantage is that highly complex fluid property calculations can be separated from the model itself. This also means that external fluid property calculation tools can be used or changed based on the accuracy or speed required in the model. In addition, the number of differential variables needed to model the system is also reduced (as opposed to a PDE based system of equations which uses arbitrary differential states like various fluid concentrations, temperatures, enthalpies, etc.). As all the other components of the energy system also use the same state variables, the index reduction of the overall energy system is not affected when the 3-PM model is integrated into it.

2 Modelling the Dynamic 3-PM system

CO_2 and CO methanation (Equations 2.1 and 2.2) can be used to convert H_2 into CH_4 in the Power to Gas process. Both reactions are highly exothermic. In the overall Power to Gas system, it is important to demarcate the boundaries of the entire system from the methanation process, which is the focus of this chapter.

$$CO_2 + 4H_2 \rightleftharpoons CH_4 + 2H_2O \qquad \Delta H_f^\circ = -165.1\,\mathrm{kJ\,mol^{-1}} \tag{2.1}$$

$$CO + 3H_2 \rightleftharpoons CH_4 + H_2O \qquad \Delta H_f^\circ = -206\,\mathrm{kJ\,mol^{-1}} \tag{2.2}$$

The Power to Gas system includes an electrolysis unit connected to a methanation system. The methanation system (Figure 2.1) comprises feed management, a methanation reactor, and heat exchangers to condense the reactor output gas. The focus of this chapter is the methanation reactor.

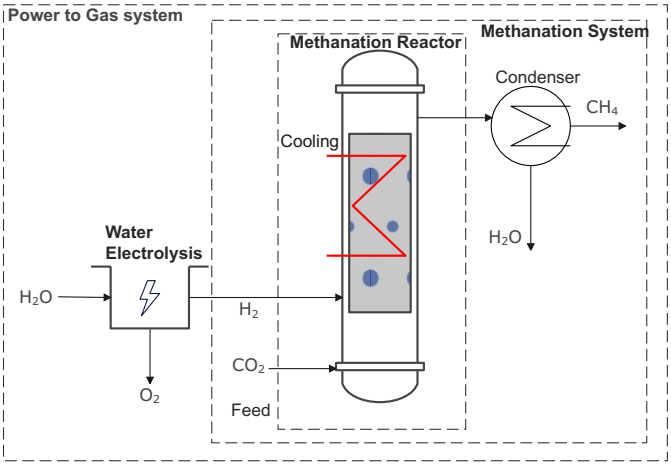

Figure 2.1: Conceptual diagram illustrating the Power to Gas system and the scope of the methanation reactor within it

2.1 Challenges in dynamic operation

The components of the energy system must be able to modulate their output in response to intermittent renewable production and fluctuating demand. Both PEM and alkaline electrolysers can be operated dynamically. Ramping rates for both electrolysers are reported to be in the order of seconds [28]. SOEC electrolysers must operate at high temperatures and are not capable of fast dynamic operation like PEM or alkaline electrolysers [113]. The exothermic nature of the methanation process presents several challenges during dynamic operation of the reactor. If the methanation reactor cannot respond dynamically,[2.1] a buffer storage is required to store the H_2 and facilitate a more constant H_2 supply to the reactor.[2.2] To analyse the ability of the reactor to handle load changes, the input feed rate can be increased to assess the response. Theurich et al. [115] use the term 'parametric sensitivity' to define small changes in input parameters that cause significant and often destructive changes in reactor temperature and output product composition. Efficient heat removal and maintenance of an isothermal state during start-up are essential for reactor safety.

In fixed bed reactors, Kreitz et al. [116] reported a sharp increase in hotspot temperature and distribution during transient inlet feed variations. Ramping down the reactor can also be challenging, with Rönsch et al. [117] reporting two major problems. First, additional heat is required to bring the reactor back to hot standby. Lowering the temperature also increases the risk of carbonyl formation, which can deactivate the catalyst. For syngas methanation, carbonyl formation has been reported for operating temperatures below 500 °C [117] and for CO_2 methanation below 200 °C [118, 119]. Rönsch et al. [117] suggested the use of insulation or localised beds of inert material as a solution. Despite these issues, there have been studies focusing on dynamic operation using fixed bed reactors. Giglio et al. [120] used cooled tubes in multiple fixed bed reactors with bypass stages and gradually introduced CO_2. Bremer and Sundmacher [121] proposed dynamic operation by letting the transient hotspots occur, allowing the system to move away from the steady state and then controlling it in the unsteady regime by adaptive control of the coolant temperatures.

Iglesias Gonzalez et al. [122] used a cooling medium Marlotherm SH [123] for temperature control and used the eggshell structure for the catalyst to prevent damage. Other attempts at dynamic control include the use of molten salt [124] and micro-channel reactors [125]. Fache et al. [126] attempted dynamic operation by mixing the catalyst pellets in an inert carrier and varying the ratio between them to dilute the catalyst at different parts of the reactor. Fixed-bed reactors must be prepared for thermal runaways in all these scenarios. Fischer and Freund [127] specified the design changes necessary in the reactor for safe operation.

2.1 The dynamic response of the methanation reactor always implies that the whole methanation unit (Figure 3.1) also responds dynamically.

2.2 The use of additional H_2 storage increases the CAPEX of PtG systems, with reported storage prices for H_2 ranging from 20 Euro/m^3 to 490 Euro/m^3 [114].

2.2 The 3-PM reactor

The reactor developed at KIT EBI-ceb [128, 129] is designed for dynamic operation using a 3 phase methanation process (denoted 3-PM). The bubble column reactor (Figure 2.2) contains the slurry which is a suspension of the solid nickel-based catalyst in a liquid heat exchange medium. The liquid medium used here is dibenzyltoluene (DBT) with the commercial name Marlotherm SH [123]. In the bubble column, the reactant bubbles initially in the gas phase cross the gas-liquid interface into the slurry phase (Figure 2.2).

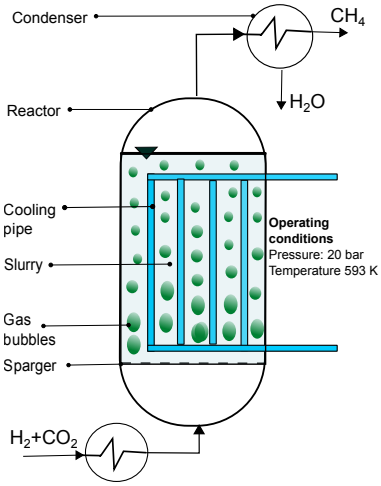

Figure 2.2: Concept diagram for slurry bubble column reactor. Image source: Own publication [13]

In the slurry phase, the reactants dissolve and diffuse to the catalyst surface where the reaction takes place and the products CH_4 and H_2O are formed. Although the reaction is highly exothermic, the liquid medium absorbs the reaction enthalpy, which enables dynamic operation during load changes without causing a thermal runaway in the reactor. The 3-PM kinetics was developed by Lefebvre et al. [15, 130] and later validated by Sauerschell et al. [129]. Integrating the 3-PM model into an energy system and analysing sector coupling requires the model to satisfy two necessary conditions. First, the balance equations should model the 3-PM process with reasonable accuracy. In addition, the 3-PM model must be capable of being simulated not as a standalone entity, but integrated with numerical models of other energy system components. The resulting model for the overall energy system must then be simulated using boundary conditions such as intermittent renewable energy generation and fluctuating demand.

2.3 Detailed Modelling of the 3-PM Process

The three-phase methanation (3-PM) process involves the dispersion of gas bubbles within a slurry medium. This slurry medium comprises both liquid and solid phases. For simplifying the mathematical modelling, this work treats the suspended solid catalyst and liquid medium as a unified slurry phase. Several modelling approaches exist for describing the behaviour of slurry bubble column reactors. Among these, the axial dispersion method was found suitable by Lefebvre et al. [15] for the specific operational requirements of the 3-PM reactor at EBI-ceb. The axial dispersion method simplifies the reactor dynamics into one-dimensional conservation equations. The spatial dimension used here is the positive z axis, coinciding with the upward direction of bubble flow. The mass and energy balance equations are derived along the vertical axis of the reactor. The original formulation by Lefebvre et al. [15] used partial differential equations (PDEs) using concentration as the state variable as shown in Equation A.1. However, concentration-based equations impose limitations when integrating the reactor into broader energy system models. Energy system models typically comprise multiple interconnected component models. To connect these component models, the incoming and outgoing flows between the components must be defined using the same variables. This means that integrating the methanation reactor model requires a reformulation of the balance equations.

The concentration-based balance equations must therefore be converted[2.3] into mass-based equations. This reformulation aligns the reactor model with upstream and downstream component models, which also utilise mass-based balance equations, thus enabling the simulation of inter-component flows. Further, to ensure uniform fluid property calculations throughout the energy system, it is required to further reformulate the balance equations using thermodynamic state variables. Specifically, state variables such as pressure (p) and specific enthalpy (h) provide a common thermodynamic basis to calculate the fluid properties for all the connected system components. Consequently, each species within the reactor is described using mass-based balance equations. The mass derivatives are then converted into density derivatives (Equation 2.22). Finally, the density derivatives are explicitly expressed using the thermodynamic state variables pressure and enthalpy, as depicted in Equation 2.24.

Using these uniform state variables across the energy system ensures compatibility with a common Equation-of-State (EOS) based fluid property calculation tool.[2.4] Further, the use of consistent state variables and fluid property calculations across all system components significantly simplifies the numerical complexity of the resulting Differential-Algebraic Equations (DAEs). Index reduction of the DAEs, a critical step for solvability, is thereby facilitated by this approach, as detailed in Section 1.7. The combination of all these factors is needed to integrate the 3-PM model into the integrated energy system.

[2.3] The derivation, transforming concentration-based equations from Lefebvre et al. [15] into the required mass-based formulation, is provided in Section A.1.

[2.4] The rationale behind adopting these specific state variables for property calculations is elaborated in Section 1.8

2.4 Balance equations:

Mass balance for each species in the overall gas phase

$$\underbrace{\frac{\partial \vec{m}_{\mathrm{g}}}{\partial t}}_{\text{Accumulation}} = \underbrace{D_{\mathrm{g,ax}} \frac{\partial^2 \vec{m}_{\mathrm{g}}}{\partial z^2}}_{\text{Axial dispersion}} \underbrace{- \frac{1}{\varepsilon_g} \frac{\partial}{\partial z} \left(u_{\mathrm{g}} \cdot \vec{m}_{\mathrm{g}} \right)}_{\text{Advection}}$$

$$\underbrace{- k_{\mathrm{L}} a_i \cdot \left(\frac{\vec{m}_{\mathrm{g}}}{\varepsilon_g \cdot H_{i,cc}} - \frac{\vec{m}_{\mathrm{sl}}}{1 - \varepsilon_g} \right)}_{\text{G/L mass transfer}} \tag{2.3}$$

Mass Balance for each species in the slurry phase

$$\underbrace{\frac{\partial \vec{m}_{sl}}{\partial t}}_{\text{Accumulation}} = \underbrace{D_{\mathrm{sl,ax}} \frac{\partial^2 \vec{m}_{sl}}{\partial z^2}}_{\text{Axial dispersion}} \underbrace{+ k_{\mathrm{sl}} a_i \cdot \left(\frac{\vec{m}_g}{\varepsilon_g \cdot H_{i,cc}} - \frac{\vec{m}_{sl}}{(1 - \varepsilon_g)} \right)}_{\text{G/L mass transfer}}$$

$$\underbrace{+ \vec{\nu}_{\mathrm{i}} \cdot \vec{M}_i \cdot \eta_{\mathrm{cat}} \cdot \varphi_{\mathrm{S}} \cdot m_{\mathrm{cat}} \cdot r_{\mathrm{3PM}}}_{\text{Reaction}} \tag{2.4}$$

where

$$\vec{m}_g = \vec{X}_g \cdot m_g \quad \text{and} \quad \vec{m}_{sl} = \vec{X}_{sl} \cdot m_{sl} \tag{2.5}$$

and

$$\vec{X}_g = \begin{bmatrix} X_{g,\mathrm{CO_2}} \\ X_{g,\mathrm{H_2}} \\ X_{g,\mathrm{CH_4}} \\ X_{g,\mathrm{H_2O}} \end{bmatrix} \quad \text{and} \quad \vec{X}_{sl} = \begin{bmatrix} X_{sl,\mathrm{CO_2}} \\ X_{sl,\mathrm{H_2}} \\ X_{sl,\mathrm{CH_4}} \\ X_{sl,\mathrm{H_2O}} \end{bmatrix} \tag{2.6}$$

The stoichiometric coefficients $\vec{\nu}_{\mathrm{i}}$ and molecular weights $\vec{M}_i$ for CO_2 methanation are:

$$\vec{\nu}_{\mathrm{i}} = \begin{bmatrix} -1 \\ -4 \\ 1 \\ 2 \end{bmatrix} \quad \text{and} \quad \vec{M}_i = \begin{bmatrix} 0.044 \\ 0.002 \\ 0.016 \\ 0.018 \end{bmatrix} \tag{2.7}$$

where i denotes the individual species of gases. For CO methanation, the vectors $\vec{v}_i$ and $\vec{M}_i$ should be changed according to the CO methanation reaction[2.5], with X_g and X_{sl} incorporating the mass fractions of CO instead of CO_2. The reaction rate r_{3-PM} should also be adapted for CO methanation. The mass balance equations for each species reflects three coupled processes:

1. **Convective transport (advection and axial dispersion).** As gas bubbles rise, they carry their respective species axially with superficial gas velocity u_g. This forced convection appears as the advection term in the mass balance.

2. **Inter-phase mass transfer.** At the gas-liquid interface, species cross between the bulk gas and slurry phases given by:

$$k_L a \; = \; k_L \cdot a,$$

   where k_L is the gas-liquid mass transfer coefficient and a the specific interfacial area. In the gas-phase mass balance, this term appears as a sink $(-k_L a(\dots))$, and in the slurry-phase balance as a source $(+k_L a(\dots))$.

3. **Intra-slurry diffusion and reaction.** In the slurry, the dissolved species diffuse to catalyst surface sites and react. The products then return to the bulk gas phase via the same gas-liquid interface.

Working together, gas-liquid mass transfer, dissolution of the transferred species in the slurry phase, diffusion across the slurry phase and reaction at the catalyst surface govern the spatial and temporal evolution of each species in the 3-PM reactor.

2.5 Energy Balance

The energy balance can be derived as:

$$\underbrace{\rho_{\mathrm{sl}} \cdot c_{p,\mathrm{sl}} \cdot \varepsilon_{\mathrm{sl}} \cdot \frac{\partial T}{\partial t}}_{\text{Accumulation}} = \underbrace{\frac{\partial}{\partial z}\left(\varepsilon_{\mathrm{sl}} \cdot \lambda_{\mathrm{sl,eff}} \cdot \frac{\partial T}{\partial z}\right)}_{\text{Axial dispersion}} + \underbrace{\eta_{\mathrm{cat}} \cdot \varphi_{\mathrm{S}} \cdot \rho_{\mathrm{S}} \cdot r_{\mathrm{3PM}} \cdot (-\Delta h_{\mathrm{r}})}_{\text{Reaction heat}}$$

$$- \underbrace{\alpha_{\mathrm{cool}} \cdot A_{\mathrm{eff}} \cdot (T - T_{\mathrm{cool}})}_{\text{Cooling}} \tag{2.8}$$

where $\lambda_{\mathrm{sl,eff}}$ is expressed as:

$$\lambda_{\mathrm{SL,eff}} = \rho_{\mathrm{SL}} \cdot c_{p,\mathrm{SL}} \cdot D_{\mathrm{SL},ax} \tag{2.9}$$

and $D_{\mathrm{SL},ax}$ is the axial dispersion coefficient.

2.5 CO methanation and its validation is not a part of this work.

Although no explicit correlation exists for $D_{\mathrm{SL},ax}$, the one developed by Deckwer [131] is used in most publications. It is derived as:

$$D_{\mathrm{SL},ax} = 0.678 \cdot \phi_C^{1.4} \cdot U_g^{0.3} \tag{2.10}$$

where ϕ_C is the reactor diameter and U_g is the superficial gas velocity.

2.6 Hydrodynamic coefficients

In this work, all the hydrodynamic coefficients required in the balance equations for the 3-PM model are adopted from previous work by Lefebvre et al. [130] and Götz [132]. The superficial gas velocity U_g is used in several correlations (listed in Table A.3) and is calculated as:

$$U_g = \frac{\dot{V}_g}{A_{cs}}, \qquad \text{where} \quad A_{cs} = \frac{\pi \cdot \phi_C^2}{4} \tag{2.11}$$

where $\dot{V}_g$ is the volumetric flow rate, ϕ_C is the column diameter and A_{cs} is the area of cross section of the bubble column. The hydrodynamic coefficient for gas holdup (ε_{G}) is calculated (Equation A.11) using the method proposed by Behkish [133]. Lefebvre et al. [15] evaluated several holdup coefficients and found that the Behkish correlations were most suitable for the 3-PM reactor developed at EBI-ceb. Lefebvre also evaluated different correlations for $k_{\mathrm{L}}a$ and determined the correlation (Equation A.15) developed by Lemoine et al. [134] to be most suitable. In the $k_{\mathrm{L}}a$ correlation by Lemoine, the Sauter mean bubble diameter (calculated in Equation A.10) of the small bubbles is used.[2.6] The solubility of gases in the slurry medium is determined using a dimensionless Henry's law coefficient $H_{i,cc}$, which is a temperature-dependent fit (Equation A.16, Table A.2) developed by Götz et al. [135]. The reaction rate r_{3PM} is estimated using the power-law equation (Equation A.17) derived by Lefebvre et al. [15]. The overall heat-transfer coefficient α_{eff} is modelled using the Deckwer coefficient for slurry bubble columns (Equation A.18). The fluid properties like density ρ_{sl} and dynamic viscosity μ_{sl} are calculated as temperature dependent fits from the manufacturer data sheet for Marlotherm SH [123].

The liquid surface tension σ_{sl} is calculated using a temperature dependent fit derived from DBT measurements conducted by Aslam et al. [136]. The fluid properties used in the calculations are only available up to 320 °C for the slurry. Therefore, if the reaction results in higher temperatures, extrapolated properties are required in the case of the slurry to calculate the hydrodynamic parameters. All equations referenced above are collected in Table A.1, and the fixed parameters with their baseline values used in this work are listed in Table A.3.

[2.6] The bubble sizes is classified in literature into small and large bubbles. The hydrodynamic correlations are different for both. To reduce complexity in modelling, only one bubble size (small bubbles) is used in this work.

2.7 Flow-regime classification

Slurry bubble columns operate in one of three distinct hydrodynamic regimes [137]. In the homogeneous regime, gas is introduced at low superficial velocities (typically $u_g < 0.05\,\text{m/s}$), producing small, uniformly distributed bubbles. Under these conditions, coalescence is minimal, the bubble-size distribution remains narrow, and gas holdup ε_g increases linearly with u_g. Mass transfer benefits from high interfacial area and well-mixed conditions. As u_g increases beyond a transition velocity, the system enters the heterogeneous regime. In the heterogenous regime, bubble coalescence and breakup produce a broader size distribution, with large bubbles which may rise rapidly in the core and smaller bubbles which can recirculate downward near the walls [137]. Gas holdup no longer scales linearly with superficial velocity in the heterogenous regime. At still higher gas velocities especially in narrow columns, a slug or churn regime may develop. Large, bullet-shaped bubbles (slugs) that can span the column diameter. In this work, throughout the operating range and at all loading conditions, the superficial velocities ($u_g \leq 0.03\,\text{m/s}$) are low. As these velocities are far below 0.05 m/s, it can be assumed that the flow is in the homogeneous regime in all the cases.

2.8 Discretisation of PDEs

After deriving the balance equations and estimating all the hydrodynamic coefficients, the PDEs in eqs. 2.3 to 2.8 are converted into ODEs. The method of lines [138] is used to replace spatial derivatives with finite difference approximations. The general 1-dimensional discretisation scheme for the axial dispersion method used to model the 3-PM reactor is depicted in fig. 2.3.

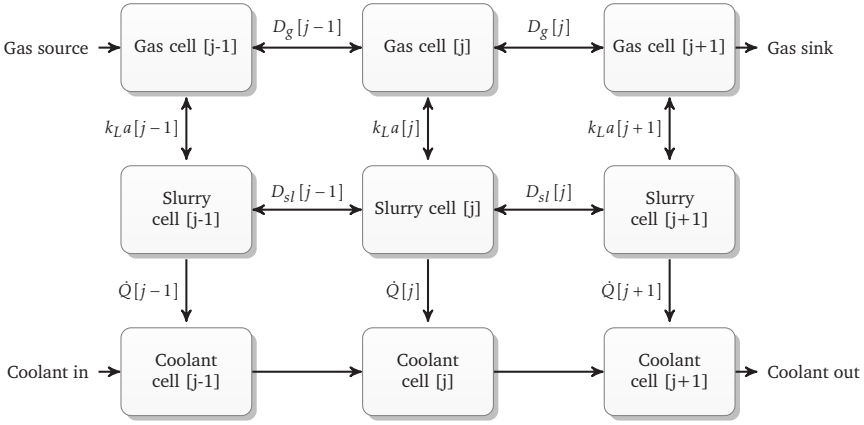

Figure 2.3: Discretisation of the axial dispersion model for the 3-PM process using a three-point grid of cells indexed spatially from $j-1$ to $j+1$. The direction from gas source to gas sink is along the reactor and the direction of mass transfer parameter k_La is assumed to be orthogonal to it.

The reactor is divided into slurry cells and gas cells surrounded by the coolant cells. The gas cells represent the bulk gas phase and the slurry cells represent the bulk slurry phase. Axial dispersion occurs within the gas and slurry cells respectively. The gas-liquid mass transfer on the other hand occurs between the gas and slurry cells. A double arrow is used to indicate the gas-liquid mass transfer in Figure 2.3 which means that the mass transfer can happen in both directions where the species (predominantly the reactants) cross over from the bulk gas phase into the slurry also from the slurry phase cross back into the bulk gas-phase (predominantly the products).

The spatial derivatives are approximated using the central differencing scheme [2.7] for the following equations:

Axial dispersion in the overall gas phase:

$$D_{\mathrm{g,ax}} \frac{\partial^2 m_{i,g}}{\partial z^2} \approx D_{\mathrm{g,ax}} \cdot V_j \cdot \left[\frac{\vec{\rho}_g(j+1) - 2 \cdot \vec{\rho}_g(j) + \vec{\rho}_g(j-1)}{dz^2} \right] \tag{2.12}$$

Axial dispersion in the slurry phase:

$$D_{\mathrm{sl,ax}} \frac{\partial^2 m_{i,sl}}{\partial z^2} \approx D_{\mathrm{sl,ax}} \cdot V_j \cdot \left[\frac{\vec{\rho}_{sl}(j+1) - 2 \cdot \vec{\rho}_{sl}(j) + \vec{\rho}_{sl}(j-1)}{dz^2} \right] \tag{2.13}$$

Advection in the overall gas phase:

$$\frac{1}{\varepsilon_g} \frac{\partial}{\partial z} \left(u_{\mathrm{g}} \cdot m_{i,\mathrm{g}} \right) \approx \frac{V_j}{2 \cdot \varepsilon_g} \cdot \left[\frac{\vec{\rho}_g(j+1) \cdot \vec{u}_g(j+1) - \vec{\rho}_g(j-1) \cdot \vec{u}_g(j-1)}{dz} \right] \tag{2.14}$$

Axial dispersion in energy balance

$$\frac{\partial}{\partial z} \left(\varepsilon_{\mathrm{sl}} \cdot \lambda_{\mathrm{sl,eff}} \cdot \frac{\partial T_{sl}}{\partial z} \right) \approx \varepsilon_{\mathrm{sl}} \cdot \lambda_{\mathrm{sl,eff}} \cdot \left[\frac{T_{sl}(j+1) - 2 \cdot T_{sl}(j) + T_{sl}(j-1)}{dz^2} \right] \tag{2.15}$$

Where $(j-1)$, (j) and $(j+1)$ are 3 random points in the spatial grid used for discretisation and i is the gas species index.

[2.7] The truncation error for the central differencing scheme is in the order of $\mathcal{O}(z^2)$ for a discretisation length z. Therefore it is given as an approximation

In the 3-PM process, the slurry and the bubbles get heated during load changes. This leads to the expansion of the multiphase mixture. The height of the expanded multiphase mixture z_{mpm}, is determined from the holdup ε_g as follows:

$$V_{sl} = V_{cat} + V_L \tag{2.16}$$

$$V_{mpm} = V_{sl} + V_g \tag{2.17}$$

$$\varepsilon_g = \frac{V_g}{V_{mpm}} \tag{2.18}$$

$$V_{mpm} = \frac{V_{sl}}{1 - \varepsilon_g} \tag{2.19}$$

$$z_{mpm} = \frac{4 \cdot V_{sl}}{\pi \cdot \phi_C^2} \cdot \left[\frac{1}{1 - \varepsilon_g} \right] \tag{2.20}$$

$$z_{cell} = \frac{z_{mpm}}{n_{cells}} \tag{2.21}$$

The discretisation step z_{cell} depends on the holdup ε_g, which in turn varies with changing operating conditions. To manage this variability effectively, a two dimensional polynomial fit (using pressure and temperature as independent variables) is developed for z_{cell}. This polynomial is derived from steady-state reactor simulations performed across various temperature and pressure scenarios where z_{cell} is calculated using the corresponding holdup values for each temperature and pressure. The polynomial fit approach for z_{cell} introduces inherent limitations, particularly extrapolation errors beyond the calibration range. Since the fit was developed using steady-state simulations, its accuracy during rapid transient conditions may be compromised, potentially affecting the prediction of multiphase mixture expansion during dynamic load shifts. To account for dynamic changes in the length of the multiphase mixture, the most effective approach would be to change the grid after each time step. Dynamic boundary changes are possible using the moving boundary method [139].

Most moving boundary techniques are based on coordinate transformations of state variables. Several mathematical operations for index reduction in Modelica require the original state variables without coordinate transformation [70]. In addition, thermodynamic state variables are also required in their unchanged form for fluid property calculations. Therefore, the moving boundary method is not used in this work.

2.9 Thermodynamic reformulation

To model the 3-PM reactor, the PDEs for the conservation equations derived in equations 2.3, 2.4, and 2.8 are converted to ODEs using the method of lines. The discretisation schemes given in eqs. 2.12 to 2.15 are used for this. Converting PDEs to ODEs alone is not sufficient to integrate the 3-PM model into the overall energy system. To integrate the equations into Modelica, the fluid properties must be calculated in the 3-PM model using the same state variables as used in the equations of state. In addition, incorporating fluid properties into the balance equations must be achieved without affecting index reduction (detailed explanation in section 1.7).

Therefore, the axial dispersion model after the corrections for discretisation step-size is reformulated as follows:

1. The mass derivatives in all the balance equations are reformulated in terms of density and volume (Equation 2.22).
2. The density derivatives are then reformulated using partial derivatives of density in pressure and enthalpy.
3. The partial derivatives, in turn are provided as explicit functions of thermodynamic state variables (p, h) (Equation 2.24).
4. Dependent properties are then calculated using the thermodynamic state variables as inputs to external EOS based tools.

The first step is to remove the mass derivative (left-hand side of eq. 2.22) and use density derivatives instead.

$$\frac{d\vec{M}}{dt} = \frac{d(\vec{\rho} \cdot V_i)}{dt} = \rho \cdot \frac{dV_i}{dt} + V_i \cdot \frac{d\vec{\rho}}{dt} \tag{2.22}$$

The control volume does not expand, $\frac{dV}{dt} = 0$ therefore $\frac{d\rho}{dt}$ is reformulated as:

$$\frac{d\vec{\rho}}{dt} = \left(\frac{\partial\vec{\rho}}{\partial p}\right)_h \frac{dp}{dt} + \left(\frac{\partial\,\vec{\rho}}{\partial h}\right)_p \frac{dh}{dt} \tag{2.23}$$

To calculate the density derivative $\frac{d\vec{\rho}}{dt}$, the partial derivatives of density at constant pressure and enthalpy are required.

Richter [89] proposed a method to calculate the partial derivatives $\left(\frac{\partial\rho}{\partial p}\right)_h$ and $\left(\frac{\partial\rho}{\partial h}\right)_p$ as explicit functions:

$$\left(\frac{\partial\rho}{\partial p}\right)_h = \frac{-T \cdot \beta^2 + \beta + \kappa \cdot \rho \cdot c_p}{c_p} \tag{2.24}$$

$$\left(\frac{\partial\rho}{\partial h}\right)_p = -\frac{\beta \cdot \rho}{c_p} \tag{2.25}$$

Where β is the isobaric expansion coefficient and κ is the isothermal compressibility. The relationships can be derived using Bridgman's tables [140]. The equations 2.22 to 2.25 are then incorporated into the balance equations 2.3, 2.4 and 2.8. This results in the final set of ODEs that can be integrated into the energy system model and solved with all other components without encountering index reduction problems.

3 Validation of numerical modelling for a three-phase methanation reactor.

The validation of the three-phase methanation (3-PM) process is critical for ensuring reactor performance, reliability, and safety under dynamic conditions encountered in practical applications. Electrolysers supplying hydrogen to the 3-PM reactors have fluctuations in H_2 production rates if they are connected to renewable power generation sources. If the hydrogen produced by the electrolysers in turn are connected to the 3-PM reactor, it is essential to evaluate whether the methanation reactor can also accommodate such fluctations resulting in frequent load shifts without compromising safety or CO_2 conversion rates. During dynamic operations involving frequent load shifts and changes in the 3-PM reactor conditions such as temperature or pressure, the mass transfer and reaction kinetics of the 3-PM process can be affected. This in turn impacts the parameters that affect safety such as reactor temperature. It also affects CO_2 conversion. Therefore, the validation of the 3-phase methanation reactor in this chapter aims to address three critical questions:

1. Can the reactor maintain safe operational parameters during frequent and sudden load shifts?
2. How is the CO_2 conversion affected under dynamic operating conditions?
3. Are the simulation results for parameters governing multiphase mass transfer and reaction kinetics (which uses empirical correlations for hydrodynamic parameters) plausible?

Considering these objectives, the validation strategy comprises three distinct analytical approaches:

1. **Validation of reactor performance during sudden load shifts**: The ability of the reactor to sustain safe operations during sudden variations in load is assessed. This involves validating the temperature distribution profile along the reactor length, as well as the CO_2 conversion rates during abrupt load shifts.
2. **Validation of simulation results along the reactor length**: The hydrodynamic parameters are evaluated along the length of the reactor (under steady state operation) to determine the spatial variation in the parameters.
3. **Validation of the reactor at extreme operating points**: The reactor is validated in steady state at both lower and higher extremes of temperature and pressure, along with multiple intermediate points.

This evaluation assesses how varying operating conditions affect reaction kinetics as well as the heat and mass transfer aspects of the 3-PM process.

3.1 Key assumptions:

In the discretised balance equations of the axial dispersion method, the CO_2 conversion in each discrete reactor segment is influenced by a sequence of processes:

- **Equilibration at the interface.** An increase in gas-phase partial pressures of H_2 and CO_2 results in higher solubility at the gas-liquid interface.
- **Transport across gas-liquid interface** Dissolved species traverse from the bulk gas phase across the gas-liquid interface. The rate of mass transfer is expressed by the coefficient $k_L a$.
- **Diffusion and reaction.** Once inside the slurry phase, the dissolved H_2 and CO_2 diffuse through the liquid layer surrounding catalyst particles. The reaction finally takes place at the catalyst surface and the products formed re-enter the bulk gas phase through the same gas-liquid interface.

The reactor model used in this work is built upon the following assumptions:

- **Ideal mixing within cells.** Each discretised axial segment is assumed to be perfectly mixed without internal concentration gradients (for both bulk gas and slurry phases).
- **Uniform superficial velocity.** All the individual species are assumed to have the same superficial velocity within each cell.
- **Using empirical correlations for bubble dynamics.** Gas-phase holdup and Sauter mean bubble diameters are calculated using empirical correlations. Therefore aspects such as dynamic bubble coalescence and breakage are not explicitly modelled.

3.2 Validation of reactor performance during load shifts

Plausible future operations of the 3-PM reactor involve operating under load transients which can affect temperature distribution, CO_2 conversion and heat transfer within the reactor. To evaluate operation under transient conditions, the 3-PM reactor is simulated for a load shift from 50% of full load to full load within a very short time (34 s). The same load shift is carried out experimentally, and the results of the simulations and experiments are compared. Figure 3.1 shows the schematic of the experimental setup used to validate the 3-PM numerical model.

Experiments were performed by Sauerschell et al. [129] in measurement campaigns during the course of this work. In the experimental setup (Figure 3.1), R100 is the methanation reactor. Inlet flow is monitored at the measuring points (marked FIRC). The thermostat PU E601 controls the reactor temperature. Heat exchanger marked HE 101 condenses DBT which falls back into the reactor and HE 300 condenses the residual gas (that comes out of HE 101) to remove steam and traces of any remaining DBT vapour. Gas composition at input and output is measured using micro gas chromatographs (μ-GC, marked QIR).

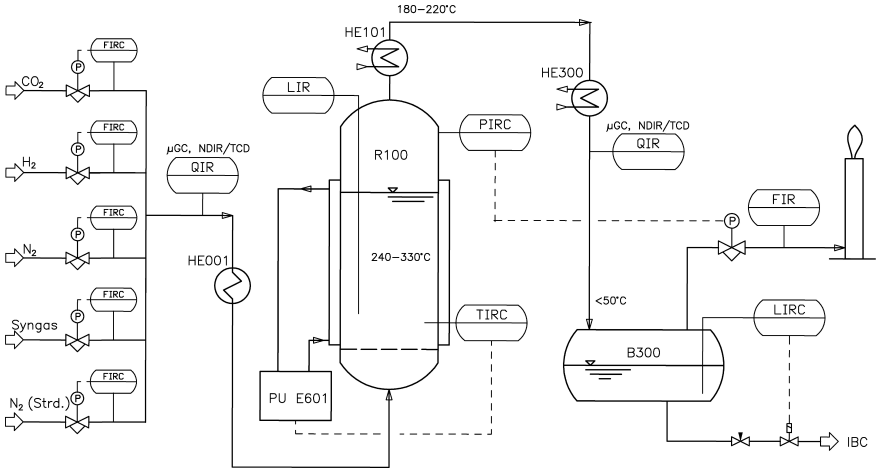

Figure 3.1: Experimental setup at the 3-PM reactor developed by EBI-ceb used for validating the numerical model. Image source: Sauerschell et al. [129].

The measurement campaigns were conducted for different loading conditions (both ramp-up and ramp-down of the reactor) and the results are used to validate the numerical 3-PM model. The inlet gas mixture comprised of an above[3.1] stoichiometric mixture of hydrogen and carbon dioxide ($S = 1.05$). The parameters used in the load shift experiments using the 3-PM plant at EBI-ceb are listed in table 3.1.

Load Shift parameters

The input ramp used for the load shift validation study is depicted in Figure 3.2. The ramp profile consists of a step increase from 50% to 100% load over a period of 34 seconds, followed by sustained operation at full load. The load shift starts at 600 s and an increase in temperature caused due to the reaction enthalpy is absorbed by both the fluid in the reactor and the coolant system.

3.1 Above in this case implies a stoichiometric ratio above 1

Table 3.1: Parameters of the test reactor at EBI-ceb

Parameter	Value
Catalyst mass	6.5 kg
Liquid (DBT) mass	62.63 kg
Slurry volume	0.0785 m^3
Slurry level at no load	1.478 m
Hydrogen volume flow rate $\dot{V}_{H_2}$ at 50% load	20 $m^3\,h^{-1}$
Hydrogen volume flow rate $\dot{V}_{H_2}$ at 100% load	40 $m^3\,h^{-1}$
Plant capacity P_{PtG}	100 kW
Input gas composition χ_{in}[NTP]	80% H_2, 20% CO_2
Reactor diameter ϕ_C	0.26 m

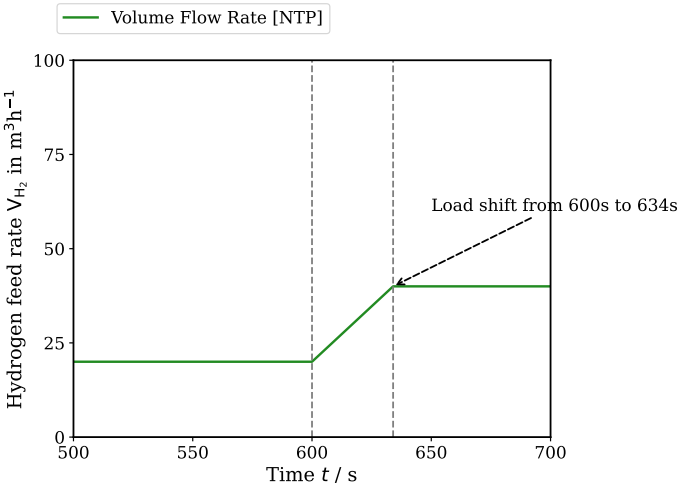

Figure 3.2: Load shift conditions for validating the 3-PM numerical model.

Dynamic changes during load shifts: Temperature

A comparison between experimental measurements and simulation results shows that the temperature increase of the reactor after a sudden load change is minimal (Figure 3.3).

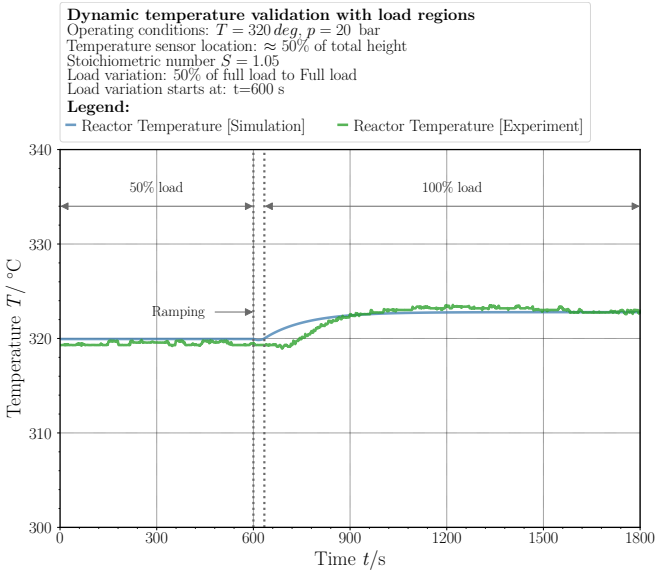

Figure 3.3: Temperature response of the middle sensor (experiment) and corresponding cell (simulation) during and after the load shift. The cooling thermostat recirculates the cooling fluid at a constant inlet temperature of 310 °C during the load shift.

The steady states before and after the load changes are in agreement between the simulations and the experiment. However, the experimental data show a significant delay (about 120 s) in the onset of the temperature peak relative to the validation curve. The delayed temperature response observed in the experiments may be attributed to multiple factors. First, the actuation time of the control valve during ramping up can postpone the actual change in reactant flow rate, thus delaying the initiation of the temperature rise. In addition, the transport time required for gas bubbles to traverse the reactor length can introduce a latency in heat generation.

Finally, the thermal inertia and thickness of the temperature sensors[3.2] can lead to further slow-down in recorded readings, dampening rapid thermal variations and shifting the peak position.

3.2 The experiment used 10 temperature sensors along the length of the reactor, with the sensor used for validation located near the middle. The temperature value from the sensor in the middle of the reactor was used as the reference. Therefore the temperature value near the middle of the discretised column is used to validate all the simulations.

Dynamic Changes During Load Shifts: CO_2 Conversion

Similar to the temperature profiles, the point at which CO_2 conversion decreases after the ramp-up phase in the experiment occurs approximately 52 s later than the simulation result (Figure 3.4).

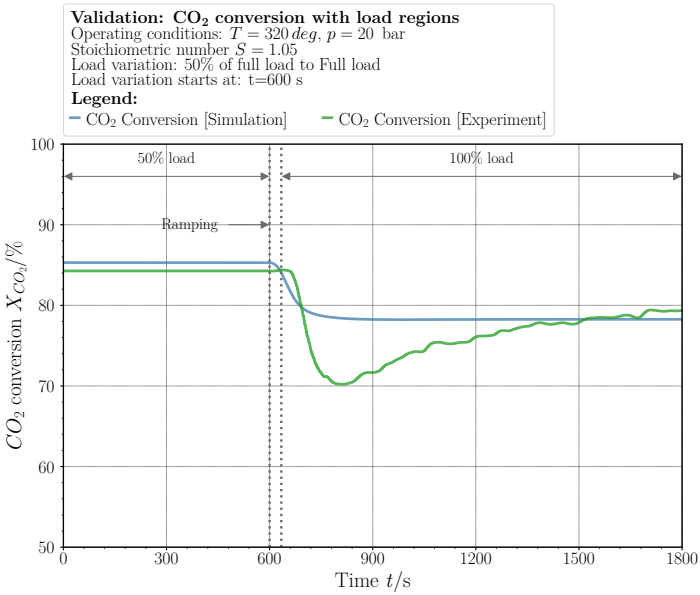

Figure 3.4: CO_2 conversion of the middle reactor segment (experimental) and corresponding cell (simulation) during and after the load shift. The cooling thermostat recirculates the cooling fluid at a constant inlet temperature of 310 °C during the load shift.

In the experiments, it was also observed that the CO_2 conversion initially decreases below its pre-shift steady state value before rising to the final steady state. In contrast, the simulated profile shows a smooth, monotonic decrease (from the pre load-shift steady state to the post load-shift steady state). The transient dip in CO_2 conversion followed by a recovery to the final steady state is not seen in the simulated results. The differences in CO_2 conversion profiles can be attributed to disparities in solubility and mass transfer rates between CO_2 and H_2.

After a load shift, an excess of dissolved CO_2 will be present in the slurry phase, whilst H_2 is slower to dissolve and diffuse in the slurry phase. The Sauter mean bubble diameters and gas holdups are also distinct and different for CO_2 and H_2. These differences impact the mass transfer from the bulk gas phase into the slurry phase, temporarily until both CO_2 and H_2 attain stoichiometric conditions in the slurry phase. This causes an under-stoichiometric CO_2 conversion in the slurry phase until a sufficient quantity of H_2 is also available. This manifests as an initial dip followed by a recovery in the CO_2 conversion profile.

Temperature Profile along the Reactor

A spatially resolved analysis of reactor performance is essential to understand how temperature and gas holdup varies with axial position and to verify model predictions. It has to be noted that in the axial dispersion method only a single spatial dimension (z axis) is used which means that the radial phenomena like radial dispersion and bounceback cannot be captured.

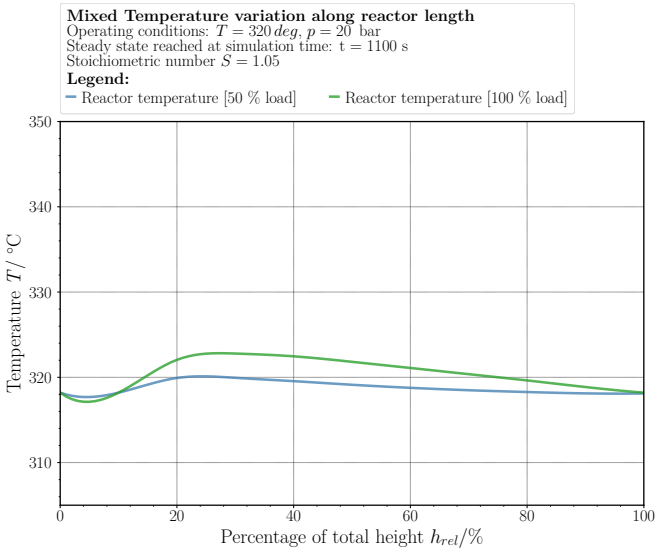

Figure 3.5: Axial temperature profile before and after the load shift. The cooling thermostat recirculates the cooling fluid at a constant inlet temperature of 310 °C during the load shift.

The temperature along the reactor remains nearly isothermal under both steady and transient conditions. Prior to the load shift, the maximum deviation from the mean temperature is approximately 1.7°C before and about 3.5°C after the load shift. This modest spike during transient operation indicates that the reactor effectively dampens thermal runaways, thereby maintaining safe operating limits. The temperature spike is predominantly in the initial part of the reactor. The reason for this will be seen in subsequent results that the mass transfer from the bulk phase to the liquid phase (see section 3.3) also has the analogous increase predominantly in the first part of the reactor.

Gas Holdup along the Reactor

The gas holdup decreases progressively along the length of the reactor due to the combined effects of mass transfer at the gas-liquid interface, dissolution of the gas in the slurry phase, and the subsequent reaction, which results in a reduction in the volume of CO_2.

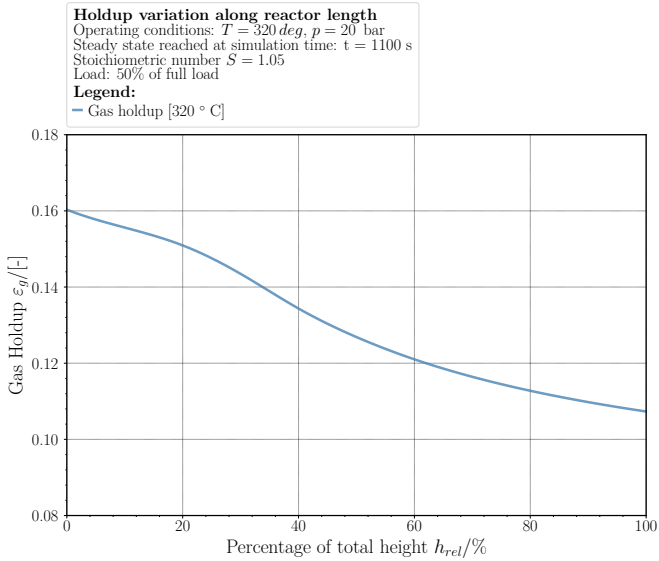

Figure 3.6: Axial gas holdup profile along the reactor length. The hold-up profile is not a function of the reactor length as it may appear from the figure. The reduction in the profile is due to the combined effects of advection, mass transfer at the gas-liquid interface, dissolution of the gas species in the slurry phase and reaction.

A reduction in gas holdup (Figure 3.6) indicates effective reactant consumption and a diminishing interfacial area for mass transfer in the latter stages of the reactor.

3.3 Validation Across the Operating Spectrum

In the methanation reaction, mass transfer occurs initially from the gas phase through the gas-liquid interface into the slurry phase. In the slurry phase, the reaction kinetics influences the final CO_2 conversion. The products which are formed then cross back into the gas phase via the gas-liquid interface. All these processes are influenced by the operating temperatures and pressures. To simulate the reactor across its full operational spectrum, it is essential to evaluate the underlying mass transfer and reaction kinetics at various temperature and pressure points within its operating limits.

So far in this work, validation efforts have focused on simulating the reactor at the upper operational limits of 320 °C and 20 bar. Therefore, the reactor is evaluated at the operating limits with pressures ranging from 6 to 20 bar and temperatures from 260 to 320 °C. The results can be used to evaluate how gas-liquid mass transfer rates and reaction kinetics in combination influence overall CO_2 conversion.

The mass transfer across the gas-liquid interface can be defined using the equation:

$$\dot{m}_{GL,i} = k_L A_i \cdot (C_{GL,i} - C_{sl,i}) \cdot V_{sl} \tag{3.1}$$

where:

- i is the species index
- $C_{GL,i}$ is the concentration at the gas-liquid interface
- $C_{sl,i}$ is the concentration in the slurry phase
- $k_L A_i$ is the rate of mass transfer across the gas-liquid interface for each species
- V_{sl} is the slurry volume

The gas-liquid interface concentration also depends on how much gas gets dissolved in the liquid medium which in turn is affected by the partial pressure of the gas and the Henry coefficient of the gas in the liquid medium.

The relationship can be defined as:

$$C_{GL,i} = \frac{p_i \cdot M_i}{H_i} \tag{3.2}$$

where:

- H_i is the Henry's coefficient for species i in the liquid,
- p_i is the partial pressure of species i,
- M_i is the molar mass of species i.

Evaluation Parameter for Mass Transfer

The ratio between the gas liquid mass transfer and solubility $\frac{k_L a}{H_{i,cc}}$ is used in this work to evaluate the efficiency of mass transfer from the bulk gas phase to the slurry phase. The volumetric mass transfer coefficient $k_L a$ quantifies the rate of mass transfer from the gas phase to the slurry phase. Higher $k_L a$ implies a high rate of gas-liquid mass transfer. The Henry coefficient $H_{i,cc}$ on the other hand determines gas solubility at the gas-liquid interface. A high $\frac{k_L a}{H_{i,cc}}$ value indicates enhanced mass transfer and solubility. The increase may result from either improved rate of mass transfer $k_L a$ across the gas-liquid interface or higher gas solubility $H_{i,cc}$ or both. Conversely, a low ratio of $\frac{k_L a}{H_{i,cc}}$ indicates poor mass transfer or low gas solubility or both. Therefore, combining $k_L a$ and $H_{i,cc}$ into a single ratio $\frac{k_L a}{H_{i,cc}}$ provides a clearer understanding of how much reactants have crossed the gas-liquid interface and are finally available in the slurry phase for reaction.

Influence of temperature on CO_2 conversion

Simulation results indicate that the ratio $\frac{k_L a}{H_{i,cc}}$ is higher for CO_2 compared to H_2, and this ratio increases with temperature for both species (Figure 3.7). At elevated temperatures, both viscosity and surface tension decrease, resulting in smaller gas bubbles. The smaller bubbles offer a larger surface-area-to-volume ratio, increasing the gas–liquid interfacial area and thereby resulting in a higher gas–liquid mass transfer coefficient. Higher temperatures slightly affect gas solubility causing minor variations in the dimensionless Henry coefficient $H_{i,cc}$ (Figure 3.8).

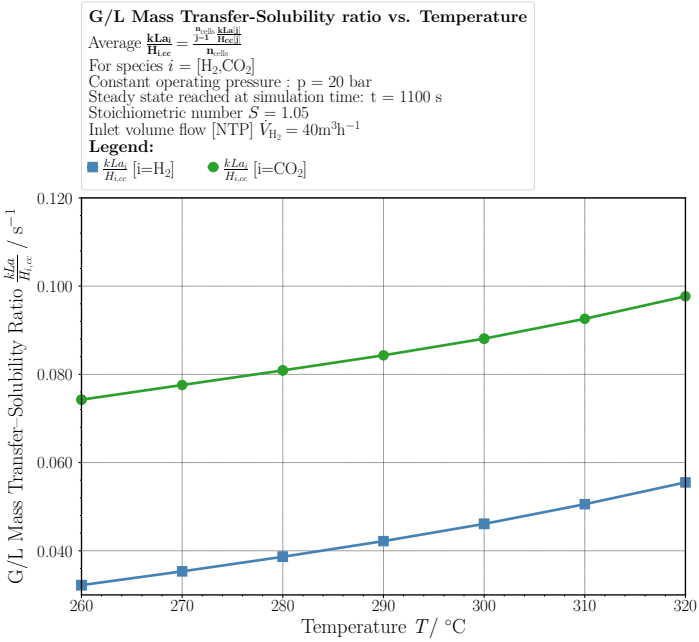

Figure 3.7: Variation in $\frac{k_L a}{H_{i,cc}}$ at higher temperatures.

Within the investigated temperature range (260–320,°C), the Henry coefficient for each species varies by about 10% (Figure 3.8), while value of $k_L a$ experiences a much larger variation thereby resulting in a net increase in $\frac{k_L a}{H_{i,cc}}$. Effective mass transfer into the slurry phase alone is not sufficient for high CO_2 conversion. For this to happen, the reaction rate within the slurry phase must also be adequate. The catalytic reaction rate is described by a power-law kinetic equation (Equation A.17), which exhibits increased reaction rates at higher temperatures. At high temperatures, both mass transfer and reaction rates increase, resulting in enhanced CO_2 conversion. In contrast, at lower temperatures, a modest reduction in gas-liquid interface mass transfer can be observed. But the reaction rates are reduced to a greater extent.

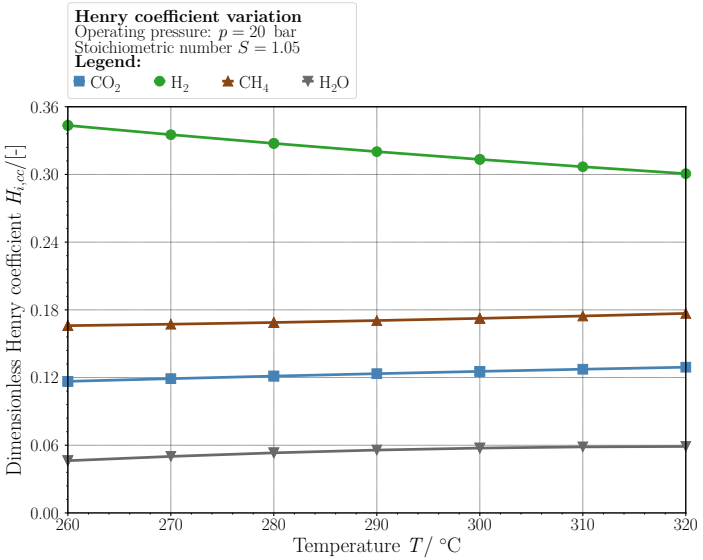

Figure 3.8: Temperature dependence of dimensionless Henry coefficient for each species.

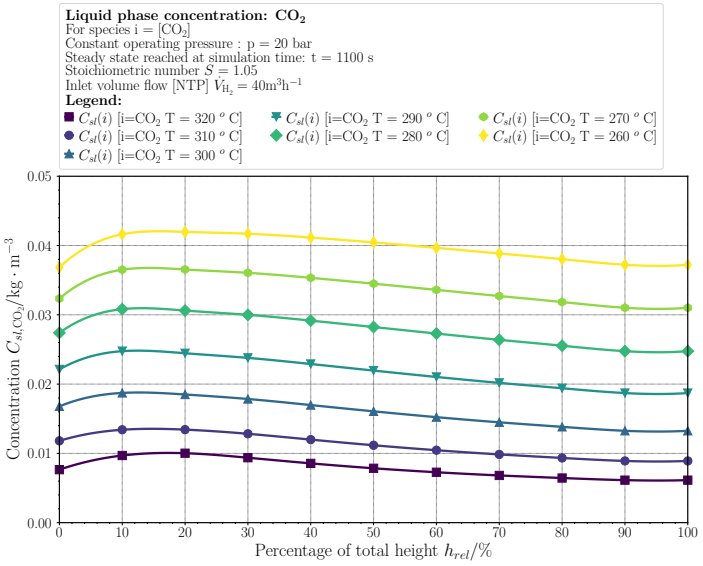

Figure 3.9: Liquid phase CO_2 concentration along reactor length at 260 °C and 320 °C.

Since the reduction in reaction rate exceeds the reduction in gas-liquid mass transfer at lower temperatures, the reactant species that have already crossed over from the gas phase into the slurry phase but remain unreacted will accumulate within the slurry phase. At higher temperatures, the gradient of CO_2 conversion along the reactor length is higher. This is due to the combined effect of improved gas-liquid mass transfer and better reaction rates. In contrast, Figure 3.9 reveals higher concentrations of unreacted CO_2 at lower temperatures, confirming that despite adequate mass transfer, lower reaction rates cause accumulation in the slurry. From the results, it can be concluded that for CO_2 conversion, at lower temperatures the reaction kinetics rather than gas–liquid mass transfer constitute the rate-limiting step. At higher temperatures[3.3], the reaction kinetics and mass transfer rates are both sufficiently high.

Influence of Pressure on CO_2 conversion

Adjusting reactor pressure while maintaining a constant inlet flow rate alters the superficial gas velocity. Increasing pressure at constant feed rate reduces superficial velocity while decreasing pressure elevates it.

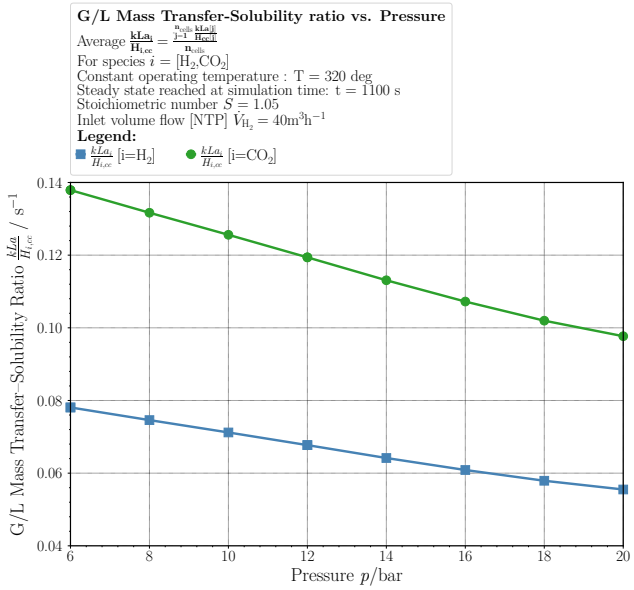

Figure 3.10: Effect of reactor pressure on the solubility-normalised gas-liquid mass transfer coefficient ($\frac{k_L A_i}{H_{i,cc}}$) at constant temperature (320 °C) and constant hydrogen loading (40 m^3h^{-1} at NTP).

3.3 Property data for DBT is available only up to 593 K. Beyond this, numerical extrapolation may yield unphysical values (e.g., negative surface tension), limiting the simulation range. The recommended maximum bulk temperature for DBT is 623 K.

Load shift experiments at constant pressure showed that higher superficial gas velocities[3.4] resulted in reduced CO_2 conversion (Figure 3.4). A plausible explanation is that higher superficial gas velocities decrease bubble break-up. Therefore, bubbles become larger and have smaller specific surface areas relative to volume which reduces $k_L a$. Similarly, when the operating pressure is increased at constant feed rate, the superficial gas velocity decreases which reduces $\frac{k_L A_i}{H_{i,cc}}$ (Figure 3.10).

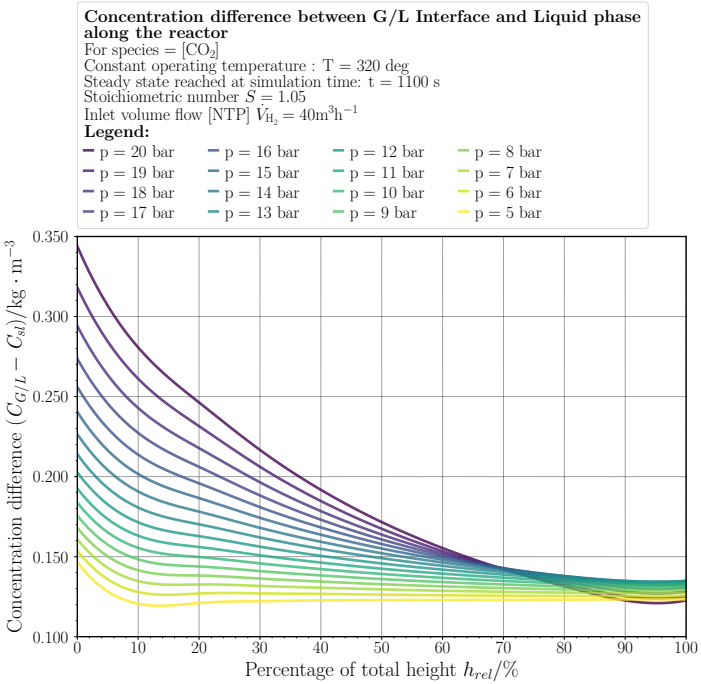

Figure 3.11: Axial concentration difference ($C_{GL} - C_{sl}$) for CO_2 along the reactor at various pressures at a fixed temperature (320 °C). Greater differences at higher pressures enhance the overall driving force for mass transfer.

But in this case, despite the reduction in $\frac{k_L A_i}{H_{i,cc}}$, the CO_2 conversion increases at higher operating pressures. To explain the increased CO_2 conversion despite reduced $\frac{k_L A_i}{H_{i,cc}}$, the concentration gradient between the gas-liquid interface and the bulk liquid phase was evaluated. The volumetric mass transfer across the gas-liquid interface depends on the concentration difference ($C_{GL,i} - C_{sl,i}$) as shown in Equation 3.1. This concentration difference increases with pressure because solubility is directly proportional to the partial pressure of the gas species (Equation 3.2). Raising the partial pressure of the species increases gas solubility at the gas-liquid interface which in-turn elevates $C_{GL,i}$ significantly.

3.4 Higher superficial velocities in the load shift experiments were achieved by increasing the input feed rate at constant pressure.

The increased concentration at the gas-liquid interface drives mass transfer due to a higher concentration gradient ($C_{GL,i} - C_{sl,i}$). The concentration profile along the reactor height at different pressures illustrates this (Figure 3.11). It can be seen that at higher pressures, the concentration difference ($C_{GL,i} - C_{sl,i}$) is up to 3 times larger at the highest pressure compared to the lowest pressure which compensates for the reduced gas-liquid mass transfer rate. It can also be seen that the concentration difference is more pronounced at the initial stage of the reactor and gradually diminishes towards the end. At the reactor inlet, the gas phase contains maximum concentrations of both CO_2 and H_2, resulting in the highest gas-liquid interface concentration. However, as the bubbles travel along the reactor and the reactants are progressively consumed and converted to products, their concentrations decrease. Higher reactor pressures (e.g. 20 bar) result in larger concentration differences between the gas-liquid interface and the slurry phase. This increased concentration difference compensates for the reduced gas-liquid mass transfer rate, causing improved mass transfer which results in improved CO_2 conversion.

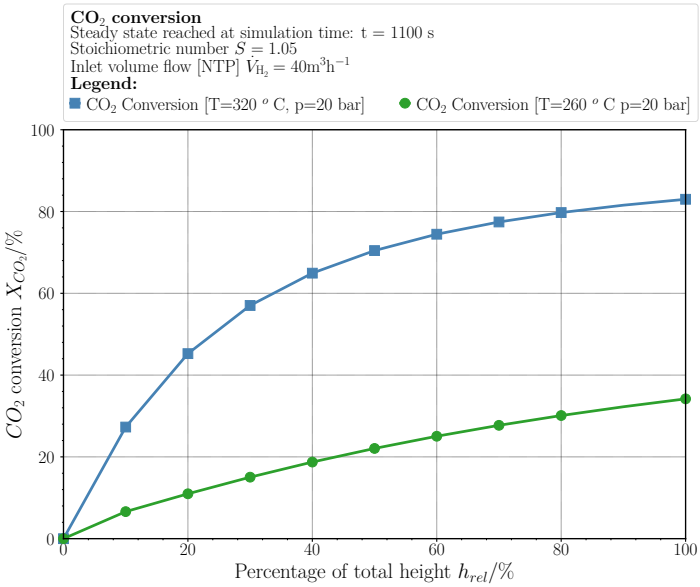

Figure 3.12: CO_2 conversion along reactor length at higher and lower temperatures with high pressure maintained.

It can also be inferred from Figure 3.12 and Figure 3.13 that low pressure (6 bar) at high temperature (320 °C) results in superior CO_2 conversion compared to high pressure (20 bar) at low temperatures (260 °C). This is because higher temperatures enhance both the reaction rate and gas-liquid mass transfer while elevated pressures benefit only mass transfer across the gas-liquid interface. Therefore, decreasing the temperature has a more limitig effect on CO_2 conversion than decreasing the pressure.

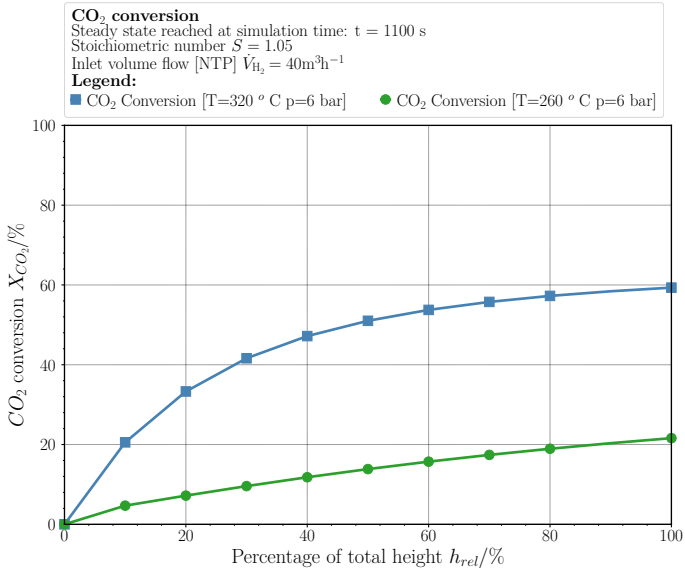

Figure 3.13: CO_2 conversion along reactor length at higher and lower temperatures with low pressure maintained.

Gas-Phase mass fraction Variations Along the Reactor

The mass-fraction profiles along the reactor demonstrate that the steepest gradients occur when both temperature and pressure are maximised. In particular, the profile obtained at 320 °C and 20 bar exhibits a markedly sharper decline in CO_2 and H_2 and correspondingly rapid rise in CH_4 and H_2O relative to the other conditions (Figure 3.16). Even when compared individually to the high-pressure, low-temperature case or the low-pressure, high-temperature case, the high-temperature, high-pressure case results in the highest CO_2 conversion (Figures 3.14 and 3.15). It is evident that increasing either the temperature or the pressure in isolation leads to a significant steepening of the CO_2 conversion gradient along the reactor length. These variations in gradient directly influence the overall CO_2 conversion, with steeper profiles corresponding to more complete consumption of reactants and higher methane yields at the reactor outlet. This correlation holds across all four data sets (Figures 3.14 to 3.17). The most favourable CO_2 conversion is achieved under combined high-temperature and high-pressure conditions, where reactant depletion is most rapid and product formation is most pronounced (Figure 3.16). Under these operating conditions, the CO_2 conversion profile approximates exponential decay, with most of the CO_2 conversion occurring in the initial section of the reactor. In contrast, at low temperatures and pressures, the profile is closer to linear, indicating more uniform conversion throughout the reactor (Figures 3.16 and 3.17). Therefore, if the operations must be maintained at lower temperatures and pressures, extending the reactor length could be advantageous in order to achieve a comparable overall conversion rate.

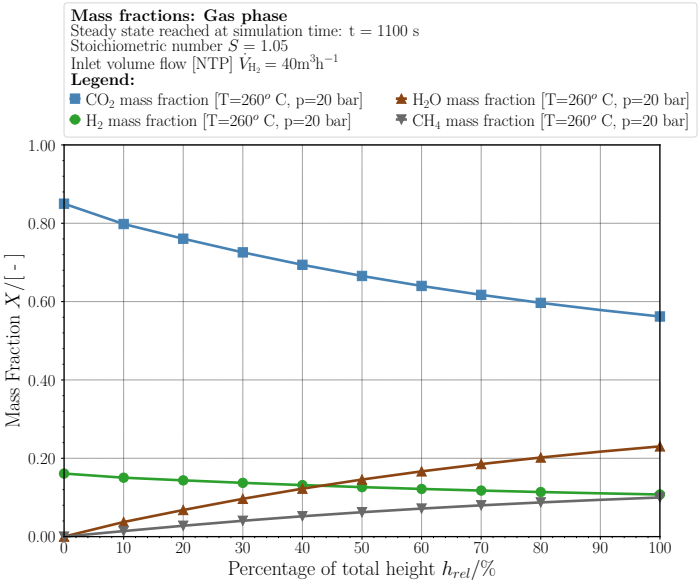

Figure 3.14: Gas-phase mass fraction changes along reactor at low temperature (260 °C) and high pressure (20 bar).

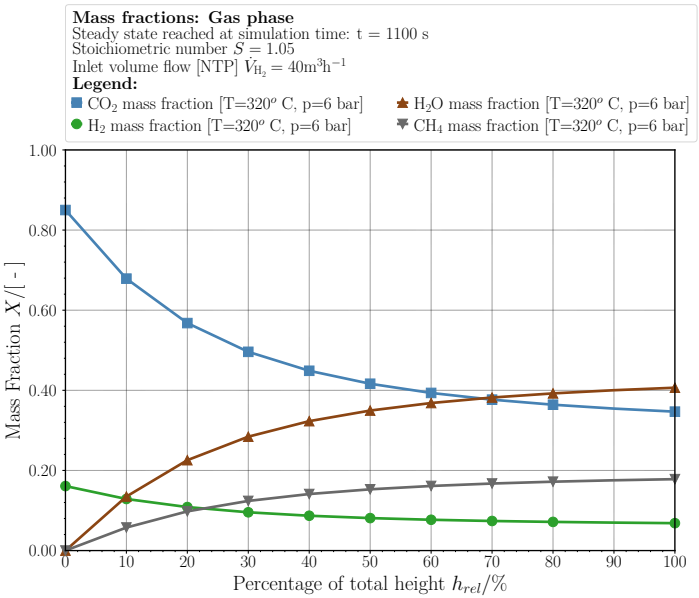

Figure 3.15: Gas-phase mass fraction changes along reactor at high temperature (320 °C) and low pressure (6 bar).

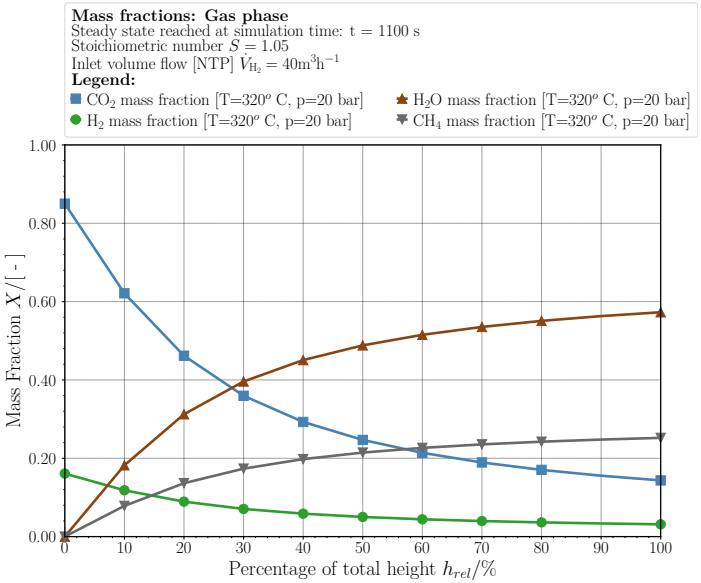

Figure 3.16: Gas-phase mass fraction changes along reactor at high temperature (320 °C) and high pressure (20 bar).

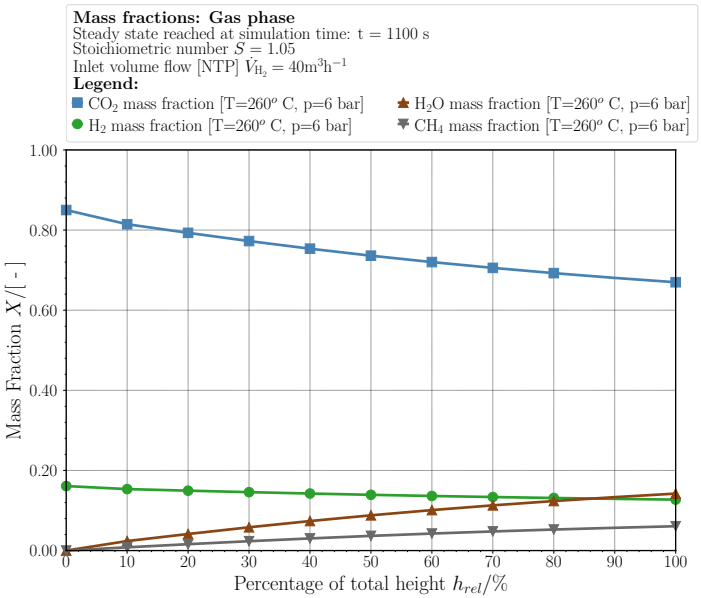

Figure 3.17: Gas-phase mass fraction changes along reactor at low temperature (260 °C) and low pressure (6 bar).

3.4 Steady-State Validation

The final phase of model validation was conducted to assess the effects of temperature and pressure on CO_2 conversion across the entire operational envelope. Measurement campaigns carried out by Sauerschell et al. [129] targeted intermediate operating points (between the operating extremes). The first campaign involved measuring CO_2 conversions across a temperature range of [260 °C, 320 °C].

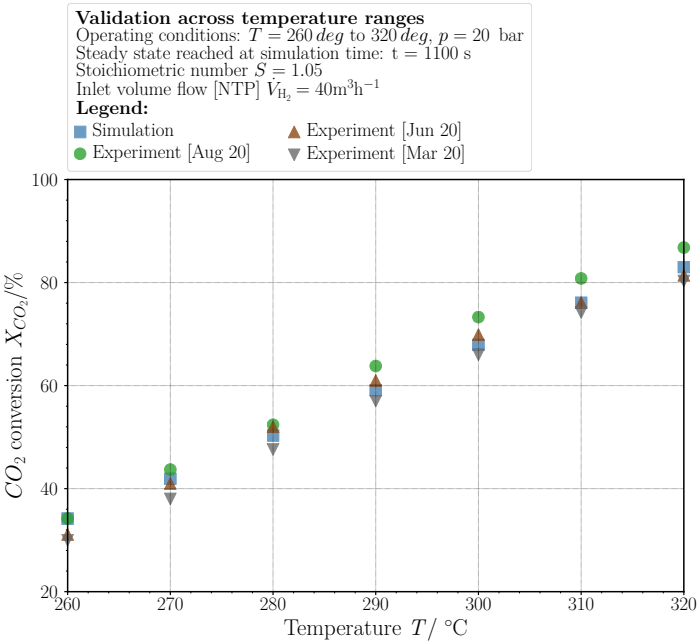

Figure 3.18: Validation of simulation versus experimental CO_2 conversion across temperature ranges ([260 °C, 320 °C]) at constant pressure (20 bar). Measurement campaigns conducted in March, June, and August 2020.

Results of the simulations demonstrated good agreement with the experimental results from the measurement campaigns (as shown in Figure 3.18). The simulated steady state CO_2 conversions closely matched experimental data across the entire temperature range. The second campaign focused on measuring steady-state CO_2 conversions across an operating pressure range of [6 bar, 20 bar]. The simulation results showed the same trend in comparison to the experimental data (Figure 3.19). However, at the lower end of the pressure range, the relative errors were larger, reaching a maximum of approximately 15%. This deviation can be attributed to the limitations associated with the two-dimensional polynomial fit used for slurry discretisation in the axial-dispersion method (explained in Section 2.8).

The two dimensional polynomial fit was calibrated over a relatively narrow temperature window [260 °C, 320 °C] but a much broader pressure range ([6 bar, 20 bar]). Consequently, at lower pressures, the polynomial approximation tends to overestimate the effective slurry height used in discretising the balance equations, resulting in inflated CO_2 conversion predictions.

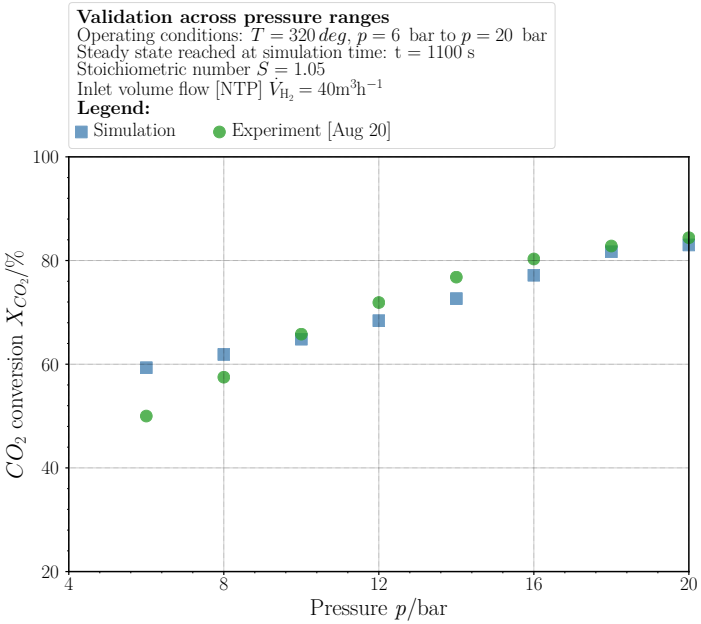

Figure 3.19: Validation of simulation versus experimental CO_2 conversion across pressure ranges ([6 bar, 20 bar]) at constant temperature (320 °C). Measurement campaign conducted in August 2020. Deviations at lower pressures reflect challenges in accurately capturing wide pressure variations.

3.5 Summary, Additional Influencing Factors, and Evaluation of Validation Objectives

The validation explored the 3-phase methanation (3-PM) reactor across diverse operational conditions addressing the influences of temperature and pressure on mass transfer, reaction kinetics, and overall CO_2 conversion. It was found that the operating temperatures and pressures impacted both mass transfer and reaction kinetics, which in turn affected the overall CO_2 conversion. Validation outcomes resulted in three main inferences. Firstly, while validating reactor safety and stability under sudden load shifts (Figures 3.2 and 3.4), deviations were observed between the experiments and simulations. Some causes were identified for this discrepancy, such as actuator response, bubble transport latency, and thermal inertia of the sensors.

However, steady-state conditions following transient phases closely matched predictions and despite the delays, the transients in reactor temperature during dynamic load shifts were not high enough to be deemed unsafe. In addition, experimental and simulation results for the steady state CO_2 conversion across various temperature and pressures (Figures 3.12, 3.13, 3.18 and 3.19) demonstrated strong alignment. Although the steady state results for temperature variations were highly accurate, some deviations at lower pressures were observed and were attributed primarily to challenges in discretising axial dispersion models. The third validation objective was to assess the plausibility of simulation results for multiphase mass transfer and reaction kinetics. The uniform temperature distribution along the reactor indicates that hot-spots are unlikely during dynamic operation. Gas holdup patterns also matched stoichiometric expectations. Certain physical phenomena were intentionally simplified in the numerical model. Radial dispersion, vortex formation, catalyst-induced turbulence, and variations in gas-phase molecular diffusion (From the bulk gas phase to the gas-liquid interface) were excluded from this one-dimensional axial dispersion model.

These simplifications may have influenced local accuracy but were essential to maintain computational feasibility of simulating the overall energy system. Further, the discretisation does not use moving boundary methods to account for dynamic expansion of the slurry phase during load shifts. Instead, it uses a fixed slurry height to discretise the balance equations. This approach is computationally effective but may not capture all transient phenomena accurately. In summary, the validation addresses two main questions regarding safety and overall CO_2 conversion under different operating conditions. Reactor safety under dynamic conditions was confirmed and the predicted CO_2 conversions closely matched experimental results. Discrepancies observed in all the cases could be explained. It can be concluded that the validated numerical model is a middle ground between physical accuracy of the 3-PM process and computational feasibility of simulating the component as a part of an integrated energy system. This balance enables reliable prediction of reactor behaviour under both steady-state and transient conditions, but also enables its integration into a broader integrated energy system.

4 Energy system integration

The aim of this chapter is to aggregate the overall energy system from individual components. To do this, it is necessary to develop boundary conditions and clustering methods specific to the energy systems used in this work. The energy system comprises three types of components.

1. Components adapted without any modifications from existing Modelica libraries
2. Components such as building energy systems that need to be modified and their level of detail adapted to fit into the integrated energy system
3. Components that are not available in Modelica libraries and need to be modelled completely

This chapter explains the structure of the overall energy system used in this work. Some energy system components, such as photovoltaic and wind turbine models, are already available in the Modelica libraries. Others, such as building energy systems, are significantly modified for the purposes of this work.

The chapter also includes methods for calculating standard load profiles, which are used in buildings and electric mobility. The components are finally aggregated into the overall energy system.

The final part of this chapter explains the control system used in this work. The control system is designed to maximise the utilisation of surplus power to produce renewable gases.

4.1 Structure of the integrated energy system

The components of the energy system[4.1] in Figure 4.1 can be categorised by their function (generation, distribution, consumption, sector coupling), energy source (electricity, gas, heat), and sector (mobility, buildings, industry). Some dynamic models used in the energy system are taken from existing libraries without modifications.

For power generation, the wind and PV models are adapted from the Modelica Buildings library [75, 87]. The weather data has a resolution of 1 h and is calculated using the Wilcox and Marion [141] procedure available as a standard module in the Modelica Buildings library [87].

[4.1] In this context, the energy system specifically refers to a system designed to analyse dynamic interactions between its constituent components. High spatial resolution networks, such as electric, gas, and district heating grids, are analysed separately.

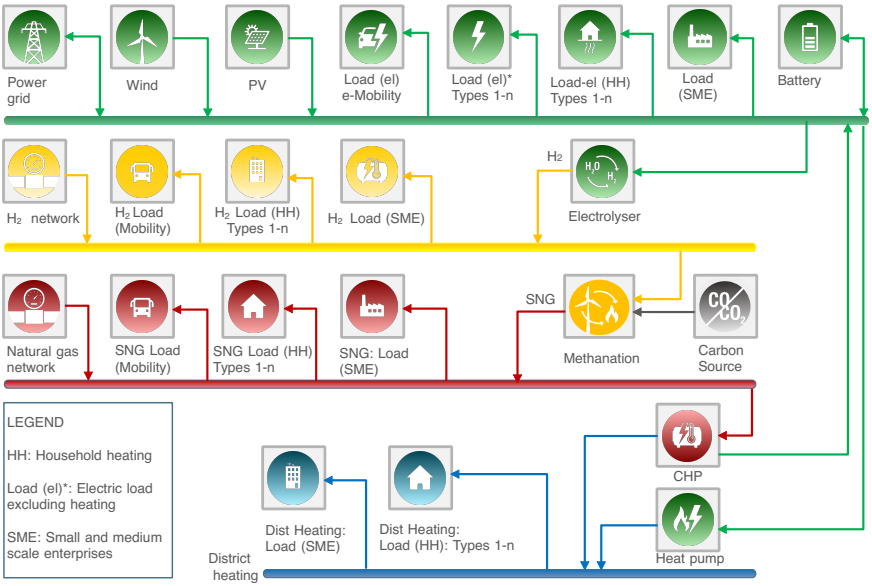

Figure 4.1: Concept of energy system showing the power sector in green, gas sector in orange, H_2 sector in yellow and district heating in blue

The weather files specific to the location are downloaded from the Ladybug EPW weather map [142]. The components of the TIL Library [88, 89, 104] are used to model the district heating network. Battery storage is modelled using the ideal battery defined in the Buildings library [87], and thermal storage is adapted from the TIL library [104]. Fluid property calculations in all thermofluid models use the TIL Media Suite [104]. All the control systems used are taken from the Modelica Standard Library [69]. All Modelica models are developed in the Dymola software [143]. Table A.4 lists the Modelica component models used in this work for energy distribution and storage. Table A.5 lists the programming tools used for data handling in this work.

4.2 Building Energy Systems

The overall load in the energy system is divided into three major sectors:

1. Load from buildings
2. Load due to mobility
3. Load from small and medium-scale enterprises

Calculating the load for buildings is a challenging task as there are several types of buildings within the same region. The International Building Performance Simulation Association (IBPSA) issues guidelines for modelling building in Modelica [144]. Modelica libraries like the AixLib [76], Buildings [87] and IDEAS [145] are based on these guidelines. These libraries focus on the detailed dynamic simulation of buildings and their HVAC systems. However, the high level of detail these building models makes grouping the buildings difficult[4.2]. In this work the buildings are classified as follows:

1. Building energy systems connected to the electric grid only
2. Building energy systems connected to the gas grid for heat and electric grid for power
3. Building energy systems connected to the H_2 grid for heat and electric grid for power
4. Building energy systems connected to the district heating for heat and electric grid for power

To use building models for sector coupling, the load profiles must be satisfied using different energy carriers (electricity, H_2 or SNG). In addition, the total number of buildings using each energy carrier also determines the load on the corresponding network. The gas distribution networks for H_2 and SNG are separate in the energy system model. Several studies have measured the efficiencies of heating devices. Pieper et al. [146] estimated the COP of the heat pump to be between 3.1 and 3.5. Xu et al. [147] calculated the COP values of the absorption heat pumps to be between 1.17 and 2.45 for various temperature ranges. Shen et al. [148] showed that the COP of the single-stage air-source heat pump varies from 1.7 to 2.6. Ahrens et al. [149] achieved a system COP of 4.1 for hybrid absorption–compression heat pumps. Jesper et al. [150] calculated COP values between 3 and 6 for standard compression heat pumps using R717 as refrigerant. Although detailed heat-pump models are available in Modelica, such a level of detail is not practical in this work as several buildings with heat pumps need to be aggregated. The are modelled instead using polynomial fits (Eq. 4.1) for COP [151, 152] based on δT[4.3].

$$COP = \begin{cases} 6.08 - 0.09 \cdot \Delta T + 0.0005 \cdot \Delta T^2, & ASHP \\ 10.29 - 0.21 \cdot \Delta T + 0.0012 \cdot \Delta T^2, & GSHP \\ 9.97 - 0.20 \cdot \Delta T + 0.0012 \cdot \Delta T^2, & WSHP \end{cases} \tag{4.1}$$

where ASHP are air-source heat pumps. WSHPs are water-source heat pumps, and GSHPs are ground-source heat pumps, which are used in larger applications, such as district heating.

4.2 The computational complexity of detailed building models can increase simulation time by orders of magnitude when scaled to district or city level, implying simplified approaches for grouping the buildings in the energy system models.

4.3 δT is the temperature difference between source and sink. The source and sink differ according to the type of heat pump (air source, water source or geothermal source).

In buildings with heat pumps, COPs are calculated using the temperature difference between the sink and environment of the heat pump (δT). To calculate δT, air-source heat pumps use ambient and target room temperatures, while water-source heat pumps use geothermal source temperature as ambient. In building energy systems using gas as the energy carrier, fixed efficiency values of 95 % are used as documented in real-life use cases [153]. H_2-based heating devices are not in widespread use at present. Studies have also looked at adapting existing boilers to use either H_2 or H_2 mixed with natural gas [154]. Other studies indicate the efficiencies of the hydrogen boiler to be between 90 % and 94% [155–157].

In this work an efficiency of 90 % is used for all H_2 boilers. Local heating devices are absent in building energy systems connected to the district heating network (Figure 4.2). Jangsten et al. [158] surveyed and found an average radiator supply and return temperature of 64 °C and 42 °C in fourth-generation district heating systems. Residential radiators operate at a temperature range of 30–70 °C. Gong and Werner [159] estimated supply temperatures between 120 °C and 85 °C and return temperatures around 55 °C for the district heating network which is used in this work.

4.3 Load profiles

The power generation components, such as wind and PV models, only require weather data, plant capacities, and conversion efficiencies to generate load profiles. Load profiles of buildings, on the other hand, are strongly influenced by outdoor temperature, building type, and occupant behaviour patterns [160, 161]. Buildings can be grouped into standard types either depending on the age of the building or their application to simplify the modelling process. For heat and electric loads, Brown et al. [5] generated electricity demand profiles using the Open Power System Data Project [162], which is a modified version of the ENTSO-E load data [163]. More detailed profiles, incorporating consumer behaviour, were developed by Pflugradt et al. [164] and Linssen et al. [160]. Other profiles are available for technologies such as night-storage heaters [165], micro-CHP [166], and heat pumps [167]. For buildings modelled in this work, the BDEW standard load profiles (SLP) [168, 169] are used.

The BDEW building classifications are listed in [168, 169]. The BDEW load profiles consist of a temperature-dependent sigmoid function and a linear part:

$$h(\vartheta) = \left[\frac{A}{1 + \left[\frac{B}{\vartheta - \vartheta_0} \right]^C} + \mathrm{D} \right] + \max \begin{pmatrix} m_H \cdot \vartheta + b_H \\ m_W \cdot \vartheta + b_W \end{pmatrix} \tag{4.2}$$

where ϑ_0 is a constant temperature specific to each profile[4.4]

[4.4] A fixed value of 40 °C is used for ϑ_0 in all the calculations.

$$Q_{day} = h(\vartheta_{alc}) \cdot KW \cdot F_{WD} \tag{4.3}$$

where ϑ_{alc} is the weighted average of temperature for the last three days calculated using the equation

$$\vartheta_{alc} = \frac{\vartheta_D + 0.5 \cdot \vartheta_{Day-1} + 0.25 \cdot \vartheta_{Day-2} + 0.125 \cdot \vartheta_{Day-3}}{1 + 0.5 + 0.25 + 0.125} \tag{4.4}$$

and KW is a temperature- and SLP-specific customer value calculated from the equation:

$$JVP = \sum_{i=1}^{365} h_{SLP}(\vartheta_i) \cdot KW \tag{4.5}$$

where JVP is the yearly cumulative gas consumption in kWh. Empirical parameters A, B, C, D, m_H, m_W, b_H, b_W vary according to the type of building and are listed in [168, 169]. Similar profiles are available for electrical load, but the classification of buildings is different. The energy system in this work uses both electrical and heating load profiles. As the load profiles are specific to the type of buildings, the building types and the total number of buildings belonging to each type must be known for each region. This is given as a user input to the energy system model. Load profiles are also required in the mobility sector, where the dynamic loads primarily depend on user behaviour, such as vehicle charging times and driving patterns.

In electric mobility, aggregated synthetic load profiles for mobility systems developed by Schäuble et al. [170] are used in this work. The electric mobility load profiles used in this work are different for electric vehicles with and without fast charging and are aggregated from measured values for different charging stations in Germany [170]. Load profiles are not available for gas mobility or industrial units. This is because they are location-specific and cannot be generalised. Therefore, both gas-based mobility and industries are classified using the BDEW standard type, GHD.[4.5]

Figure 4.2 shows the different building energy systems used in this work. All BES models comprise a demand block that uses dynamic load profiles[4.6] supplied by different heating devices. The supply is regulated by PID controllers.

[4.5] The standard classification of the industrial load GHD (Gewerbe, Handel, Dienstleistung) used in the German literature can be translated as SMEs. Due to a lack of data, all industrial loads in this work are classified as SMEs.

[4.6] In all buildings the electrical components like lighting, appliances, and auxiliary devices have dedicated load profiles and are different from their primary heating load profiles. The Figure 4.2 shows only the heating load pfofiles.

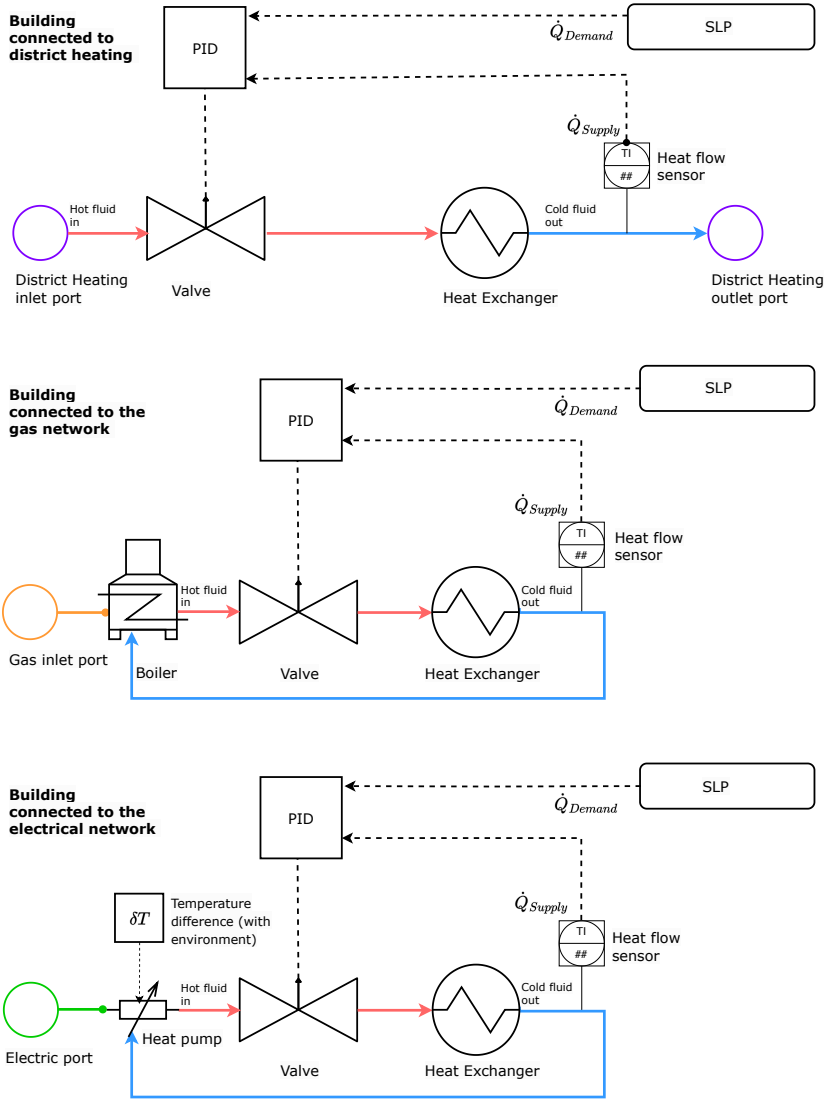

Figure 4.2: Schematic representation of building energy systems connected to the district heating network (top), the gas network (middle) and the electricity network (bottom).

4.4 Control system

The de-central energy system includes components for energy demand, conversion, storage and sector coupling. Düpmeier et al. [171] consider the use of Supervisory Control and Data Acquisition Strategies (SCADA) systems for control, monitoring and visualisation at the Energy Lab of KIT [172–175]. In this work, a similar real-time monitoring and control system is not attempted, as the energy system model uses simplified network topologies. Here, the control strategy is based on economic dispatch, where operational control is based on minimisation problems using parameters from the energy system.

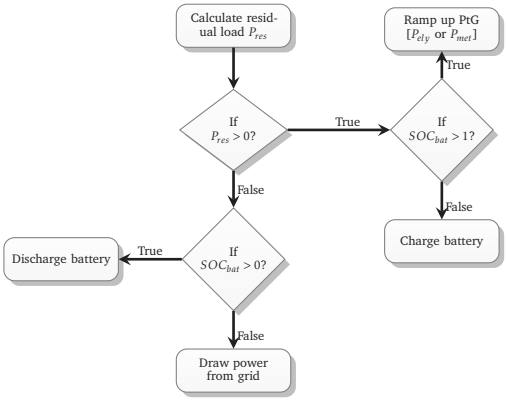

Figure 4.3: Flowchart for residual load and battery management

Similar control strategies based on economic dispatch have been investigated for electric grid systems [176], integrated energy systems with conventional generators and CHPs [177, 178], integrated energy systems with a high share of solar PV [179], and coupled gas and electric grids [180–184]. The control strategy used in this work, based on minimising surplus power generation, is shown in Figure 4.3. Two separate sets of objectives are developed for local and global control. At the local level, for each component of the energy system, the PID controllers ensure that the demand is always met. Tolerance limits are also set for operating parameters such as pressure and temperature for hydraulic components, and voltage and current for electrical components, and they are maintained at all times. The global control strategy involves minimising surplus power generation and converting excess renewable power to gas. Minimising surplus power production is only one of several control strategies that can be applied. Other strategies such as demand-side management [165, 185] and cost minimisation [176, 178, 180, 181, 183] are also possible. In this work, the control strategy based on minimising surplus power production is preferred (Figure 4.3). This is because minimising surplus power production reduces the chance of curtailment and enables PtG operation to make maximum use of the control reserve market, which in turn can minimise the cost of H_2 or SNG produced.

5 Spatio-temporal complexity in the overall energy system

The analysis of sector coupling requires two different modelling approaches. The dynamic system model captures the temporal evolution of the energy system, simulating the interactions between the energy system components across different time scales. In contrast, the network model is used to simulate energy distribution across infrastructure such as multi-nodal networks (electricity, gas or district heating), focusing on topology and spatial relationships between components and the distribution of energy. However, the network models are mostly static with no inherent dynamic capability to analyse transient phenomena in the components.

To enable the analysis of sector coupling across both temporal and spatial domains, a co-simulation framework is developed in this chapter. This interface acts as an intermediary layer, allowing bi-directional communication between the energy system model and the network model. The framework implements de-multiplexing functionality that disaggregates aggregated state variables from the dynamic system model into distributed variables. These variables are then mapped to multiple nodes in the network model. The interface also handles multiplexing operations that consolidate the distributed results from the network model simulation back into the aggregated variables required by the dynamic system model. Time management in the co-simulation framework is implemented through a master-slave pattern. The co-simulation interface acts as the master-slave coordinator, controlling the execution sequence of both models. When one model is simulating, the interface pauses the other model to maintain temporal consistency.

5.1 Topology simplification using clustering

The purpose of an energy system model is to simulate the dynamic interactions between different energy system components. In reality, these components are connected to the gas, electricity and district heating networks. They are also distributed over several spatial points. The dynamic model cannot handle such high spatial resolutions. Therefore, in order to ensure that the energy system model and the distributed network models are simulating the same energy system, the scattered energy system components in the network model need to be grouped into representative clusters and then used in the energy system model. A typical network topology has different nodes and links. The links may sometimes form loops, especially in district heating networks.

A representative topology of the full-resolution network is used in the energy system model. Bode [186] evaluated two methods to reduce network complexity of the full-resolution network [187, 188] and preferred the method developed by Loewen [187] as it can handle loops in the network. Buildings vary widely in terms of age, type of use and energy consumption patterns. Industries also have specific load profiles depending on the industrial processes used. In the network model, the buildings and industries are distributed across different nodes of the network. A major challenge in simplifying the network for sector coupling is to preserve the variability of different building types and industrial units when reducing the number of nodes. A clustering method that only considers the location of buildings aggregates loads across multiple nodes and uses the combined cumulative load in the simplified network. However, the variability due to different building types, the heating appliances used in them and the fuels used in the heating appliances is lost in the process. As variability is essential to evaluate sector coupling in the energy system model, a new clustering method is needed. This clustering method groups the buildings according to their types and the heating appliances used in them. Therefore, the variability in the building classifications and heating device types are not lost in the energy system model.

In this work, the following three classifiers are used to cluster the scattered buildings in the network model and use them in the energy system model without compromising on variability:

1. **Load profile:** Each building is assigned a standard heat and electric load profile [168, 169].
2. **Heating device:** Each building is allocated an internal heating device to connect them to their respective networks.
3. **The total number of units:** The demand of each group is the dynamic load in individual buildings multiplied by the total number of buildings in the group as given in Equation 5.2 to Equation 5.1.

The total number of buildings in the network model n_b can be grouped according to standard load profiles as:

$$n_b = \sum_{i=1}^{15} n_{BES(i)} \tag{5.1}$$

where index i is the building type index and $n_{BES(i)}$ is the number of buildings corresponding to each of the 15 standard load profiles (for each type). The number of buildings $n_{BES(i)}$ using each standard load profile must be provided as inputs in the energy system model. The 15 categories of buildings are listed in the BDEW load calculation guidelines [168, 169]. The total load of the building sector is calculated in eq. 5.2 as:

$$P_{heating} = \sum_{s=1}^{3} \sum_{k=1}^{15} n_{BES(i)} \cdot P_i \tag{5.2}$$

P_i is the standard load profile corresponding to each building type, and $P_{heating}$ is the combined dynamic load in all three sectors (Single Family Homes (HEF), Multi-Family Homes (HMF) and Small and Medium-scale Enterprises (SME)).

In the mobility sector, aggregated profiles defined by Schäuble et al. [170] for fast and regular charging are used in this work.

$$P_{mobility} = \sum_{evt=1}^{2} n_{EV(i)} \cdot P_i \tag{5.3}$$

where s is the sector index (HEF, HMF, SME) and evt is the EV type (with and without fast charging).

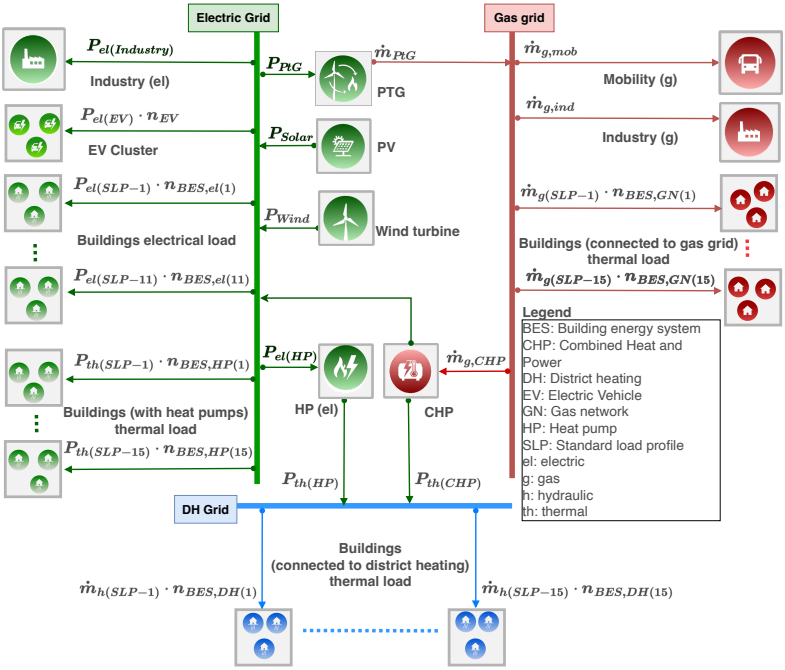

Figure 5.1: Clustering method to connect groups of buildings of particular types to the corresponding networks. The heat pumps connected to the houses and the district heating grids are of different capacities and therefore they are counted separately.

5.2 Co-simulation of dynamic and network models

Although energy systems could be modelled with simplified topologies as shown in Section 5.1, multi-nodal network models with high spatial resolution are often required[5.1]. The dynamic model simulates energy system components over time scales ranging from seconds to days. The network tool analyses stability of individual nodes (connection points) and links (transmission elements). A co-simulation framework is therefore required as an interface between the two tools for them to be simulated together. While a simplified reference network model exists in Modelica for transmission and distribution networks [189], it cannot replace dedicated network modelling tools. Most network tools are quasi-static and do not have the capability to handle the dynamics of individual components. Trying to incorporate the features of the network model into the dynamic model or vice versa is not a reliable strategy. The models must work independent of each other in the co-simulation framework, and their communication must be synchronised.

In this work, the co-simulation framework uses Application Programming Interfaces (APIs) to interact with individual tools (Figure 5.2). The APIs are developed in Python, and they can set parameters in the individual tools and also get parameters from them. To interact with the dynamic model, the Functional Mock-up Interface is used. Functional Mock-up Interface, abbreviated FMI, is a set of free standards for the model exchange and co-simulation of dynamic systems. The standards define a container and an interface for data exchange with dynamic simulation models using a combination of XML files, binaries and C code [190].

The containerised form of the Modelica model is called a Functional Mock-up Unit (FMU). In this work, the open-source co-simulation tool MOSAIK [191] is used as a higher-level interface to integrate all the APIs. MOSAIK manages the simulation time steps and the interactions between each API (Figure 5.2). The information flows between the APIs in two directions: from the energy system model to the network tool and from the network tool back to the energy system model. Two sets of parameters are used to exchange information between the APIs.

From the dynamic energy system model to the network tool, a vector of control parameters is passed (Figure 5.3). The network stability flag is then passed back from the network tool to the energy system model. Figure 5.3 depicts the variables passed when coupling the electrical network with the dynamic energy system. It uses two control parameters $[P_{PtG}]$ and $[P_{CHP}]$. After each time step, the energy system tool generates the arrays $[P_{PtG}]$ and $[P_{CHP}]$ based on the control system defined in Figure 4.3. The MOSAIK simulator first passes them from the energy system model into the network tool. Power-flow analysis is then performed in the network tool to analyse network stability. The stability conditions are user-defined and different for each de-central energy system.

5.1 In energy network modelling, nodes represent physical connection points such as substations in electricity networks and compression stations in gas networks, through which energy can be distributed to buildings. Links represent the physical connections between nodes, e.g. transmission lines in electricity networks, pipes in gas and heat networks.

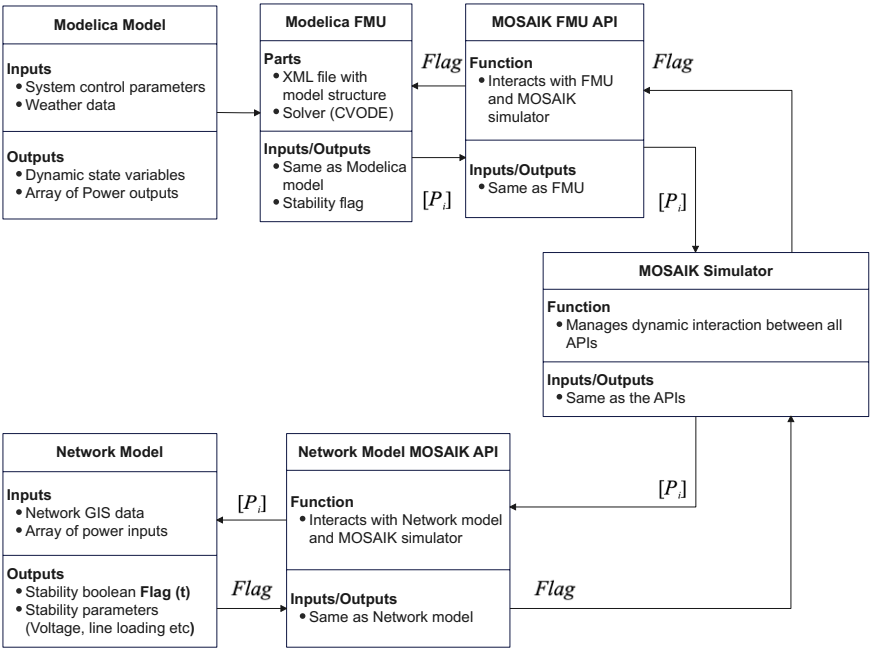

Figure 5.2: The co-simulation framework with APIs to communicate with individual tools and the simulator to manage all the APIs

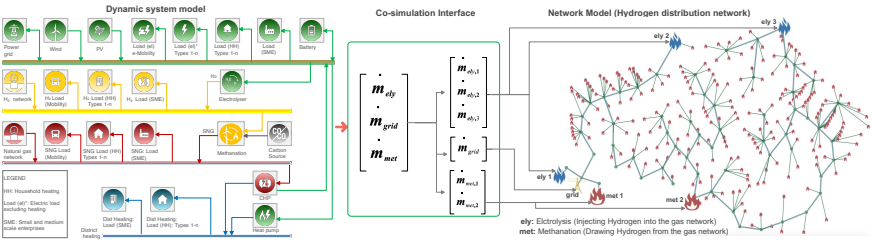

Figure 5.3: Passing variables from the dynamic energy system model to the network model using the co-simulation interface

In general, frequency or line loading is used to define stability in electrical networks, whereas gas and district heating networks use pressures and temperatures. In all the network models, two conditions must be satisfied to consider the network simulation a success:

1. The power-flow analysis (for the electrical network) or equivalent parameter stability analysis of the network tool (pressure stability across pipelines in the gas network or temperature stability in the district heating network) should converge.

2. User-defined stability conditions must be met throughout the network.

A Boolean flag variable is true if both these conditions are satisfied. Time management between different APIs is demonstrated in Figure 5.4. If either the power-flow does not converge or the user-defined stability conditions are breached, the flag is false, and the simulation stops.

The time steps ($t_{i+1} - t_i$ in Figure 5.4) involved in coupling the energy system model to the electrical network are different from those needed in the gas network or the district heating grid. It is not recommended to analyse multiple network tools in the same co-simulation, as it is computationally expensive to co-simulate all the components using the shortest time step. Conversely, an increase in the time step will prevent features of electrical networks from appearing in the simulations. For this reason, separate co-simulation APIs were developed to couple the energy system to the power, gas and district heating networks, respectively.

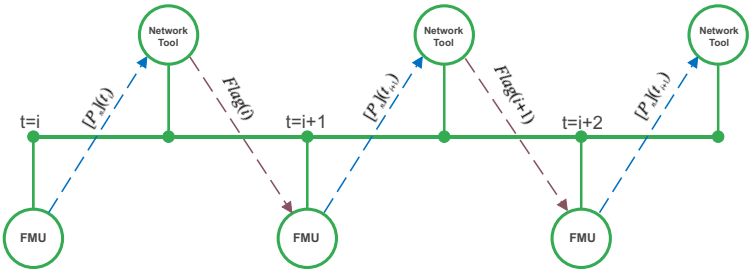

Figure 5.4: Time management between the network model and the energy system model within the co-simulation framework

In this work, the APIs have been modelled for pandapower [192] to analyse electrical networks and STANET [193] for gas and district heating grids. Preliminary testing for the co-simulation framework using power grids was carried out using the Oberrhein network, which is an electrical network based on open-source data [192]. Similarly, the co-simulation framework for gas and district heating grids has been tested using real networks separately in the RegenZell project [194].

6 Simulating energy scenarios

Modelling future energy systems requires a detailed assessment of which components and technologies are likely to become relevant in the future. These prospective developments are mapped in the so-called “energy scenarios” that analyse the changes in energy mix and technologies needed to make energy systems sustainable. Evaluating the impact of implementing the technologies from the energy scenarios at the level of de-central energy systems is crucial, as demand, renewable energy potential, and weather may vary considerably for each system.

6.1 Energy scenarios

Energy scenarios can be defined in general as policy guidelines analysing plausible combinations of energy carriers and associated technologies that can lead to sustainable energy systems in the future. Energy scenarios are interpreted in this chapter as projections of the share of renewable energy carriers and their associated technologies in each sector[6.1] which can make de-central energy systems sustainable. Table 6.1 presents an overview of energy scenarios that outline possible trends in future energy systems[6.2]. The scenarios are compiled from established national and sector-specific studies [195–199]. Each scenario defines the shares of renewable energy carriers and the associated technologies[6.3] needed to integrate these carriers into their respective sectors.

6.1 Interpretation of "Sector": In this chapter, a sector is interpreted as residential buildings, mobility or industry that cumulatively account for the annual energy demand (both heat and electricity) in a de-central energy system. The energy demand of the sector is in turn met by appliances using various energy carriers. The share of these energy sources is defined in the scenarios.

6.2 All scenarios are projected for the year 2045.

6.3 For example, the energy carrier hydrogen can be used in technologies like fuel cells in the transport sector, or electricity can be used for residential heating using heat pumps.

Table 6.1: Generalised overview of the trends according to various energy scenarios. The quantification of the shares of each energy carrier and their adaptation to de-central energy systems is explained in section 6.4.

Scenario	Trend	Mobility	Industry	Buildings
BMWK-LFS [195]				
TN-el	Heavy use of electricity	High BEV share, electric freight	Direct electrification	Heat pumps preferred
TN-PTG/PTL	Heavy use of synthetic fuels	Moderate BEVs, synthetic fuels for freight	SNG preferred	SNG preferred
TN – H_2	Heavy use of H_2	Moderate BEVs, H_2 for freight	H_2 preferred	H_2 preferred
DENA [198]				
KN-100	Balanced mix	High BEVs, H_2 for freight	Mixed electrification, SNG, H_2	Heat pumps preferred
Agora [197]				
KN2045	Strong electrification	High BEV share, electric freight	Direct electrification	Heat pumps preferred
Ariadne [196]				
Mix scenario	Mixed energy portfolio	High BEVs, H_2 for freight	Mixed electrification, H_2	Heat pumps preferred
Electrification	Strong electrification	High BEV share, electric freight	High electrification	Heat pumps preferred
H_2	Heavy use of H_2	High BEVs, synthetic fuels for freight	H_2 preferred	Heat pumps preferred
E-Fuels	Heavy use of synthetic fuels	Moderate BEVs, H_2 for freight	SNG preferred	Heat pumps preferred
Road Map Gas (RMG) [199]	Heavy use of synthetic fuels	Moderate BEVs, H_2 for freight	SNG preferred	Heat pumps preferred

The scenarios can be broadly categorised into three groups:

- **All-electric scenarios:** These scenarios focus on direct electrification through technologies like heat pumps in buildings and battery-electric vehicles in mobility.
- **Gas-based scenarios:** They focus on H_2 and SNG as renewable energy carriers. The renewable energy carriers are produced using PtX technologies like methanation and electrolysis and used in devices like fuel cells and gas-based heating systems.
- **Mixed scenarios:** Focus on both electrification and renewable gases, maintaining flexibility through diversified use of energy carriers and technologies.

The objective of this chapter is to evaluate the energy self-sufficiency[6.4] of a de-central energy system if the energy carriers and their associated technologies described in the scenarios are implemented. Implementation in this context means parametrising the energy system by changing the energy carriers according to the scenarios, i.e. changing the number of corresponding appliances using the energy carriers connected to each sector.

6.4 Self-sufficiency in the context of this chapter means the dependence (or lack thereof) on external transmission networks (in the case of electricity) and transport networks (in the case of gases) under dynamic operating conditions like intermittent power production and fluctuating demand.

To assess the impact of these changes on self-sufficiency, the energy system is simulated to estimate the share of renewable power, synthetic natural gas (SNG) or hydrogen (H_2) that can be produced locally, with the remainder drawn from the respective transmission networks. The analysis also explores the trade-offs between implementing the all-electric and gas-based scenarios in the de-central energy system.

6.2 Parametrising the de-central energy systems according to energy scenarios

To analyse the impact of energy scenarios in future de-central energy systems, a methodology is required that can parametrise the energy system model both in terms of the changes in the energy carriers predicted by the scenarios and in terms of regional variations in the renewable energy potential. To parametrise the energy system model in terms of the energy carriers prescribed in the scenarios, the energy system model must be adapted by changing the number of components using the respective energy carriers. To parametrise the system in terms of renewable energy potential, the capacities of the wind and PV plants must be set in the energy system model. The capacities of the PtX components (electrolysis and methanation plants) must also be set according to the scenarios. Once all the capacities are set in the model, the energy system is simulated to evaluate the interaction between the generation, demand and storage components and to assess in real-time how much of the annual heat and electricity demand is met locally and how much is drawn from the connected transport networks. Irrespective of the scenario chosen, all energy system components must also maintain system stability[6.5] during dynamic operation.

The components of the energy system model that need to be parametrised can be broadly divided into three categories:

- **Generation**: Generation[6.6] components include local renewable power generation components such as wind and PV plants.
- **Demand**: Demand-side components are the end consumers of energy. The demand side can be divided into sectors like residential buildings and SMEs which in turn are served by appliances using different energy carriers like H_2, renewable power or SNG.
- **PtX components**: The PtX components are used for sector coupling to produce energy carriers from renewable power. The PtX components like electrolysers and methanation units are also used for seasonal storage.

6.5 The design tolerances and safety limits for operating temperatures, pressures, voltages, etc. in each component must always be adhered to.

6.6 Only the local wind and PV plants are considered generation components. The PtX components used to convert excess renewable power into storable energy carriers are not considered as components for generation. The connections to the power transmission network and gas and H_2 transport networks for imports in case demand cannot be met locally are also not counted among the generation components.

All three categories of components need to be individually parametrised to adapt the energy system model to each scenario. Different data sources are needed to parametrise the components. The generation components depend on the local renewable energy potential and weather conditions. Therefore, the renewable energy potential must be available to parametrise them. The demand side and PtX components, on the other hand, are parametrised based on a combination of census data and scenario data sets, as explained in the following sections. The methodology to parametrise the energy system model according to the scenarios can be divided into the following main steps:

1. **Define renewable power generation profiles:** Determine the installed capacities for wind and PV in each region and combine them with site-specific weather data to generate time-dependent power generation profiles.

2. **Break down annual energy demand by sector:** Distribute annual heat and electricity demand of the region across the three main sectors: (i) Single-Family Homes (HEF), (ii) Multi-Family Homes (HMF) and (iii) Small and Medium-scale Enterprises (SME). The percentage of the total annual energy demand that each sector needs is determined using the sector-specific energy ratios obtained from the census or other data sources such as sector-specific energy consumption or the number of buildings per sector in the region.

3. **Redistribute sector-wise energy demand among energy carriers:** Redistribute[6.7] the demand in each sector between the energy carriers: H_2, SNG, electricity (el) and district heating (DH) by changing the total number of appliances using these carriers according to the scenarios. The technology powering the district heating system is also changed according to the scenario. Heat pumps are used in all-electric scenarios, while CHPs are used for district heating in gas-based scenarios.

4. **Create dynamic load profiles:** After the annual heat and electricity demands are first split according to each sector and further redistributed according to each energy carrier, time-resolved standard load profiles are generated. The profiles use measured temperature data, empirical coefficients, and usage patterns specific to the building type. The resulting load profiles, generated at hourly resolution for a full year, form the dynamic boundary conditions required to initialise all the demand-side components in Modelica.

5. **Set the capacities of PtX plants:** Dimension electrolysis and methanation plants in the energy system model according to the scenarios.

6. **Model scenario sweeps:** Vary the energy carrier ratios, the energy source in district heating and the installed capacities of PtX components according to each scenario, then run dynamic simulations and integrate the results to analyse long-term storage.

6.7 Redistribution in this context means determining the number of appliances, like heat pumps or boilers, using each energy carrier so the appliances account for the share of energy demand by the energy carrier.

7. **Case studies:** Carry out a comparative analysis of long-term energy storage, dependence on transport networks (for gas and electricity) and demand coverage for each scenario on the basis of case studies of real de-central energy systems. The two de-central energy systems chosen for the case studies are the city of Karlsruhe with high PV potential and the city of Schmallenberg with high wind potential.

A schematic of the methodology used is shown in fig. 6.1 as a Sankey diagram. It shows the logic of splitting the annual heat and electricity demand by sector and energy carriers. The generation side of the energy system model can be varied by location, as it is parametrised according to the renewable energy potential of the region; the demand side and the PtX components in the energy system model can be varied according to the scenarios. Choosing a different scenario alters the energy carrier ratios, which in turn affects the real-time interaction between the components of the energy system. At each time step, if local power generation exceeds demand and all PtX components (e.g. electrolysers and methanation units) are already operating at full capacity, the surplus power is fed into the external high-voltage electricity transmission network.

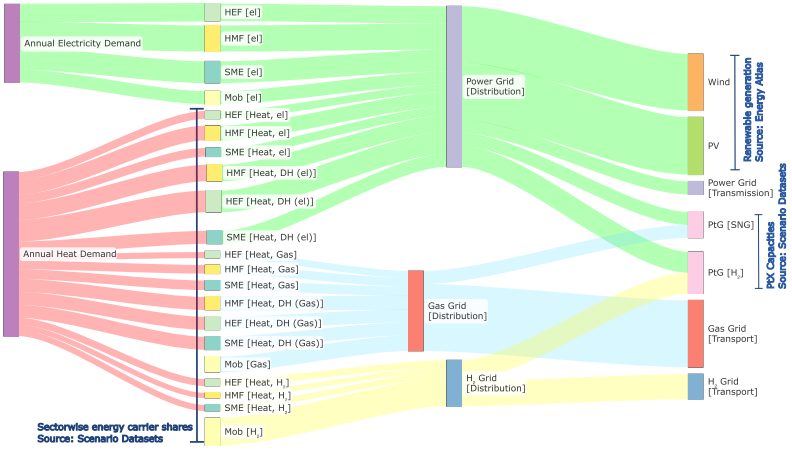

Figure 6.1: Sankey diagram showing the data sources used to configure the energy system model and the part of the energy system that is parametrised according to the scenarios.

If SNG or H_2 production exceeds demand, it must be exported to the corresponding[6.8] gas transport network. Conversely, if the demand cannot be met, power or gas is imported from the same external networks. Simulating this process year-round allows for the analysis of seasonal energy storage specific to the de-central energy system. The cumulative demand coverage for power and gas through local production after the year-long simulation is used to compare scenarios, with self-sufficiency acting as the benchmark.

6.8 A H_2 transport network is assumed to exist in all H_2-based scenarios.

However, to simulate different scenarios, the energy system model must be parameterised by adjusting the installed capacities of the generation components and the number of appliances using each energy carrier, as well as the capacities of the PtX plants, according to the specified scenario.

6.3 Parametrising the power generation components

Wind and PV plants are the two main renewable power generation components in the energy system model. The total installed capacity of the wind or solar plants in each region is set in the energy system model using data from the Energy Atlas [200, 201], where the potential of renewable power has been mapped across different geographical regions in Germany. The actual capacities for PV and wind plants used in the model are determined by scaling this renewable potential with a user-defined factor:

$$P_{\text{gen},r} = \omega_{\text{cu},r} \cdot P_{\text{total},r} \quad \forall r \in [\text{PV}, \text{Wind}], \tag{6.1}$$

where:

- r denotes the type of renewable energy source, specifically photovoltaic (PV) or wind.
- $P_{\text{gen},r}$ in kW represents the installed capacity for the renewable power source r specific to the region.
- $P_{\text{total},r}$ in kW is the total regional renewable potential for source r as provided by the energy atlas.
- $\omega_{\text{cu},r}$ is the user-defined capacity utilisation factor that determines the fraction of the total renewable potential that is used.

Once the plant capacities are established, they are used in the Modelica Buildings library [75, 87], to generate dynamic generation profiles. A conversion efficiency of 18 % is assumed for PV modules.

Assumptions:

- **Weather data accuracy:** The weather data used [142] is a reference year calculated using the TMY method [141]. The actual weather conditions in a given year may differ from this reference. The evolution of weather patterns due to climate change that might influence future renewable power generation is not considered. The weather data is assumed to be representative of the average conditions in the region.
- **Capacity Utilisation Factor ($\omega_{\text{cu},r}$):** It is assumed that the localised renewable potential for the region predicted in the energy atlas datasets is fully utilised ($\omega_{\text{cu},r} = 1$).

- **Downtime:** Plant maintenance downtimes are not considered, and all renewable plants are assumed to operate whenever renewable power is available.
- **Geographical limitations:** Regional variations such as terrain, shading and the effect of construction on the solar plants are not incorporated, and it is assumed that such effects are already taken into account while calculating renewable potential [200, 201].

6.4 Parametrising the demand-side components

The annual heat ($E_{\text{annual,heat}}$) and electricity ($E_{\text{annual,el}}$) demands in the region are distributed to each sector using the sectoral energy ratios $\omega_{\text{HEF}}, \omega_{\text{HMF}}, \omega_{\text{SME}}$ according to the following equations:

$$\vec{E}_{s,\text{annual,heat}} = E_{\text{annual,heat}} \cdot \vec{\omega}_s \quad \forall s \in \{\text{HEF, HMF, SME}\} \tag{6.2}$$

which can be expanded as:

$$\begin{bmatrix} E_{\text{annual,heat},HEF} \\ E_{\text{annual,heat},HMF} \\ E_{\text{annual,heat},SME} \end{bmatrix} = E_{\text{annual,heat}} \cdot \vec{\omega}_s \quad \text{where} \quad \vec{\omega}_s = \begin{bmatrix} \omega_{HEF} \\ \omega_{HMF} \\ \omega_{SME} \end{bmatrix} \tag{6.3}$$

Similarly, for electric load:

$$\vec{E}_{s,\text{annual,el}} = E_{\text{annual,el}} \cdot \vec{\omega}_{s(el)} \quad \forall s \in \{\text{HEF, HMF, SME, MOB}\} \tag{6.4}$$

which can be expanded as:

$$\begin{bmatrix} E_{\text{annual,el},HEF} \\ E_{\text{annual,el},HMF} \\ E_{\text{annual,el},SME} \\ E_{\text{annual,el},MOB} \end{bmatrix} = E_{\text{annual,el}} \cdot \vec{\omega}_{s(el)} \quad \text{where} \quad \vec{\omega}_{s(el)} = \begin{bmatrix} \omega_{HEF} \\ \omega_{HMF} \\ \omega_{SME} \\ \omega_{MOB} \end{bmatrix} \tag{6.5}$$

The three main sectors considered in the de-central energy system for heat demand are (i) Single-Family Homes (HEF) (ii) Multi-Family Homes (HMF) and (iii) Small and Medium-scale Enterprises (SME). The sectoral energy ratios $\vec{\omega}_s$ and $\vec{\omega}_{s(el)}$ are normalised shares that determine the fraction of the total annual energy demand allocated to each sector.

An important assumption is that the total annual energy demand is consumed exclusively by the sectors considered:

$$\omega_{\text{HEF}} + \omega_{\text{HMF}} + \omega_{\text{SME}} = 1. \tag{6.6}$$

for the annual heat demand and

$$\omega_{\text{HEF}} + \omega_{\text{HMF}} + \omega_{\text{SME}} + \omega_{\text{MOB}} = 1. \tag{6.7}$$

for the annual electricity demand. Sector-specific ratios $\omega_{\text{HEF}}, \omega_{\text{HMF}}, \omega_{\text{SME}}$ can be derived from local energy consumption data or from the number of buildings in each sector [202, 203]. $\vec{\omega_s}$ can be calculated for cities with detailed sector-wise energy consumption data as:

$$\omega_s = \frac{E_{\text{annual,heat},s}}{E_{\text{annual,heat}}} \quad \forall s \in \{\text{HEF}, \text{HMF}, \text{SME}\} \tag{6.8}$$

For cities lacking such data, $\vec{\omega_s}$ is estimated based on the number of buildings in each sector:

$$\omega_s = \frac{n_s}{n_{\text{total}}} \quad \forall s \in \{\text{HEF}, \text{HMF}, \text{SME}\} \tag{6.9}$$

where n_s is the number of buildings in each sector s which can be obtained from the census [203].

Redistribution according to energy carriers

The share of renewable energy carriers required in each sector to achieve sustainability is defined in the scenarios [195–199]. In order to analyse the impact of each scenario on the de-central energy system, the data from the scenarios must be quantified and normalised into energy carrier ratios. Subsequently, the annual heat demand for each city, previously split into sectors in eqs. 6.3 and 6.5, must be further split according to the energy carriers: Synthetic Natural Gas (SNG), H_2, Electricity (el) and district heating (DH) as:

$$\vec{E}_{s,ec,\text{annual,heat}} = E_{s,\text{annual,heat}} \cdot \vec{\omega_{ec}} \quad \forall s \in \{\text{HEF}, \text{HMF}, \text{SME}\}, \tag{6.10}$$

which can be expanded as:

$$\begin{bmatrix} E_{\text{heat-SNG},s} \\ E_{\text{heat-H2},s} \\ E_{\text{heat-el},s} \\ E_{\text{heat-DH},s} \end{bmatrix} = E_{\text{annual,heat},s} \cdot \begin{bmatrix} \omega_{\text{SNG}} \\ \omega_{\text{H}_2} \\ \omega_{\text{el}} \\ \omega_{\text{DH}} \end{bmatrix} \quad \forall s \in \{\text{HEF}, \text{HMF}, \text{SME}\} \tag{6.11}$$

Here too, it is assumed that the energy demand in each sector is fully covered by the energy carriers which means that the energy carrier ratios (including DH) will sum to 1:

$$\omega_{\mathrm{SNG}} + \omega_{\mathrm{H_2}} + \omega_{\mathrm{el}} + \omega_{\mathrm{DH}} = 1 \tag{6.12}$$

The normalised energy carrier ratios ω_{ec} for the three energy carriers (SNG, H_2, el) are calculated directly from the scenario datasets [195–199]. This in turn can be used in eq. 6.11 to redistribute the annual heat demand in each sector further in terms of energy carriers. Figure 6.2 illustrates the normalised energy carrier distributions across various sectors and scenarios. Each bar represents the share of energy carriers per sector in the scenario. The energy carrier ratios are used to adapt the energy system model to the scenarios by changing the number of appliances that use each energy carrier.

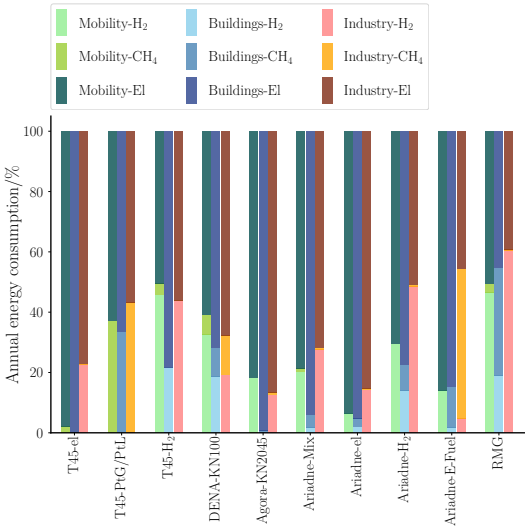

Figure 6.2: Annual energy demand in each sector (mobility, buildings, and industry) per energy carrier (CH_4, H_2, and renewable electricity) for each scenario

The heating system powering district heating is also changed according to the scenario[6.9]. If an all-electric scenario is chosen, the district heating is powered by large heat pumps, whereas in a gas-based scenario, CHPs are used to power district heating systems. On choosing the scenarios, the district heating components are replaced accordingly[6.10] in the energy system model.

6.9 Although district heating is not an energy carrier per se, in this work it is grouped along with other heating devices to have a perfect sector-wise split and an energy-carrier-wise redistribution.

6.10 In this context, the term "replacement" refers to the implementation of large electric heat pumps to power district heating systems in all-electric scenarios and using CHPs in gas-based scenarios for the same purpose.

The annual energy demand from district heating is calculated in eq. 6.14 using ω_{DH} and the annual heat demand in each sector. The capacity of the district heating plant is calculated [6.11] as:

$$P_{\mathrm{DH}} = \frac{E_{\mathrm{DH}}}{\mathrm{FLH}} \tag{6.13}$$

where FLH is the full-load hours and:

$$E_{\mathrm{DH}} = \omega_{\mathrm{DH}} \cdot E_{\mathrm{annual,heat}} \tag{6.14}$$

Scenario interchangeability

The vector $\vec{\omega}_{ec}$ calculated directly from the scenario datasets [195–199] is normalised such that:

$$\omega_{\mathrm{SNG}} + \omega_{\mathrm{H_2}} + \omega_{\mathrm{el}} + \omega_{\mathrm{DH}} = 1 \tag{6.15}$$

Normalising the energy carrier ratios ensures that using a new scenario reassigns the shares of hydrogen, natural gas and electricity in each sector without affecting the annual energy demand. Changing the scenario does not change heat demand or the distribution of heat demand. Instead, the same demand is met using a different set of energy carriers.

Assumptions

1. **Exclusivity:** Both $\vec{\omega}_{s}$ and $\vec{\omega}_{ec}$ are assumed to be exclusive which means that the annual energy demand is fully covered by the sectors HEF, HMF and SME and within each sector the demand is fully covered by H_2, SNG, DH and electricity. Fossil-based energy carriers are not used.
2. **No internal variations within each type:** All the buildings inside each BDEW classification can still have different types of insulation or ages which can affect the demand. Such variations are not considered and all the buildings inside one type are assumed to have uniform behaviour.
3. **Technical feasibility:** In all the sectors, it is assumed that the technologies for using the energy carriers like heat pumps, H_2 and SNG boilers are already operational.
4. **Network availability:** It is assumed that distribution networks for both H_2 and SNG are available in the de-central system to simulate those scenarios where there is demand for both H_2 and SNG.
5. **Technologies powering district heating:** In all the scenarios, the technologies powering district heating are assumed to be uniform.

[6.11] A detailed sample calculation for the splitting of annual heat demand according to the sectors and further redistribution according to energy scenarios and setting the district heating system is provided in section A.5.

In all-electric scenarios, the entire district heating system is powered by electric heat pumps while in gas-based scenarios, CHP systems are used. In mixed scenarios where both electrification and gas-based energy carriers are given importance, the district heating system is powered only by CHPs (a mix of heat pumps and CHPs is not considered).

6.5 Dynamic profiles

All energy demands (including annual heat/electricity and their redistribution by sector and energy carrier) require time-dependent load curves to be used as dynamic boundary conditions in the energy system model. This means that the annual energy demands must be converted into time-series data for load profiles:

$$\vec{E}_{s,ec,\text{annual,heat}} = \vec{n}_{ec} \cdot \int P(t)\,dt \tag{6.16}$$

where

$$\vec{n}_{ec} = \vec{\omega}_{ec} \cdot n_s \tag{6.17}$$

and

$$\vec{n}_s = \vec{\omega}_s \cdot n_{total}. \tag{6.18}$$

In Equation 6.16, $\int P_i\,dt$ represents the integral of the standard load profiles (e.g. based on BDEW guidelines) over the chosen time horizon. Here, $\vec{\omega}_s$ denotes the sector-wise energy ratios, $\vec{\omega}_{ec}$ denotes the energy carrier share within that sector, and n_{total} is the total number of buildings. The resulting dynamic profiles capture the daily and seasonal fluctuations of building heat demand, mapped to each carrier as specified by the scenario assumptions. To create the load profiles for the residential and SME sectors, the BDEW guidelines [169] are used. The procedure is summarised as follows:

1. **Start with carrier-specific annual demand in each sector:** Use the annual energy demand (heat or electricity) per carrier in each sector from eq. 6.11.
2. **Apply temperature-based factors:** Incorporate BDEW reference temperature profiles to capture the effect of weather on heat demand, along with day-type adjustments (weekdays, weekends, holidays).
3. **Interpolate to required time-step:** The resulting standard load profiles are then interpolated to match the simulation time-step (e.g. 15 minutes or hourly).

For mobility, a specified number of EVs, denoted by N_{EV}, is allocated from the census data. Each EV is then assigned a charging load profile [170].

The total charging demand in the region, denoted by $P_{\text{mobility}}(t)$, is formulated as

$$P_{\text{mobility}}(t) = N_{\text{EV}} \times P_{\text{EV}}(t). \tag{6.19}$$

where $P_{\text{EV}}(t)$ is the time-dependent charging profile of a single EV and N_{EV} is the number of EVs in the region. Gas and hydrogen vehicles are not allocated separately, because their fuel usage is assumed to be accounted for (as fuel stations) in the SME sector.

Consistency check

On integrating the load profiles over one year, the annual demand should be equal to the annual demand from which the profiles are made. As sigmoid functions are used in the load profiles and interpolation is used to increase profile resolution, numerical errors are possible. It must be verified whether such errors are beyond acceptable limits. To confirm that the dynamic load profiles reflect the cumulative annual demand specified by each scenario, the generated profiles are reintegrated:

$$\vec{n}_{ec} \cdot \int_0^T P(t)\,dt \approx \vec{E}_{s,ec,\text{annual,heat}} \tag{6.20}$$

where T is one year. The relative error is computed as:

$$\text{error}_{s,ec} = \left| \frac{\vec{n}_{ec} \cdot \int_0^T P(t)\,dt - \vec{E}_{s,ec,\text{annual,heat}}}{\vec{E}_{s,ec,\text{annual,heat}}} \right| \times 100\%. \tag{6.21}$$

A manual check is also carried out on each load profile. This is to ensure that the daily and seasonal patterns are realistic. In all the simulations in this work, the error never exceeded 5 %.

6.6 Dimensioning the PtX units

Although the scenarios do not provide explicit ratios for setting capacities of individual plants, each scenario provides the share of renewable gases (H_2 or SNG) in the annual energy demand (Figure 6.3). The shares of renewable gases are used to calculate the capacities of electrolysis and methanation units. The electrolyser capacity P_{ely} and the methanation capacity P_{met} can be determined from:

$$P_{\text{ely}} = \omega_{H_2} \cdot P_{\text{gen},r} \quad \forall r \in [\text{PV}, \text{Wind}] \tag{6.22}$$

$$P_{\text{met}} = \omega_{\text{SNG}} \cdot P_{\text{gen},r} \quad \forall r \in [\text{PV}, \text{Wind}] \tag{6.23}$$

where $P_{\text{gen,r}}$ is the total generation capacity determined from eq. 6.1 by scaling the regional wind and PV potentials with the capacity utilisation factor $\omega_{\text{cu},r}$. ω_{H_2} and ω_{SNG} are the normalised shares for H_2 and SNG in the energy mix derived from the scenario[6.12] datasets (Figure 6.3).

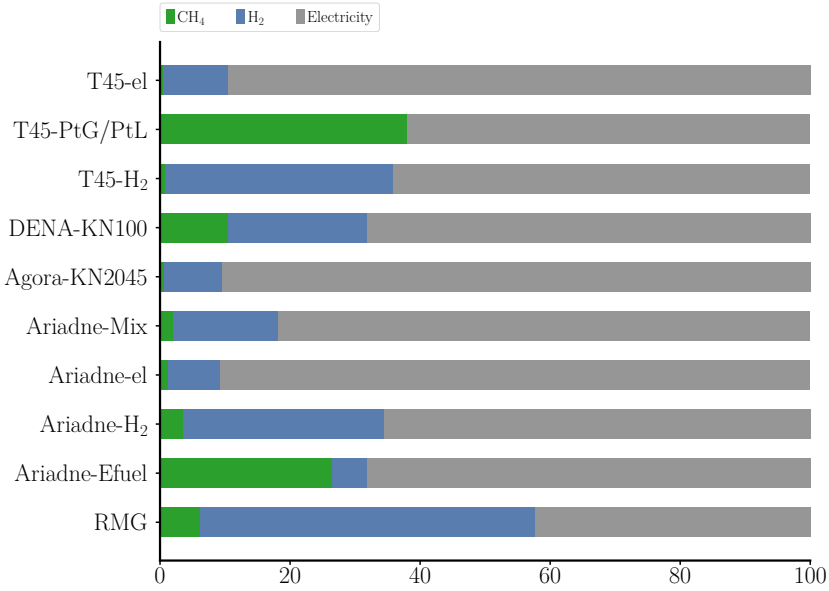

Figure 6.3: Share of energy carriers in annual energy demand for each scenario

6.7 Scenario sweep

The final simulation step is a scenario sweep, i.e. all resulting energy systems parametrised according to the scenarios are simulated. In the initialisation phase (steps 1–8 in fig. 6.4) the generation side, demand side, district heating (DH) allocation, mobility, load profiles and storage components are all configured in the energy system model. All dynamic load profiles are then generated according to the required time step.[6.13]

6.12 Using the shares of renewable gases from the scenario dataset to calculate the electrolysis and methanation capacities is not an accurate method as the scenarios are trends designed for the whole country and not customised for each region. This causes the possibility that the PtX units are either under-dimensioned or over-dimensioned in the region. Therefore, an additional parameter sensitivity study is required to fine-tune the storage capacities specific to the location of the de-central energy system. This is the focus of chapter 7.

6.13 If lower time steps are required, the standard load profiles are interpolated to the required time step.

Once this initialisation is complete, multiple Functional Mock-up Units (FMUs) [190] are created, one for each scenario considered. The generated FMUs are then simulated in parallel[6.14]. Each scenario is simulated for a full year to capture short-term (daily), medium-term (monthly) and long-term (seasonal) interactions. The results are then used for a comparative analysis of fuel mixes, storage strategies, district heating decisions and mobility issues, highlighting trade-offs between electrification, gas-centric approaches or hybrid solutions.

Each scenario is further examined for local self-sufficiency by determining how much renewable power must be imported from the electricity transmission grid or renewable gases from the gas transport network on a real-time basis. A scenario is deemed to offer the region higher self-sufficiency if energy exchanges with external transport networks are minimised, indicating that the region is able to meet most of its own demand locally. A summary of the process schematic leading to the scenario sweep is shown in fig. 6.4. A detailed sample calculation for the sector and energy carrier allocation procedure is provided in section A.5.

6.14 After testing several Python libraries, the Ray [204] library was found to be suitable for parallelising the large simulation model with $\sim 10^4$ to $\sim 10^5$ equations per energy system across multiple scenarios and different cities.

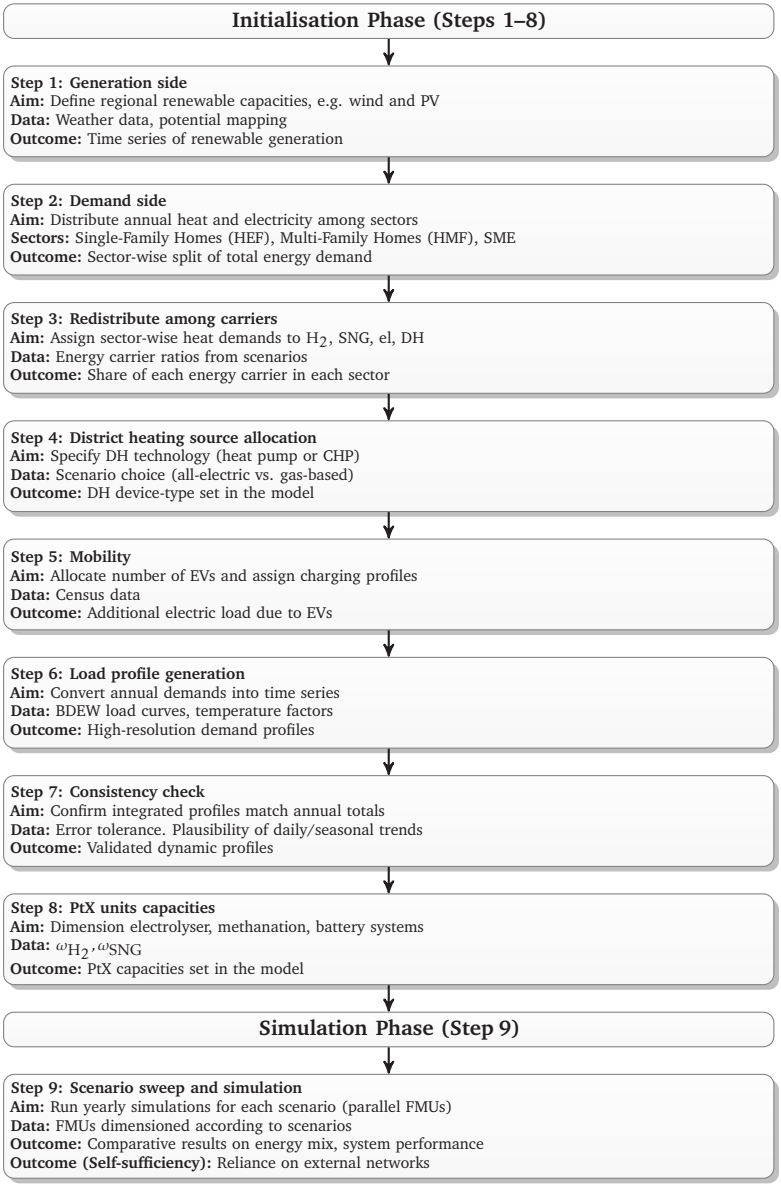

Figure 6.4: Overview of scenario analysis methodology with the initialisation phase (Steps 1–8) and the simulation phase (Step 9).

6.8 Case study: Karlsruhe and Schmallenberg

Two contrasting German cities were chosen to illustrate how the scenario-driven allocations and dynamic simulations affect a de-central energy system in practice. Karlsruhe, with its high solar potential, is a model for future energy systems with high PV-based generation, while Schmallenberg has a very high wind potential. Both cities are initialised with renewable potential data, after which the demand side is initialised, dynamic profiles are generated (see section 6.5) and the methanation and electrolysis units are dimensioned (for scenarios where they are relevant).

Data acquisition

In Karlsruhe, sector-specific energy demand data is available (table 6.3), while for Schmallenberg, the data had to be derived from the census [203]. Across both cities, the key question remains how different energy carrier mixes and related storage capacities perform in meeting local demand without excessive reliance on external grids or networks. Therefore, the models are initialised and simulated (according to the method summarised in fig. 6.4) for each scenario.

Table 6.2: City configuration: Potentials and demand. Data sources: For Karlsruhe: Energie Atlas BW [200] and Energie Leitplan Karlsruhe [202]. For Schmallenberg: Energie Atlas NRW [201]

	Karlsruhe	Schmallenberg
Total solar potential P_{solar} (GW)	1.1	0.022
Total wind potential P_{wind} (GW)	0.00044	0.487
Yearly electrical demand E_{eldem} (TWh)	1.25	0.105
Yearly thermal demand E_{thdem} (TWh)	3.0	0.0648

Table 6.3: Sector ratios in city configuration. Data sources: For Karlsruhe: Energie Leitplan Karlsruhe [202]. For Schmallenberg: Derived from Census [203]

City	Karlsruhe	Schmallenberg
ω_{SME}	0.138	0.143
ω_{DH}	0.100	0.022
ω_{HMF}	0.280	0.135
ω_{HEF}	0.482	0.700

The dynamic results are then evaluated for each city and scenario. The energy system model corresponding to each scenario is exported as a functional mock-up unit (FMU) [190] and all the FMUs are simulated in parallel using the Python Ray library [204]. The results are then compared to evaluate the performance of each scenario in meeting local energy demands, storage utilisation, and grid interactions.

6.9 Results: Comparative evaluation

The energy systems corresponding to each energy scenario are dynamically simulated. This analysis targets key metrics to evaluate the de-central energy systems:

- **Storage utilisation**: Identifies periods with heavy reliance on gas-based or battery buffering.
- **Grid and network interaction**: Explores the extent of external grid imports or curtailment of surplus power.
- **Scenario-based system efficiencies**: Compares total delivered energy services (heat, electricity, or fuels) to total inputs, highlighting reliance on external grids or networks, dependence on seasonal gas storage, or both.

Taken together, these indicators offer a holistic view of how each scenario configuration aligns with local constraints and overarching sustainability goals. The simulation results are evaluated in three progressive stages. In the first stage, the dynamics of the system are evaluated in the short term. The results are plotted over a period of one month to evaluate the changes in the summer and winter months.

Finally, the monthly results are integrated and evaluated over a period of one year to determine the seasonal trends. It is important to define the terms “power surplus” and “power deficit”[6.15]. The power surplus is defined as follows (eq. 6.24):

$$P = \begin{cases} P_{\text{surplus}}, & \text{if } \left(P_{\text{wind}} + P_{\text{PV}} + P_{\text{CHP,el}}\right) > \left(P_{\text{load,el}} + P_{\text{ely}} + P_{\text{met}}\right) \\ P_{\text{deficit}}, & \text{if } \left(P_{\text{wind}} + P_{\text{PV}} + P_{\text{CHP,el}}\right) < \left(P_{\text{load,el}} + P_{\text{ely}} + P_{\text{met}}\right) \end{cases} \tag{6.24}$$

The power generated in each scenario is normalised according to the equation:

$$P_{\text{norm}} = \begin{cases} \dfrac{P(t)}{\max[P(t)]} \cdot 100 & \text{Generation} \\ \dfrac{-P(t)}{\max[P(t)]} \cdot 100 & \text{Loads} \end{cases} \tag{6.25}$$

where max[P(t)] is the maximum power generation or load in the given time period. In all short-term simulations, the installed capacities of wind and PV plants (Table 6.2) are assumed to be equal to the maximum potential. This is to ensure that enough surplus power is available to analyse the dynamic response of various components in the energy system.

6.15 The term *power surplus* (P_{surplus}) denotes the excess renewable power generated locally after meeting the local electrical load and fully utilising electrolysers and methanation units. The term *feed-in* ($P_{\text{feed-in}}$) refers to the surplus power exported to the external electricity transmission grid when it cannot be utilised or stored locally. The term *grid import* (P_{deficit}) refers to power drawn from the external electricity transmission grid. The term *curtailment* (P_{curtail}) refers to the deliberate reduction of surplus power generation when feed-in is not possible.

For ease of understanding, scenarios with high electrification and no electrolyser capacity are referred to as "all-electric scenarios" and those with high H_2 or SNG production are referred to as "gas-based scenarios". Figure 6.5 illustrates the short-term fluctuations in power generation and load in Karlsruhe, a region with high solar potential. When simulated under an all-electric scenario, it can be seen that there is a marked increase in solar power generation during the mid-day period. A portion of the renewable power surplus (labelled Surplus (el) in Figure 6.5) cannot be utilised or stored locally and must be fed into the external electricity transmission grid or curtailed. Similar trends are observed in energy systems with high wind potential when all-electric scenarios are implemented (Figure 6.6). Here, the duration of the power surplus is longer than that of energy systems in regions with high solar potential. When the same cities are simulated under a gas-based scenario, it can be seen that the surplus power is significantly lower. This is because in gas-based scenarios, H_2 or SNG production increases during periods of surplus power generation, utilising more of the excess power (Figure 6.7).

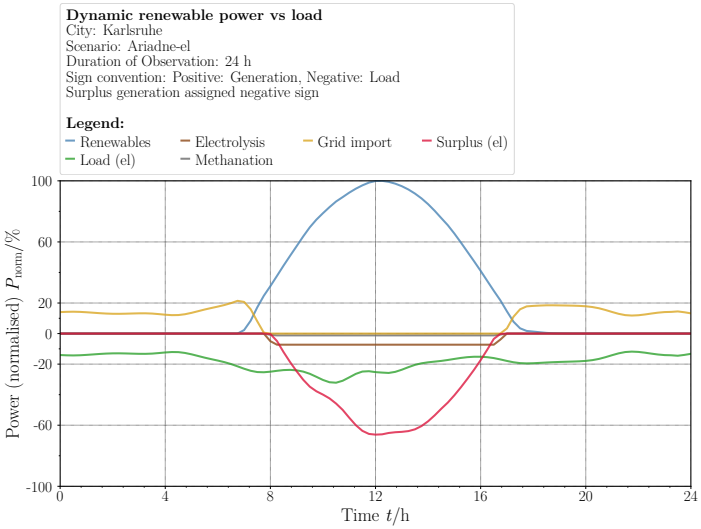

Figure 6.5: Short-term variations in regions with high solar potential simulated under an all-electric scenario. Y-axis values normalised according to eq. 6.25.

The utilisation of excess power to produce renewable gases results in the net surplus being lower compared to all-electric scenarios. However, an anomaly is observed where, even when electrolysers operate at full capacity, some surplus power remains and is fed into the external electricity transmission grid or curtailed in gas-based scenarios. The presence of additional surplus power even in gas-based scenarios highlights a limitation of the scenario-based method. The energy carrier ratios (Figure 6.3) in the scenarios are calculated for the national level. PtX plant capacities (electrolysers or methanation units depending on the scenario) are dimensioned using these ratios.

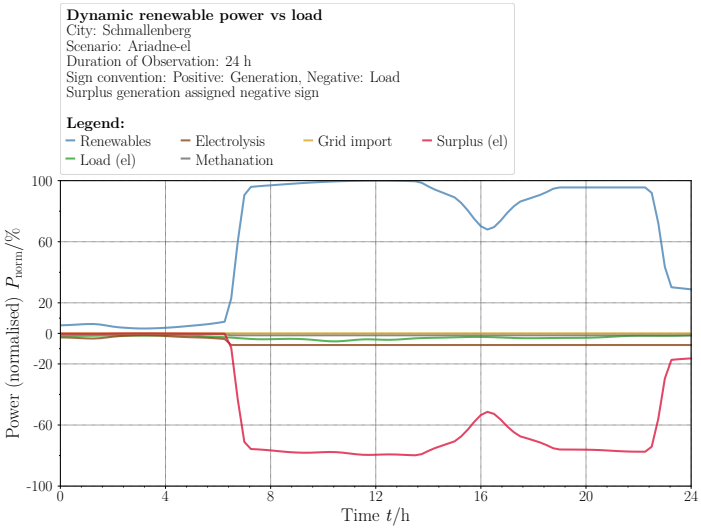

Figure 6.6: Short-term variations in regions with high wind potential simulated under an all-electric scenario. Y-axis values normalised according to eq. 6.25.

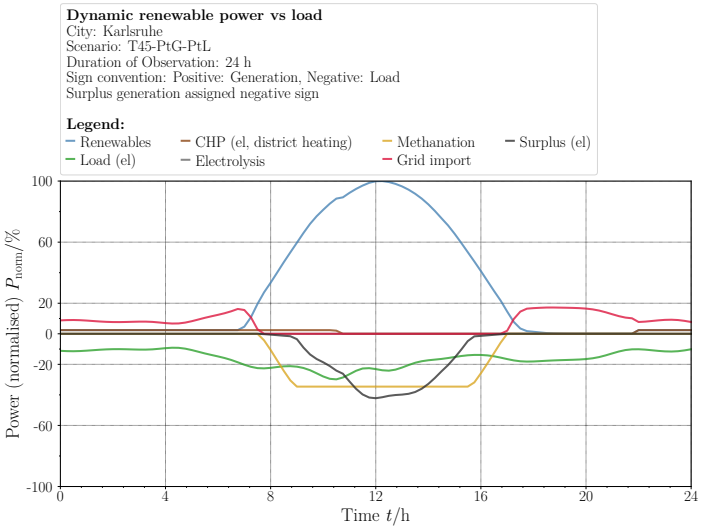

Figure 6.7: Short-term variations in regions with high solar potential simulated under a gas-based scenario. Y-axis values normalised according to eq. 6.25.

However, the use of these ratios in the as-is condition may result in storage units being under- or over-dimensioned (Figure 6.7). If the storage units are under-dimensioned, a portion of the surplus power cannot be utilised or stored locally and is fed into the external electricity transmission grid or curtailed (Figure 6.7). Therefore, the PtX unit capacity must be first set using the energy carrier ratios specified in the scenarios and additionally fine-tuned[6.16] for each region (see the parameter sensitivity analysis in Chapter 7).

6.10 Monthly variations

After the short-term dynamic results, the simulation results are analysed over a period of one month. This period allows for the observation of dynamic patterns during the winter or summer months. The response of different components of the de-central energy system during these months is vital to evaluate the efficacy of each scenario. The dynamic response of the de-central energy system during a typical winter or summer month also changes depending on whether the region has a high solar or wind potential. Therefore, the scenario comparison is repeated for both cities. In the monthly results, the energy systems are simulated using three different scenarios for two cities (The scenarios are: (i): the all-electric scenario Ariadne-el, (ii): the gas-based scenario Road Map Gas (RMG) and (iii): the mixed scenario DENA-KN100).

The results are then normalised using the monthly maximum across all the evaluated scenarios according to the equation:

$$P_{\text{norm}} = \frac{P(t)}{\max_i[\max_j[P(t)]]} \tag{6.26}$$

where i is the number of scenarios and j is the number of result points in each month for each scenario.

The dynamic response of the de-central energy system with a high solar potential in a typical summer month is depicted in Figure 6.8. It can be seen that when simulated under the all-electric scenario, the energy system consistently produces higher surplus power that cannot be utilised or stored locally, leading to increased feed-in to the external electricity transmission grid or curtailment, compared to gas-based scenarios. For the region with high wind potential, the same effect can be observed, with the difference that the individual duration of the periods (Figure 6.9) of surplus generation is higher than in the case of cities with a high share of PV.

The months of surplus generation are different in energy systems with high PV and wind potentials. In both cases (Figure 6.8 and Figure 6.9) the implementation of all-electric scenarios leads to an increased power surplus. This not only increases the likelihood of curtailment or feed-in to the external electricity transmission grid, but also represents a missed opportunity to produce renewable gas throughout the month.

6.16 Fine-tuning in this case means increasing or decreasing the capacities of the PtX units to ensure that 100 % of the power surplus is utilised.

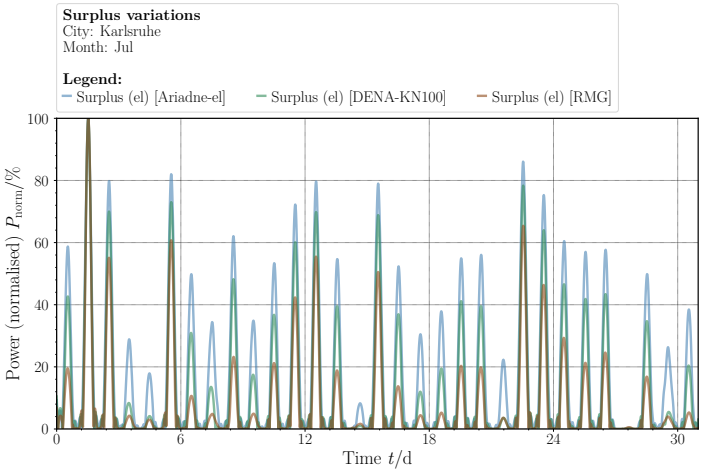

Figure 6.8: Dynamic variation of power surplus in a city with high solar potential (Y-axis values normalised according to eq. 6.26).

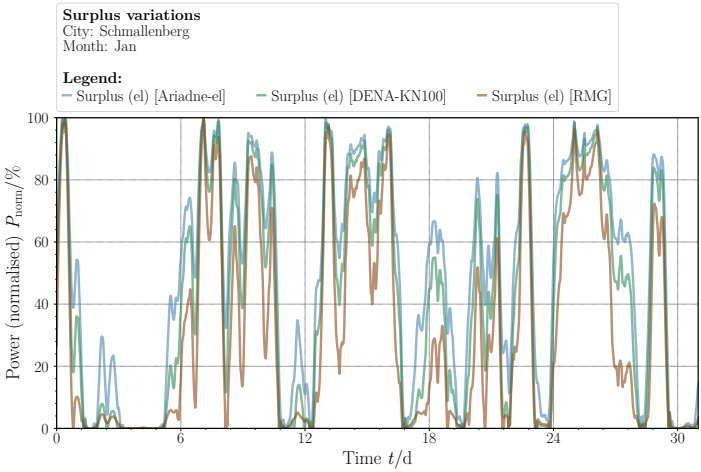

Figure 6.9: Dynamic variation of power surplus in a city with high wind potential (Y-axis values normalised according to eq. 6.26).

The energy system also needs to rely on grid imports if there is a deficit in power generation. The electrical load is already higher in winter than in summer. This, combined with the reduced COP of heat pumps in winter, the simultaneous operation of several heat pumps, and the lack of alternative gas heaters in all-electric scenarios, further increases the electrical load. As a result, the dependence on grid imports is higher when the energy system is simulated under all-electric scenarios (Figure 6.10).

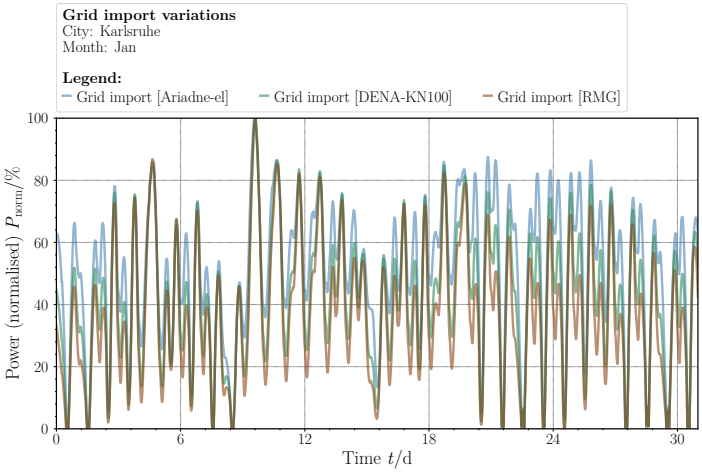

Figure 6.10: Dynamic variation of power imported from the grid during winter in a city with a high share of PV (Y-axis values normalised according to eq. 6.26).

It is of particular concern that the duration of the power deficit in wind-dependent energy systems can last longer. This implies that during periods of deficit, the back-up supply necessary to compensate for the shortfall will have to operate for longer periods to prevent black-outs. Unlike gas-based scenarios, a power black-out in all-electric scenarios will also result in a heat black-out, which provides further justification for the use of a molecule-based sector-coupling strategy.

6.11 Feasibility of seasonal energy storage

One of the main advantages of using gas-based scenarios for sector coupling is the possibility of long-term[6.17] energy storage. Long-term energy storage requires a continuous period of high generation followed by periods of high deficit so that renewable gases can be produced during the season with surplus power to supply the deficit season.

6.17 In this work, the duration of "long-term" in long-term energy storage is assumed to be in the order of months. Therefore, the terms long-term storage and seasonal storage are used interchangeably.

To analyse long-term energy storage, the dynamic results for each month need to be integrated and plotted for the whole year using weather data specific to the location of the energy system. Energy systems with a high share of PV plants have a clear summer-winter divide. This pattern is characterised by high renewable power generation in the summer months, when surplus power is high and heat demand is low. Energy systems with a high share of wind plants, on the other hand, do not have a consistent seasonal pattern for renewable power generation. Although long-term storage is still possible, the seasonal pattern of wind power generation is highly site specific. However, the winter heat demand is independent of the renewable power generation type and is high for both systems. To analyse sector coupling combined with long-term energy storage, the renewable power generation, gas production, and loads from the dynamic simulation results are integrated for each month. The process is repeated for each scenario and each chosen region. Each point in the scatter plots analysing the feasibility of long-term storage is normalised using the highest monthly integral in a year according to the equation:

$$E_{\text{norm}} = \frac{\left[\int_{t_0}^{t_{\text{end}}} P(t)\,dt\right]_i}{\max\left[\max\left[\int_{t_0}^{t_{\text{end}}} P(t)\,dt\right]_i\right]} \cdot 100, \text{ where, } i = 1, 2, 3...12 \tag{6.27}$$

The integrated monthly results[6.18] are used to assess whether H_2 or SNG generation during the surplus season combined with long-term storage can mitigate the deficit in the lean season. Implementing the all-electric scenario results in higher surplus power throughout the surplus season, which is fed into the external electricity transmission grid or curtailed (Figure 6.11). This represents a missed opportunity to produce renewable gases using the surplus power and as a result also reduces the possibility for long-term energy storage (Figures 6.15 and 6.16) in de-central energy systems when the all-electric scenario is implemented. In cities with high wind potential, the annual generation of wind power is more erratic (Figure 6.12). Surplus power generation is feasible during several periods throughout the year. However, it can be seen that the implementation of all-electric scenarios leads to significantly higher un-utilised surplus power compared to gas-based scenarios. During the winter months, both cities show an increase in electricity demand (Figures 6.13 and 6.14).

Solar power generation is lower in winter than in summer. Therefore, in regions with high solar potential, the combination of high power demand and reduced power generation leads to increased dependence on grid imports (Figure 6.13). When analysing the power deficit, the difference between the scenarios is not very noticeable for the city with high wind potential (Figure 6.14), due to the longer duration of wind power generation in winter (Figure 6.9) compared to the city with high solar potential. However, the result cannot be generalised as wind patterns are different in each city. Reducing dependence on grid imports is not enough to achieve overall energy system self-sufficiency. The energy systems must also be independent in terms of renewable gas production.

6.18 To avoid redundancy, not all scenarios are plotted. Only one all-electric, mixed and gas-based scenario is selected for illustrative purposes. The results comprising all the scenarios are provided in the Appendix.

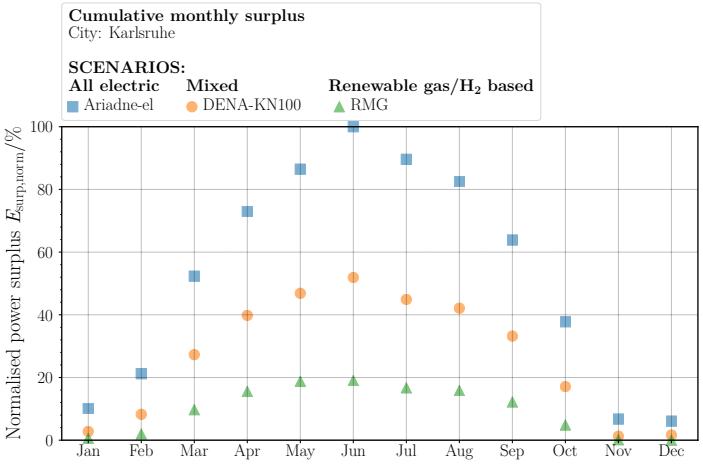

Figure 6.11: Monthly integrated surplus power variations in a sunny region. All-electric scenario has significantly higher surplus power in summer. Y-axis values normalised according to eq. 6.27. For all the scenarios, see fig. A.1.

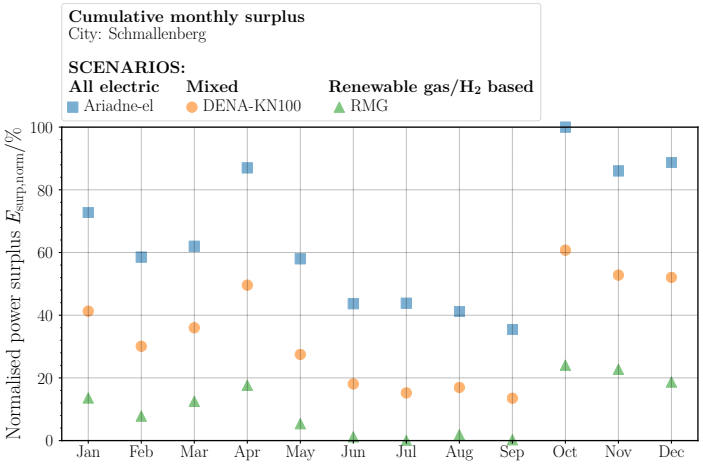

Figure 6.12: Monthly integrated surplus power variations in a windy region. Y-axis values normalised according to eq. 6.27. For all the scenarios, see fig. A.3.

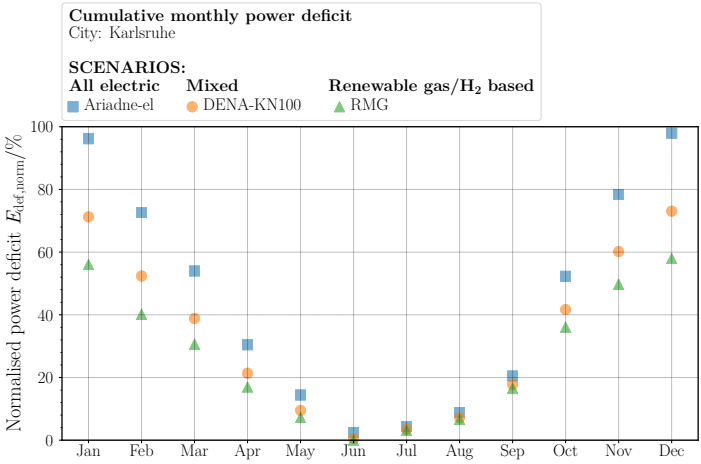

Figure 6.13: Monthly integrated grid import variations in a sunny region. Y-axis values normalised according to eq. 6.27. For all the scenarios, see fig. A.2.

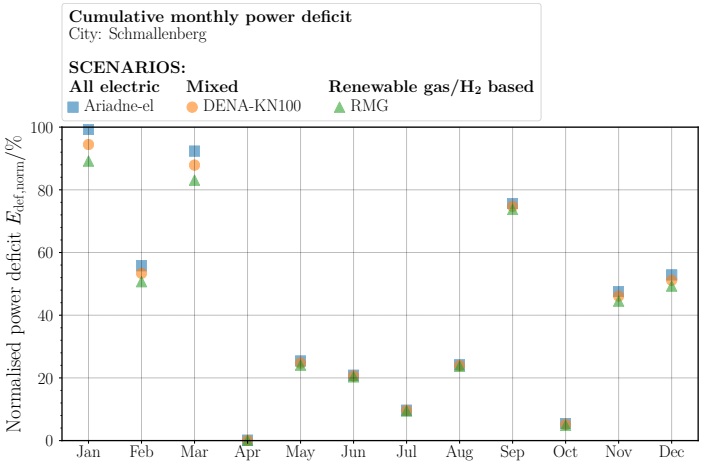

Figure 6.14: Monthly integrated grid import variations in a windy region. Y-axis values normalised according to eq. 6.27. For all the scenarios, see fig. A.4.

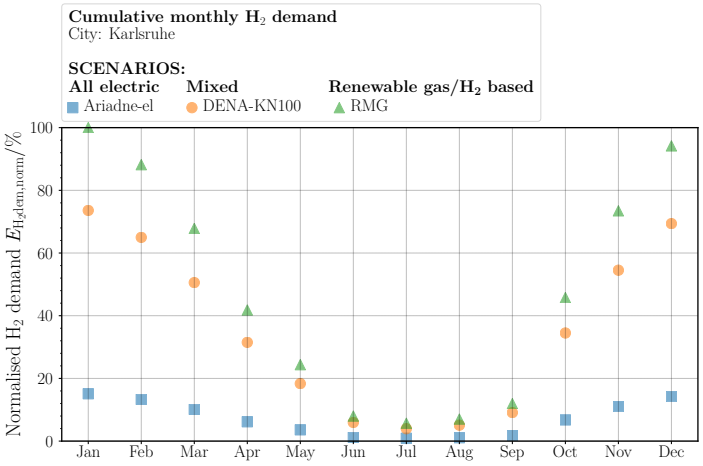

Figure 6.15: Renewable H_2 demand. Y-axis values normalised according to eq. 6.27. For all the scenarios, see fig. A.6.

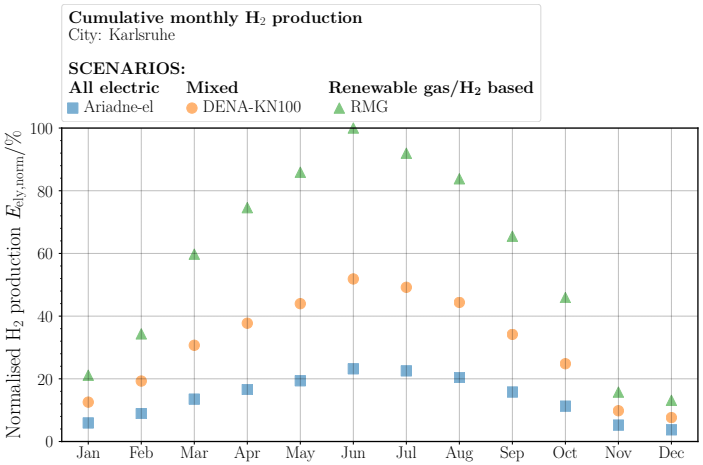

Figure 6.16: Renewable H_2 production. Y-axis values normalised according to eq. 6.27. For all the scenarios, see fig. A.6.

It can be seen on evaluating long-term storage in relation to seasonal gas demand and renewable gas production, that cities with high solar and wind potential have high gas demand in winter. But in cities with high solar potential, winter demand can be met with renewable gas produced in summer, when the demand for gas is much lower (Figure 6.16). It can be summarised from the scenario analysis that higher seasonal storage, reduced curtailment and feed-in, and reduced winter grid imports are advantages of gas-based scenarios. It is also evident from the results that the advantages must be quantified specific to the de-central energy system using location-specific boundary conditions. Long-term storage can be concluded to be the critical capability that a de-central energy system will lack if an all-electric scenario is implemented.

Additional research is necessary to evaluate the infrastructure modifications and associated expenses required to adapt the grids and networks and implement all-electric or gas-based scenarios. In addition, cities that lack high wind and solar potential and may need to import gases should also be evaluated. The existing portfolio of scenarios is also highly likely to change over time. However, the important takeaway from the scenario analysis is that integrating a molecule-based approach with a long-term storage strategy greatly enhances both the security of supply and the reliability of a de-central energy system. But the benefits must be quantified for each de-central energy system seperately.

7 Parameter sensitivity analysis

The effect of changing energy carriers in sector coupling can be analysed by simulating de-central energy systems under different scenarios. However, energy scenarios are developed at a national level and only show general trends. Therefore, the dimensions of the components, in particular the PtX components such as methanation or electrolysis units, may be either excessive or insufficient for a particular location if they are dimensioned using only the ratios from the scenarios. It is therefore essential to carry out a further parameter sensitivity analysis, focusing on the installed capacities of site-specific components. This chapter introduces a Design of Experiment (DOE) approach using sampling techniques to generate a range of random values for each independent variable, and then simulating the energy system over these variables to assess parameter sensitivity.

Sampling is performed by dimensioning all the energy system components using the ratios from the scenario datasets and energy atlas as a baseline and varying selected independent variables, such as installed wind and PV capacities or electrolyser and methanation capacities, between minimum and maximum deviations from the baseline. The installed capacity of renewables and the capacity of PtX units are chosen as independent variables because they have the greatest impact on self-sufficiency as seen in the scenario studies. The power surplus, annual power deficit, and the ratio of renewable gas production to demand are identified as key output parameters, as they can be used to assess the security of supply and self-sufficiency of the de-central energy system. The parameter sensitivity analysis is carried out to analyse the impact of three highly plausible activities in present energy systems, i.e., scaling up renewable capacity alone, scaling up PtX capacities alone, or scaling up both.

7.1 Parameter sensitivity

To assess parameter sensitivity, a Design of Experiments (DOE) approach is used where each independent variable is assigned a maximum and minimum range within which random values are generated. Advanced sampling methods, such as Plackett-Burman [205] or Latin Hypercube Sampling (LHS) [206], prevent sample clustering and ensure comprehensive coverage between set limits. The de-central energy system is then configured for each set of input parameters, and the output parameters are derived from simulation results. Identifying relevant input and output variables for sensitivity analysis is challenging due to the multitude of results produced by simulations.

In this study, the output parameters are selected to evaluate the supply security and self-sufficiency of the energy system. The International Energy Agency (IEA) defines energy supply security based on three aspects:

1. Adequacy: The demand must be met at all times under normal operating conditions.
2. Security: Un-interrupted energy supply under flexible operating conditions and ramping rates.
3. Resilience: Ability of the system or components to recover from short- or long-term disruptions.

If energy systems do not meet supply security objectives, sporadic or cascading blackouts could occur [207]. Although some studies focus solely on adequacy to evaluate supply security [208–210], Zeng et al. [211] argue that adequacy also depends on demand response and consumer behaviour. Other research [57, 58, 60] uses resilience to assess supply security. Senkel et al. [59] uses a performance measure (MOP) to quantify resilience in integrated energy systems. The parameter sensitivity analysis in this work uses annual power deficit and power surplus to evaluate scale-up. The underlying dynamic model, from which the cumulative annual values are generated, accounts for other features such as ramping rates and connections to the external transport networks. Integrating the time-resolved simulations that balance supply and demand (in gas, electricity, and heat) at every time step gives the annual power surplus and annual power deficit.

7.2 Selection of output parameters

The output parameters are used to assess the security of supply and the self sufficiency of the energy system. The parameters used to identify supply security are the annual cumulative grid feed-in (feeding into the power transmission grid due to power surplus) and grid import (drawing power from the power transmission grid during cumulative annual power deficits), calculated as:

$$E_{\text{surp}} = \int_0^{t_{\text{end}}} P_{\text{surp}} \cdot dt \tag{7.1}$$

$$E_{\text{def}} = \int_0^{t_{\text{end}}} P_{\text{def}} \cdot dt \tag{7.2}$$

where P_{surp} is the surplus power remaining after all storage options have been exhausted and P_{def} is the power deficit. The annual integrals[7.1] are normalised for scenarios, $i = 1, \ldots, n$, as:

7.1 Multi-time scale dynamic behaviour and co-simulation with spatial network tools are part of the energy system model. The parameter sensitivity analysis focuses only on the integrated results of this model. Furthermore, the concept of "grid" used in the parameter sensitivity analysis is monolithic, meaning that whenever there is a shortage of supply of any form of energy (heat, gas, or electricity), the grid will cover the shortfall. The cumulative annual values can be used to assess self-sufficiency.

$$E_{\text{surp,norm}} = \frac{E_{\text{surp}}(i)}{\max\left[E_{\text{surp}}(i)\right]} \cdot 100, \quad E_{\text{def,norm}} = \frac{E_{\text{def}}(i)}{\max\left[E_{\text{def}}(i)\right]} \cdot 100 \tag{7.3}$$

The other output parameter is the ratio of renewable SNG or H_2 produced annually within the region to the demand for the renewable gases in the region. This parameter determines whether the region is self-sufficient in terms of gas production. The ratio of the annual gas production to the annual gas demand is calculated as:

$$\omega_{\text{H}_2} = \frac{E_{\text{H}_2,\text{gen}}}{E_{\text{H}_2,\text{dem}}}, \quad \omega_{SNG} = \frac{E_{\text{SNG,gen}}}{E_{\text{SNG,dem}}}. \tag{7.4}$$

where

$$E_{\text{H}_2,\text{gen}} = \int_0^{t\max} P_{\text{ely}}\, dt \quad \text{and} \quad E_{\text{SNG,gen}} = \int_0^{t\max} P_{\text{met}}\, dt \tag{7.5}$$

In eq. 7.5, annual demands $E_{\text{H}_2,\text{dem}}$ and $E_{\text{SNG,dem}}$ are calculated from the scenario and city datasets (Section 6.3) and the local production of renewable gases $E_{\text{H}_2,\text{gen}}$ and $E_{\text{SNG,gen}}$ are obtained by integrating the results of the dynamic simulation. A ratio above 1 indicates that annual production exceeds demand over the whole time duration (1 year in this case).

7.3 Assumptions

The parameter sensitivity study in this work is carried out under the following assumptions (Table 7.1) for Karlsruhe and Schmallenberg. The median values for solar and wind power capacities are assumed from the energy atlas datasets [200, 201]. The median values of electrolyser and methanation capacities are calculated according to eq. 6.23 and the parameter ω_{PtX} in table 7.1 is calculated for each scenario from the scenario datasets (Figure 6.3,Equation 6.23). For all the independent variables, the limits are set at -50% to +50% of the median values, and sampling is done between the limits to generate random values. The energy system is then dimensioned for each of these random values, and the output parameters are calculated first as a time series in the dynamic simulation and then integrated to obtain yearly cumulative values. These results are then used to evaluate the impact of the independent variables on the output parameters. The sampling method used is Latin Hypercube Sampling [206] to generate random independent variables between the minimum and maximum, and the depth[7.2] of the Design of Experiments (DOE) is set at 10. Therefore, 10 sets of sample parameters are generated, which in turn are used to dimension the energy systems, which are then simulated.

7.2 The accuracy of the DOE can be enhanced by increasing its depth. Since simulating the process for complex energy systems is computationally expensive, only 10 values are sampled within the minimum and maximum range of parameters for each city, and higher resolutions in-between for the results are derived using interpolation.

The parameter sensitivity analyses three situations that are highly likely in future de-central energy systems:

- Case 1: Effects of scaling-up renewable capacities alone.
- Case 2: Effects of scaling-up PtX capacities for SNG or H_2 production without a corresponding scale-up of renewable capacities.
- Case 3: Effects of simultaneous scale-up of both renewable and PtX capacities.

In each of the three cases, the aim of the parameter sensitivity analysis is to determine the self-sustainability and security of supply of the energy system. A summary of the methodology used for parameter analysis is depicted in Figure 7.1, and the assumptions used are listed in table 7.1.

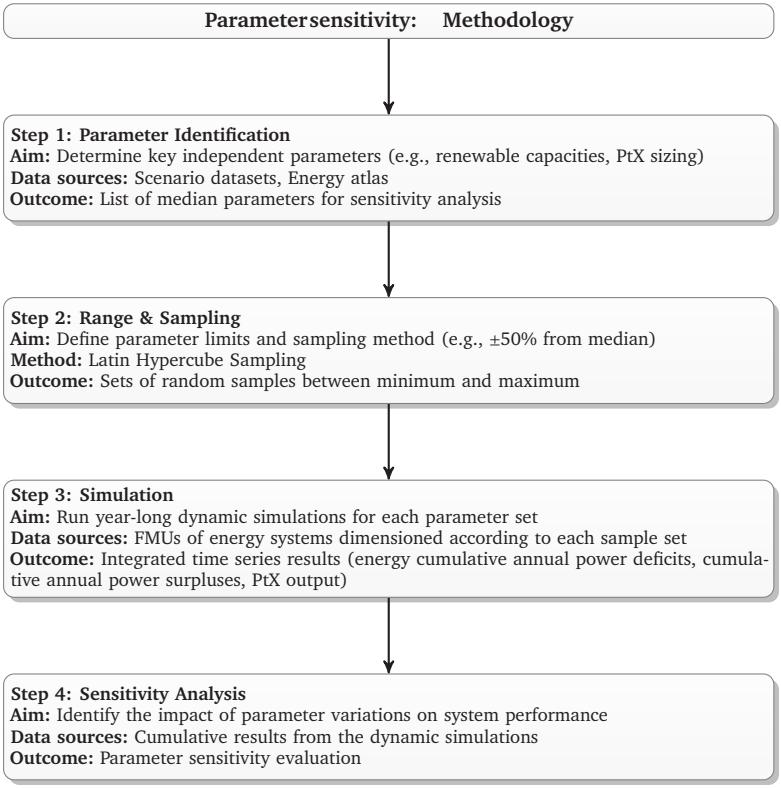

Figure 7.1: Overview of the methodology applied for parameter sensitivity analysis

Table 7.1: Assumptions used in the parameter sensitivity

Parameter	Karlsruhe	Schmallenberg
Scenario		
	BMWK-LFS-T45 (PtG/PtL)	BMWK-LFS-T45 (PtG/PtL)
Median parameters: Generation side		
$P_{\text{PV,median}}$ in GW	1.1	0.022
$P_{\text{wind,median}}$ in GW	0.00044	0.487
Median parameters: Electrolyser and Methanation capacities		
$P_{\text{ely,median}}$ in GW	$(P_{\text{wind,median}} + P_{\text{solar,median}}) \cdot \omega_{PtX}$ from eq. 6.23	
$P_{\text{met,median}}$ in GW	$(P_{\text{wind,median}} + P_{\text{solar,median}}) \cdot \omega_{PtX}$ from eq. 6.23	
Limits and depth		
Upper limit	+50% of median value for each parameter	
Lower limit	-50% of median value for each parameter	
Number of values (min-max)	10	
Case	Independent variables	Output parameter
Case 1	$(P_{\text{wind}} + P_{\text{solar}})$	$E_{\text{surp,norm}}$, ω_{SNG}
Case 2	P_{met}	$E_{\text{surp,norm}}$, ω_{SNG}
Case 3	$(P_{\text{wind}} + P_{\text{solar}}), P_{\text{met}}$	$E_{\text{surp,norm}}$, ω_{SNG}

7.4 Effects of increase in renewable capacity

A highly likely future activity involves increasing renewable wind or PV capacity, without a corresponding expansion in the capacities for H_2 or SNG production. Therefore, in the first parameter sensitivity analysis, the installed capacities of renewable wind and solar plants[7.3] alone are scaled up. The increase in the capacity of renewable power plants has two prominent effects on the de-central energy system. First, the annual power deficit is reduced as the renewable power production is higher. However, this comes at the cost of an increase in surplus power production. The general trends are the same in both cities with high wind and solar potential. As can be seen in Figure 7.2, the annual power deficit (and, as a result, grid import) decreases in all scenarios as total renewable capacity increases. However, it can also be seen that the results remain unchanged across different scenarios (Figure 7.2). This is due to the electrolyser control strategy which focuses on curtailment minimisation (Figure 4.3).

In this strategy, electrolysers only operate during power surplus hours, ensuring that any surplus power is directed to electrolysis (or methanation) rather than curtailed. As a direct consequence, electrolyser capacity remains idle during periods of power deficit, resulting in a similar reduction in grid imports in all scenarios as renewable capacity increases. This reduces the annual cumulative power deficits, but at the same time results in higher cumulative annual power surpluses (Figure 7.3), as a greater proportion of total generation is no longer used to meet existing demand.

7.3 The total renewable capacity P_{ren} (sum of wind and solar capacities) is used as a single entity in all the results. If the region has a high wind potential, P_{ren} will have a high share of wind and vice versa.

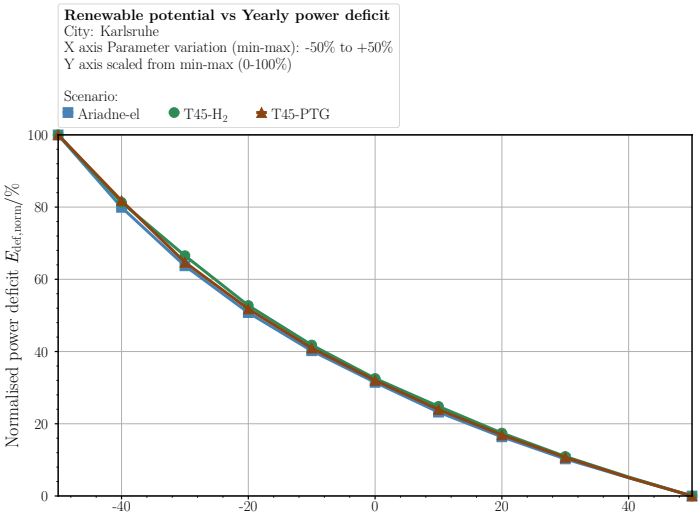

Figure 7.2: Variation of annual power deficit when only the renewable capacity increases. Y axis values normalised according to Equation 7.3.

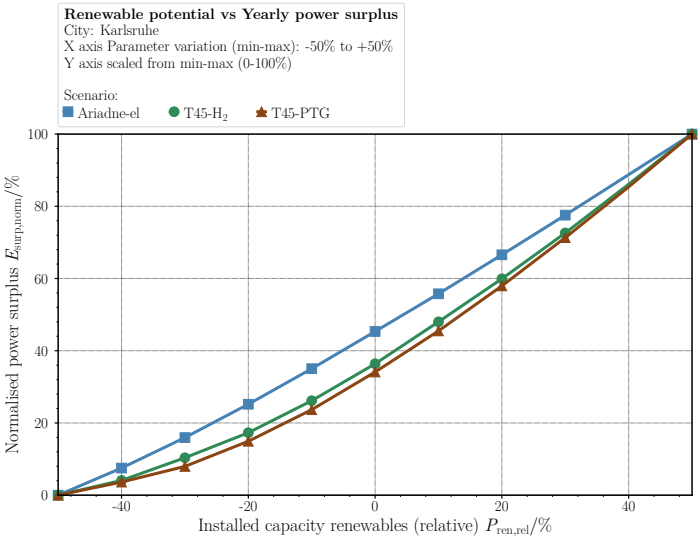

Figure 7.3: Effect of renewable capacity increase on power surplus. Y axis values normalised according to Equation 7.3.

In SNG (or H_2)-based scenarios, increasing renewable capacity increases the utilisation of existing electrolysers and methanation units, thereby increasing renewable gas production (Figure 7.4). Therefore, if PtX capacity is already in place, the amount of excess power does not scale linearly as renewable capacity expands. Instead, a non-linear pattern emerges in the cumulative annual grid feed-in (Figure 7.3), as the PtX components are still operating below their maximum capacities. The non-linear trend persists (until approximately 10% additional capacity (relative to median), as seen in Figure 7.3), after which the PtX plants operate at their full capacity. Beyond this threshold, any increase in renewable capacity results in surplus power generation that must be exported to the grid or curtailed. Therefore, the cumulative annual grid feed-increases linearly from that point.

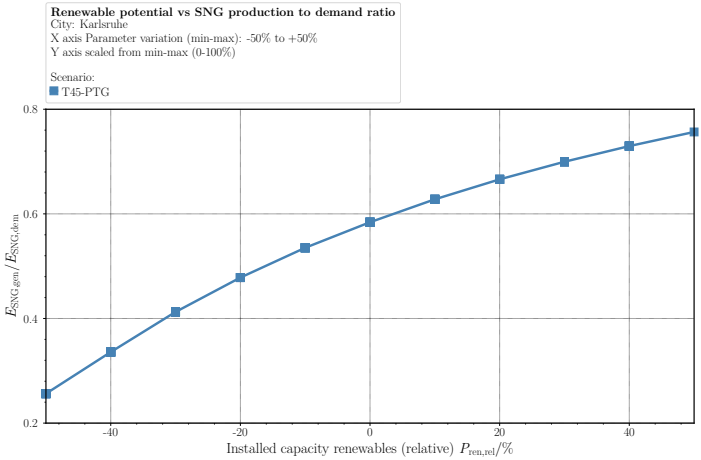

Figure 7.4: Effect of renewable capacity increase on renewable gas production.

7.5 Effect of increase in electrolysis or methanation capacities

Another future possibility is to increase the capacity of electrolysers or methanation units without a proportional increase in installed renewable capacity. This may be applicable in areas where a high installed capacity of wind or PV is already in place and the potential for further expansion is limited. Electrolysers can be used in such locations to improve the utilisation of existing renewable capacity. Expanding electrolyser capacity will result in greater use of surplus power (Figure 7.5) to produce renewable gases, resulting in less power being fed into the grid or curtailed. Figure 7.6 shows the increase in renewable gas production when methanation capacity is increased without a proportional increase in renewable capacity. A similar result is observed for all gas-based scenarios. Electrolysis capacity can be further increased until the cumulative annual power surpluses are fully utilised.

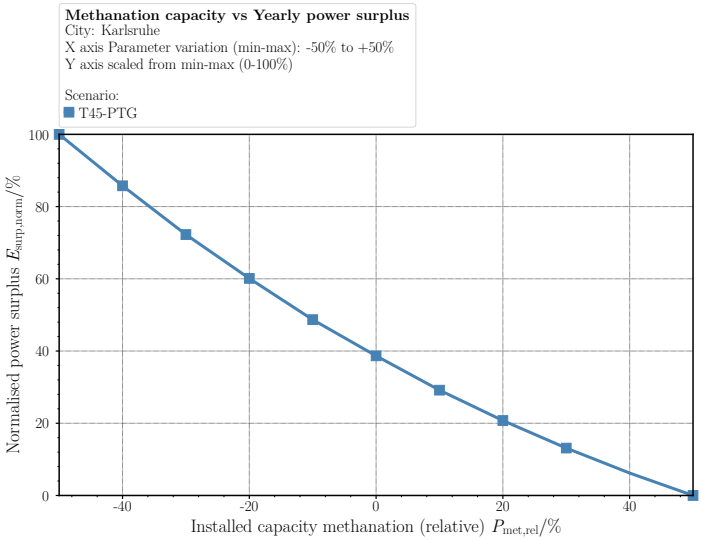

Figure 7.5: Effect on grid feed-in when increasing methanation capacities without a proportional scale-up of renewable plant capacity. Y axis values normalised according to eq. 7.3.

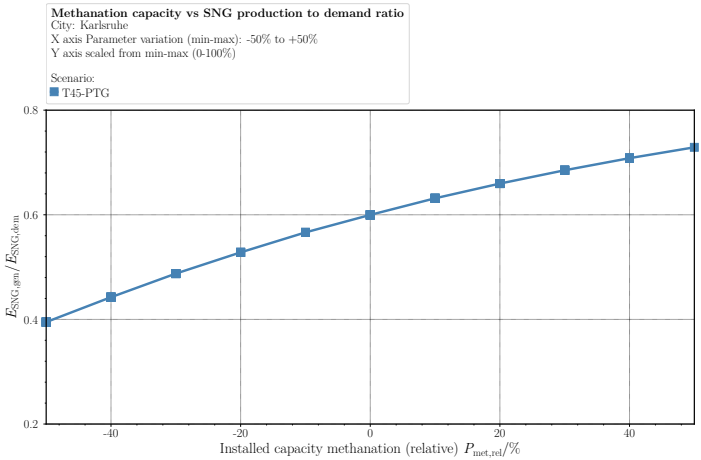

Figure 7.6: Ratio of renewable gas production to demand on increasing methanation capacities without a proportional scale-up of renewable plant capacity.

The renewable capacities used in all simulations are significantly higher than the electrolyser or methanation capacities. This allows a further expansion of PtX capacities to use the cumulative annual power surpluses. This is the reason why in (Figure 7.6) renewable gas production can be further improved.However, if a region has low installed renewable capacity, scaling up electrolyser or methanation capacity alone will not increase renewable gas production. In this case, renewable gas production does not increase because there will not be enough power surplus to run the electrolysers.

Gas production can only increase in such cases if the electrolysers are forced to operate with purchased electricity during power deficit hours. Other control strategies such as demand-side management, battery storage, or market-based electrolyser control strategies are needed to evaluate this. As the control system used in this work (Figure 4.3) is designed to operate the electrolysers only during power surplus, such possibilities are not analysed.

7.6 Proportional increase of parameters

In regions where neither renewable capacity nor PtX plants exist at present and where both are planned to be installed, the parameter sensitivity analysis can be used to evaluate how both can be scaled up proportionally. To do this, the installed capacities of renewable energy plants, electrolysers, or methanation units need to be scaled up, while ensuring that the increased renewable gas production does not lead to unused power surplus and thereby a higher chance of curtailment or grid feed-in.

The parameter sensitivity analysis in this case requires a two-dimensional variation. Two independent parameters, the installed renewable capacity (P_{ren}) and the electrolysis capacity (P_{ely}) or methanation units (P_{met}), are varied simultaneously. The objective is to determine the impact of these variations on two dependent output variables: renewable gas production and surplus power. Figure 7.7 shows that the highest gas production is achievable when the renewable capacity and the methanation capacity are at their maximum.

Looking at this result alone, it can be concluded that it is essential to simultaneously increase the capacities of both renewable energy and methanation to their maximum in order to make the energy system self-sufficient. A different perspective is obtained by examining the results from the second graph, where the z-axis represents the power surplus (Figure 7.8). Although maximising both renewable and methanation capacities maximises gas production, it also significantly increases the amount of unutilised power surplus, leading to increased grid feed-in or curtailment. This indicates a potential inefficiency in the use of resources, as a significant proportion of the surplus power generated is not used. The inference is that maximising both parameters at the same time may not always produce the best results when scaling up in regions without renewable capacities or PtX plants.

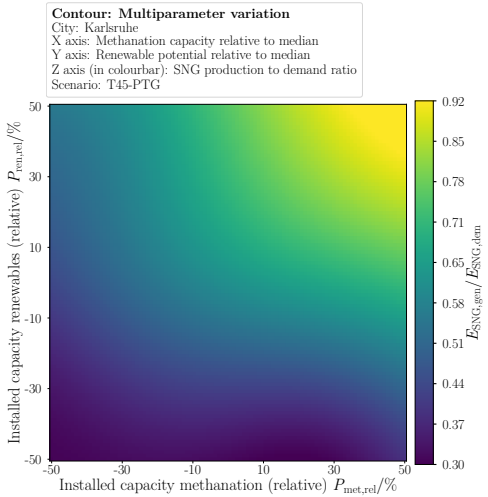

Figure 7.7: Variation in renewable gas production for simultaneous scale-up of renewable and PtX plant capacities. The resolution of the sampled region is increased using 2-D interpolation.

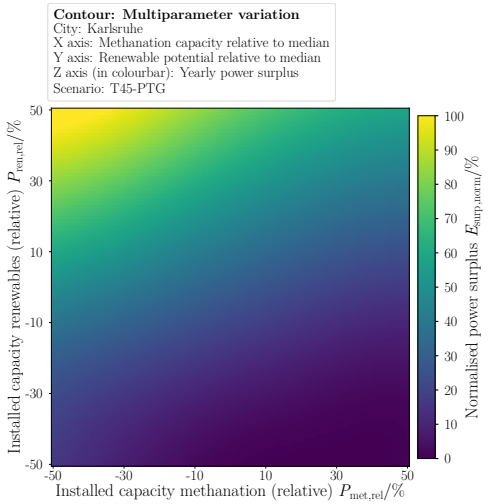

Figure 7.8: Variation in grid feed-in for simultaneous scale-up of renewable and PtX plant capacities. The resolution of the sampled region is increased using 2-D interpolation. Z values normalised according to Equation 7.3.

A more balanced approach is to scale up the renewable capacity and PtX capacities using different factors (In the case analysed in Figure 7.8, if the renewable capacity is scaled up to about 10% of its maximum value and the methanation capacity to its maximum (50% above base level), the unutilised surplus power is then reduced to almost zero, and the ratio of renewable gas production to gas demand reaches about 85% of its maximum possible value). It is not always the case that maximum capacity will produce the best results. Instead, a carefully balanced scale-up approach is required, taking into account both production and curtailment. Increasing the capacity of both renewables and electrolysers requires greater capital investment. In addition, increased use of surplus power reduces operating costs. This also suggests that an optimal scale-up strategy will also have an impact on costs. The analysis carried out in this work provides site- and scenario-specific boundary conditions that can be used for subsequent Pareto optimisation studies to minimise costs.[7.4] While many real-world constraints (e.g., pipe injection limits, grid congestion, advanced market structures) lie outside the scope of this work, the tool developed here is capable of integrating such considerations if co-simulated models of networks and markets are added.

The aim of this work is to demonstrate how parameter sensitivity, conducted on integrated results from time-resolved sector-coupled systems, yields crucial insights into security of supply and self-sufficiency under varying capacity assumptions.

7.4 An important future area that can be undertaken as a continuation of this work is economic analysis, including the impact of grid modifications or cost optimisation. The approach used in this work can refine the input parameters required for a more comprehensive economic assessment.

8 Conclusion

The goal of this work was to evaluate sector coupling in decentral energy systems using the power-to-gas process and to adapt these systems to the expected changes in future energy scenarios. To meet the goals, the methodology involved modelling the components of the energy system, combining these components into an integrated energy system, simulating the integrated system in various energy scenarios, and performing a sensitivity analysis specific to the location of the energy system. The modelling process included the integration of existing model components from the literature, such as power generation and distribution, and the development of missing components, such as the dynamic three-phase methanation model (3PM) and building energy systems.

The 3PM process was modelled using a modified axial dispersion method. The axial dispersion method was modified to include numerical adaptations to account for bubble bed expansion and thermodynamic modifications to ensure compatibility with the Modelica fluid property libraries. The impact of bubble-bed expansion on the discretisation of the balance equations was investigated and a methodology was developed to integrate the bubble-bed expansion into the numerical method. In addition, thermodynamic modifications, such as the reformulation of the balance equations in explicit derivatives of (p,h), were developed to calculate fluid properties using EOS based methods and integrate the model into Modelica. The model was validated using data obtained from dynamic load-shift experiments conducted on the 3-PM reactor at EBI-ceb. Summarising the results of dynamic validation, the model was able to reproduce general load shift trends from the experimental results with a maximum error of approximately 3% to 15% in a temperature range of 260 to 320 °C.

The building energy system models were developed and grouped on the basis of their energy source (electricity, gas or hydrogen) and type (single-family, multi-family, industrial). They were then integrated with other power generation, energy storage and PtX models.

The resulting integrated energy system could simulate dynamic behaviour over time intervals ranging from seconds to days. However, the system could not simulate networks with high spatial resolution like electricity and gas networks. To address this, a co-simulation interface was developed using the Functional Mockup Interface combined with the open-source tool Mosaik, enabling the dynamic model to be coupled with high-resolution network models. To evaluate the impact of future changes in energy systems, the model was adapted to simulate different future energy scenarios.

Multiple de-central energy systems were configured using data from different energy scenarios. The results of the short-term and long-term dynamic simulatios showed that implementing all-electric scenarios led to challenges such as surplus electricity during periods of high surplus generation and increased reliance on external grids in winter due to the simultaneous operation of multiple electric heaters. The molecule-based strategies on the other hand offered several advantages, such as long-term storage and reduced dependence on the external grid during winter.

Finally, a parameter sensitivity study was also conducted to analyse the fine-tuning required in sizing the capacities of different energy system components to achieve self-sustainability without compromising security of supply. While the de-central energy system model developed in this work effectively simulates individual regions, a comprehensive analysis at the national level requires the simulation of several regions, co-simulation of the transport and distribution networks, incorporation of dynamic fluctuations in renewable gas imports and exports, and integration of costs such as network modification costs and operating costs in each energy system. Additional factors such as greenhouse gas emissions must also be incorporated into the de-central energy system model. Nevertheless, the models developed and the insights gained in this work are an important first step in ensuring the effective implementation of gas-based sector coupling across various regions and different future energy scenarios.

A Appendix

A.1 Derivation of balance equations

The partial differential equations in concentration terms is derived by Lefebvre et al. [15] as:

$$\underbrace{\frac{\partial}{\partial t}\left(\varepsilon_{\mathrm{g}} \cdot \vec{c}_{i,\mathrm{g}}\right)}_{\text{Accumulation}} = \underbrace{\frac{\partial}{\partial z}\left(\varepsilon_{\mathrm{G}} \cdot D_{\mathrm{g,ax}} \cdot \frac{\partial \vec{c}_{i,\mathrm{g}}}{\partial z}\right)}_{\text{Axial dispersion}}$$

$$\underbrace{-\frac{\partial}{\partial z}\left(u_{\mathrm{g}} \cdot \vec{c}_{i,\mathrm{g}}\right)}_{\text{Advection}} \tag{A.1}$$

$$\underbrace{-k_{\mathrm{L}} a_i \cdot \left(\frac{\vec{c}_{i,\mathrm{g}}}{H_{i,cc}} - \vec{c}_{i,\mathrm{L}}\right)}_{\text{G/L mass transfer}}$$

To couple them to the overall energy system, the concentration terms in (Equation A.1) must be converted into mass terms with two indices: i for gas species and j for the discretised cell:

$$\vec{c}_{i,g} = \frac{\vec{m}_{i,g}}{V_{j,g}} \tag{A.2}$$

and Where $V_{j,g}$ is the volume of the gas phase in cell j. The gas holdup is defined as

$$\varepsilon_g = \frac{V_{j,g}}{V_j} \tag{A.3}$$

$$\varepsilon_{sl} = \frac{V_{j,sl}}{V_j} \tag{A.4}$$

where V_j is the total volume (j denotes the discretised cell) containing all three phases. The holdup in the slurry phase is defined as

$$\varepsilon_{sl} = 1 - \varepsilon_g \tag{A.5}$$

From eqs. A.2 to A.4, the concentration terms can be reformulated as:

$$\vec{c}_{i,g} = \frac{\vec{m}_{i,g}}{\varepsilon_g \cdot V_j} \tag{A.6}$$

and

$$\vec{c}_{i,sl} = \frac{\vec{m}_{i,sl}}{\varepsilon_{sl} \cdot V_j} \tag{A.7}$$

Substituting $\vec{c}_{i,g}$ from eq. A.5 and $\vec{c}_{i,sl}$ from eq. A.7 into A.1, the equivalent species mass balance can be derived as (with i for species and j for cell indices):

$$\underbrace{\left[\frac{1}{\varepsilon_\mathrm{g} \cdot V_j}\right]\frac{\partial}{\partial t}\left(\varepsilon_\mathrm{g} \cdot \vec{m}_{i,\mathrm{g}}\right)}_{\text{Accumulation}} = \underbrace{\left[\frac{1}{\varepsilon_\mathrm{g} \cdot V_j}\right]\frac{\partial}{\partial z}\left(\varepsilon_\mathrm{g} \cdot D_{\mathrm{g,ax}} \cdot \frac{\partial \vec{m}_{i,\mathrm{g}}}{\partial z}\right)}_{\text{Axial dispersion}}$$

$$\underbrace{-\left[\frac{1}{\varepsilon_\mathrm{g} \cdot V_j}\right]\frac{\partial}{\partial z}\left(u_\mathrm{g} \cdot \vec{m}_{i,\mathrm{g}}\right)}_{\text{Advection}}$$

$$\underbrace{-k_\mathrm{L} a_i \cdot \left(\left[\frac{1}{\varepsilon_\mathrm{g} \cdot V_j}\right]\frac{\vec{m}_{i,\mathrm{g}}}{H_{i,cc}} - \left[\frac{1}{\varepsilon_\mathrm{sl} \cdot V_j}\right]\vec{m}_{i,\mathrm{sl}}\right)}_{\text{G/L mass transfer}}$$

Which can be simplified into:

$$\underbrace{\frac{\partial \vec{m}_{i,\mathrm{g}}}{\partial t}}_{\text{Accumulation}} = \underbrace{D_{\mathrm{g,ax}}\frac{\partial^2 \vec{m}_{i,g}}{\partial z^2}}_{\text{Axial dispersion}} \underbrace{-\frac{1}{\varepsilon_g}\frac{\partial}{\partial z}\left(u_\mathrm{g} \cdot \vec{m}_{i,\mathrm{g}}\right)}_{\text{Advection}} \underbrace{-k_\mathrm{L} a_i \cdot \left(\frac{\vec{m}_{i,\mathrm{g}}}{\varepsilon_g \cdot H_{i,cc}} - \frac{\vec{m}_{i,\mathrm{sl}}}{(1-\varepsilon_g)}\right)}_{\text{G/L mass transfer}} \tag{A.8}$$

A.2 Hydrodynamic coefficients

In this work, all hydrodynamic coefficients required for the balance equations are determined using empirical correlations listed in Table A.1.

Table A.1: Hydrodynamic and kinetic relations used in the 3-PM model. Centred dots (·) indicate multiplication.

Eq. No.	Description (symbol)	Formula	Source
Eq. A.9	Superficial gas velocity (U_G)	$U_G = \dot{V}_G / A_{cs},\ A_{cs} = \pi \phi_C^2 / 4$	Lemoine et al. [134]
Eq. A.10	Bubble diameter (d_S)	$d_S = 37.19 \cdot \frac{\sigma_L^{1.22} T^{1.66}}{\rho_L^{1.52} (MW/10^3)^{0.12}} \cdot U_G^{0.14} \cdot \left(\frac{\phi_C}{\phi_C+1}\right)^{0.30} \cdot (1-\varepsilon_G)^{1.56} \cdot \Gamma^{-0.02} \cdot \exp\left[2.81 X_W + 2.77 \frac{\rho_P d_P}{1-\varepsilon_P}\right]$	Lemoine et al. [134]
Eq. A.11	Gas holdup (ε_G)	$\varepsilon_G = 4.94 \times 10^{-3} \cdot \frac{\rho_L^{0.415}}{\sigma_L^{0.27} \mu_L^{0.174}} \cdot \rho_G^{0.177} \cdot U_G^{0.553} \cdot \left(\frac{P_T}{P_T - P_S}\right)^{0.203} \cdot \left(\frac{\phi_C}{\phi_C+1}\right)^{-0.117} \cdot \Gamma^{0.053} \cdot \exp\left[-2.231\,\mathrm{CV} - 0.157 \frac{\rho_P d_P}{1-\varepsilon_P} - 0.242\zeta\right]$	Behkish et al. [133]
Eq. A.12	Sparger parameter (Γ)	$\Gamma = K_d \cdot N_O \cdot d_O^{\alpha}$	Behkish et al. [133]
Eq. A.13	Open-area ratio (ζ)	$\zeta = \frac{N_O \pi d_O^2}{4 A_{cs}} = \left(\frac{d_O}{\phi_C}\right)^2 N_O$	Behkish et al. [133]
Eq. A.14	Interfacial area (a)	$a = 6\varepsilon_G / \left[(1-\varepsilon_G) d_S\right]$	Lemoine et al. [134]
Eq. A.15	Volumetric mass-transfer ($k_L a$)	$k_L a = 6.14 \times 10^4 \frac{\rho_L^{0.26}}{\rho_G^{0.06} \sigma_L^{0.52}} \cdot \varepsilon_G^{1.21} \cdot U_G^{-0.12} \cdot d_S^{-0.05} \cdot D_{AB}^{0.50} \cdot T^{-0.68} \cdot C^{0.11} \cdot \left(\frac{\phi_C}{\phi_C+1}\right)^{0.40}$	Lemoine et al. [134]
Eq. A.16	Dimensionless Henry coefficient ($H_{i,cc}$)	$H_{i,cc} = \exp\left(A_H + B_H/T + C_H/T^2\right)$	Götz et al. [16]
Eq. A.17	Reaction rate ($r_{3\mathrm{PM}}$)	$r_{3\mathrm{PM}} = 3.90699 \times 10^5 \cdot \exp\left[-79\,061/(RT)\right] \cdot \frac{c_{\mathrm{H_2,L}}^{0.3} c_{\mathrm{CO_2,L}}^{0.1}}{(1 + c_{\mathrm{H_2O,L}})^{0.1}} \cdot K$	Lefebvre et al. [15]
Eq. A.18	Heat-transfer coefficient. (α_{eff})	$\alpha_{\mathrm{eff}} = 0.1 \cdot \left[C_{p,L} \rho_L^{3/2} \lambda_L (U_G g/\mu_L)^{1/2}\right]^{1/2}$	Deckwer [212]

The parameters used to determine the Henry's law coefficient (Equation A.16) are listed in Table A.2.

Table A.2: Henry's law fit coefficients according to Götz et al. [135].

Gases	A_H	B_H in K	C_H in K^2	Range in °C
CO_2	-2.158	609.798	-322499	25-300
H_2	-2.3838	701.147	0	100-300
CH_4	1.0697	-2856.7	708530	240-300
H_{20}	-21.325	21971	-6525600	250-290

Table A.3: Parameters and their baseline values used in this work. "In equation" gives the appearance of the variable by reference.

Symbol	Description	In equation	Range	Value used	Unit
C	Empirical constant (Lemoine)	Equation A.15	1–10	1.0	–
MW	Liquid molecular weight	Equation A.10	18–567	272	$g \cdot mol^{-1}$
K_d	Distributor constant	Equation A.12	1.00–1.55	1.36	–
N_O	Number of sparger orifices	Equations A.12 and A.13	48–1200	170	–
U_G	Superficial gas velocity	Equations A.9 to A.11, A.15 and A.18	3.5e-3–0.57	0.03	$m \cdot s^{-1}$
X_W	Primary-liquid mass fraction	Equation A.10	0.5–1.0	0.90	–
α	Sparger exponent	Equation A.12	0.015–0.65	0.50	–
ε_P	Pellet porosity	Equations A.10 and A.11	0–0.60	0.40	–
ρ_P	Catalyst particle density	Equations A.10 and A.11	700–4000	1039	$kg \cdot m^{-3}$
ϕ_C	Column diameter	Equations A.10, A.11 and A.15	0.038–7.62	0.26	m
CV	Solid volume fraction	Equation A.11	0–0.36	0.067	–
d_O	Sparger orifice diameter	Equations A.12 and A.13	0.002–0.070	0.004	m
d_P	Catalyst particle diameter	Equations A.10, A.11 and A.15	4.2e-5–3e-4	7.5e-5	m
g	Gravitational acceleration	Equation A.18	9.81 fixed	9.81	$m \cdot s^{-2}$

The superficial velocity, together with key transport properties such as density, surface tension, and dynamic viscosity, is used to evaluate the Sauter mean bubble diameter, gas holdup, gas–liquid interfacial area, and the volumetric mass-transfer coefficient. The correlations applied throughout this work consistently correspond to the small-bubble regime.

All empirical correlations for bubble diameter and volumetric mass transfer are adopted from Lemoine et al. [134], while the gas holdup relation is based on the work of Behkish et al. [133]. The Henry coefficient is calculated from Götz et al. [16] and the reaction rate is calculated using the power law equation in Lefebvre et al. [15]. The fixed parameters for equations in Table A.1 and their baseline values used in this work are listed in Table A.3.

A.3 Modelica libraries used in this work

Table A.4: Summary of libraries used in the energy system model.

Component	Parts	Source
Electrical network:	Lines, Voltage Sources, Loads, PV, Wind plants, Battery, Weather data	Modelica Buildings library [87]
Gas network:	Pipes, Valves, Storages, Junctions	TIL library [104, 213]
District heating:	Pipes, Valves, Junctions, Thermal storage	TIL library [104, 213]
Buildings:	Heat pumps, Gas Heaters, SLP	In-house
PtG system:	3-phase methanation, PtG system	In-house
Load curves:	Building SLPs, Mobility aggregated loads	BDEW [169] and Schäuble et al. [170]
Control system:	PID Control, Hysteresis control	Modelica Standard Library [214]

A.4 Python libraries used in this work

Table A.5: Summary of Python libraries used for data analysis and visualisation.

Component	Purpose	Library
Data processing:	Data manipulation, CSV handling, DataFrames	pandas [215]
Numerical computing:	Arrays, mathematical operations, linear algebra	NumPy [216]
Scientific computing:	Interpolation, optimisation	SciPy [217]
Visualisation:	Plotting, charts, figure generation	Matplotlib [218]
FMU simulation:	Functional Mock-up Units, co-simulation	FMPy [219]
Geospatial analysis:	Geographic data processing, spatial analysis	GeoPandas [220]
Network analysis:	Pipeline networks, fluid network simulation	pandapipes [221]
Data storage:	HDF5 file format, large dataset handling	h5py [222]
Parallelisation:	Distributed computing, parallel processing	Ray [204]
Weather data:	Climate data processing, EPW files	Ladybug [142]

A.5 Sample Calculation for the RMG Scenario in Karlsruhe

This worked example applies the generic allocation workflow to the gas-centred **Road-Map-Gas (RMG)** scenario for the city of Karlsruhe.

1. Data overview and assumptions

Table A.6 lists every numerical input referenced below.

Table A.6: Input parameters for the Karlsruhe-RMG case study

Parameter	Value / Comment
Generation side	
Total PV potential $P_{\text{total,PV}}$	1.10 GW
Total wind potential $P_{\text{total,Wind}}$	0.000 44 GW
Capacity-utilisation factor $\omega_{\text{cu},r}$	1.0 (full potential utilised)
PV module efficiency	18 %
Plant downtimes	Neglected
Demand side	
Annual heat demand $E_{\text{annual,heat}}$	3.0 TWh
Annual electricity demand $E_{\text{annual,el}}$	1.25 TWh
Sector split $\omega_{\text{HEF}}, \omega_{\text{HMF}}, \omega_{\text{SME}}$	0.482 / 0.280 / 0.238
Energy-carrier mix (RMG)	
District-heating share ω_{DH}	0.10
Residual 90 % split (H_2/SNG/el)	0.19 / 0.36 / 0.45
Derived factors	$\omega_{H_2} = 0.171,\ \omega_{\text{SNG}} = 0.324,\ \omega_{\text{el}} = 0.405$
DH heat production technology	CHP (fuelled by SNG or H_2)
PtX capacity formulae	
Electrolyser power P_{ely}	$\omega_{H_2} \cdot (P_{\text{PV}} + P_{\text{Wind}})$
Methanation power P_{met}	$\omega_{\text{SNG}} \cdot (P_{\text{PV}} + P_{\text{Wind}})$

2. Installed renewable capacities

The raw potentials are multiplied by the utilisation factor $\omega_{\text{cu},r} = 1$:

$$P_{\text{gen,PV}} = \omega_{\text{cu,PV}} \cdot P_{\text{total,PV}} = 1.0 \times 1.10 = 1.10\,\text{GW}, \qquad P_{\text{gen,Wind}} = 1.0 \times 0.00044 = 0.000\,44\,\text{GW}.$$

These capacities are later fed into the Modelica weather generator models to generate the dynamic profiles along with the real weather data.

3. Sector-wise annual heat demand

Applying the census-derived sector ratios to the total thermal demand:

$$E_{\text{heat,HEF}} = 3.0 \times 0.482 = 1.446\,\text{TWh},$$

$$E_{\text{heat,HMF}} = 3.0 \times 0.280 = 0.840\,\text{TWh},$$

$$E_{\text{heat,SME}} = 3.0 \times 0.238 = 0.714\,\text{TWh}.$$

Consistency check: $1.446 + 0.840 + 0.714 = 3.000$ TWh.

4. Re-allocation to energy carriers

Each sectoral figure obtained in the eariler section is then apportioned to H_2, SNG, electricity and district heating according to the normalised RMG scenario ratios:

$$\omega_{H_2} = 0.171,\ \omega_{\text{SNG}} = 0.324,\ \omega_{\text{el}} = 0.405,\ \omega_{\text{DH}} = 0.10, \qquad \sum \omega_i = 1.$$

$$E_{\text{heat-X},s} = E_{\text{heat},s} \cdot \omega_X, \qquad X \in \{H_2, \text{SNG}, \text{el}, \text{DH}\}.$$

Because $0.171 + 0.324 + 0.405 + 0.10 = 1$, the transformation is energy-conserving by construction.

5. District-heating CHP sizing

First compute the yearly heat to be delivered by the district-heating network:

$$E_{\text{DH}} = \omega_{\text{DH}} \cdot E_{\text{annual,heat}} = 0.10 \times 3.0 = 0.30\,\text{TWh}.$$

Assume the CHP runs at its *nominal* thermal power $P_{\text{DH}}^{\text{nom}}$ during a total of FLH full-load hours per year. By definition

$$\int_0^{\text{FLH}} P_{\text{DH}}^{\text{nom}}\,\mathrm{d}t = P_{\text{DH}}^{\text{nom}} \cdot \text{FLH} = E_{\text{DH}}.$$

Rearranging:

$$P_{\mathrm{DH}}^{\mathrm{nom}} = \frac{E_{\mathrm{DH}}}{\mathrm{FLH}}.$$

6. Dimensioning of PtX units

The combined renewable generation capacity is

$$P_{\mathrm{ren}} = P_{\mathrm{gen,PV}} + P_{\mathrm{gen,Wind}} = 1.10 + 0.00044 = 1.100\,44\,\mathrm{GW}.$$

Applying the carrier fractions (normalised values obtained from scenario dataset) yields

$$P_{\mathrm{ely}} = 0.171 \times 1.10044 \approx 0.188\,\mathrm{GW},$$

$$P_{\mathrm{met}} = 0.324 \times 1.10044 \approx 0.357\,\mathrm{GW}.$$

These values are starting points—later sensitivity analysis may scale them to minimise curtailment.

7. Generation of dynamic load profiles

For each sector/carrier combination the annual energy amount is converted into an hourly load curve using the BDEW standard-profile algorithm, temperature correction and weekday/weekend modifiers. A numerical check confirms that

$$\left| \frac{\int_0^{8760} P_{s,X}(t)\,\mathrm{d}t - E_{\text{heat-X},s}}{E_{\text{heat-X},s}} \right| < 5\%.$$

These time-series constitute the boundary conditions of the dynamic system simulation.

A.6 Scenario results: All scenarios

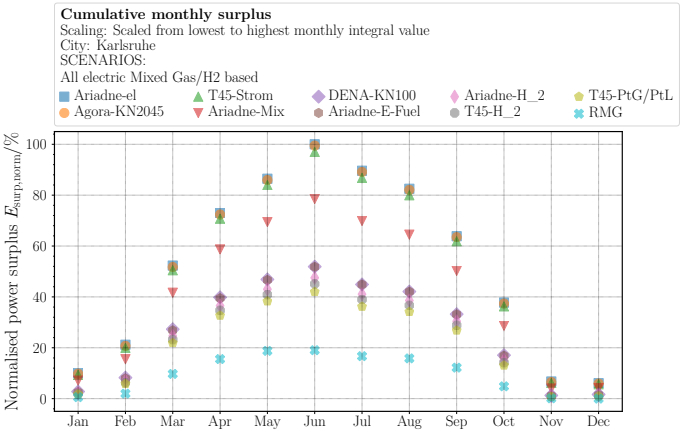

Figure A.1: Monthly integrated surplus power variations in a sunny region. Y axis values normalised according to eq. 6.27.

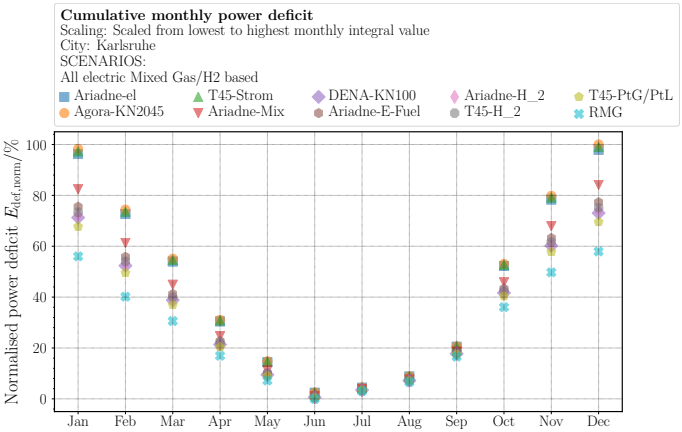

Figure A.2: Monthly integrated grid import variations in a sunny region. Y axis values normalised according to eq. 6.27.

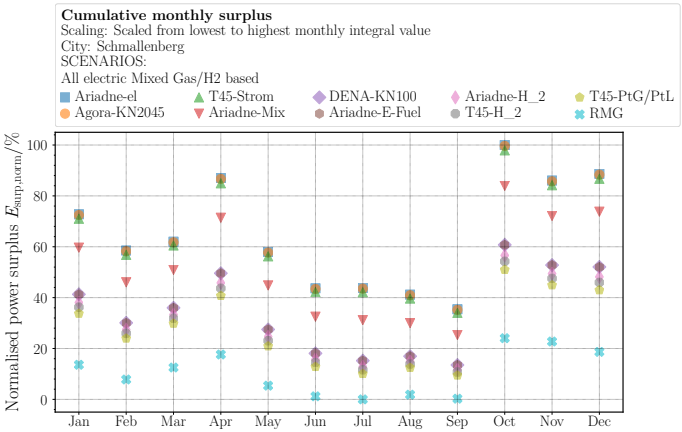

Figure A.3: Monthly integrated surplus power variations in a windy region. Y axis values normalised according to eq. 6.27.

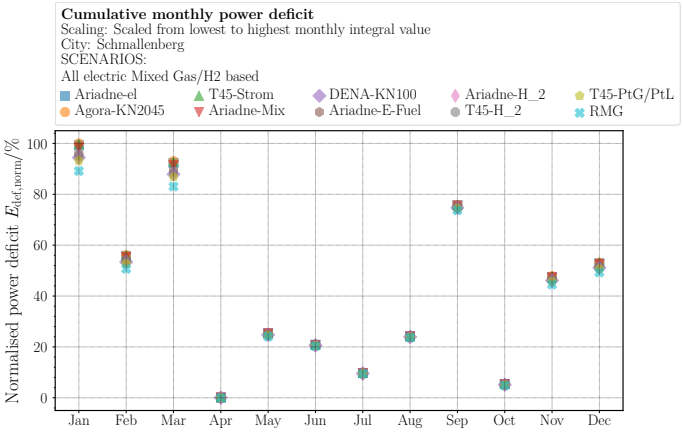

Figure A.4: Monthly integrated grid import variations in a windy region. Y axis values normalised according to eq. 6.27.

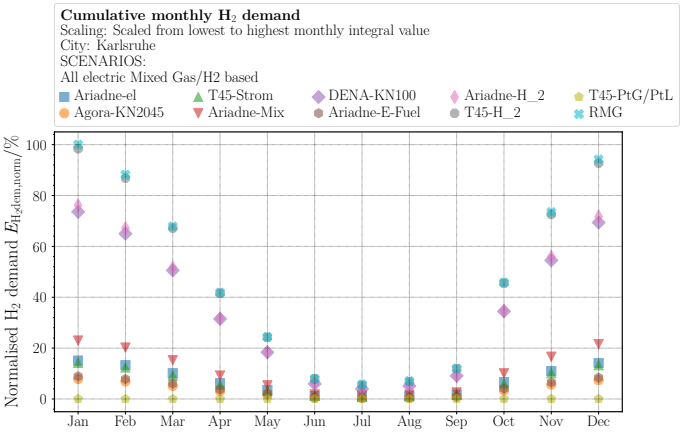

Figure A.5: Renewable H_2 demand. Y axis values normalised according to eq. 6.27.

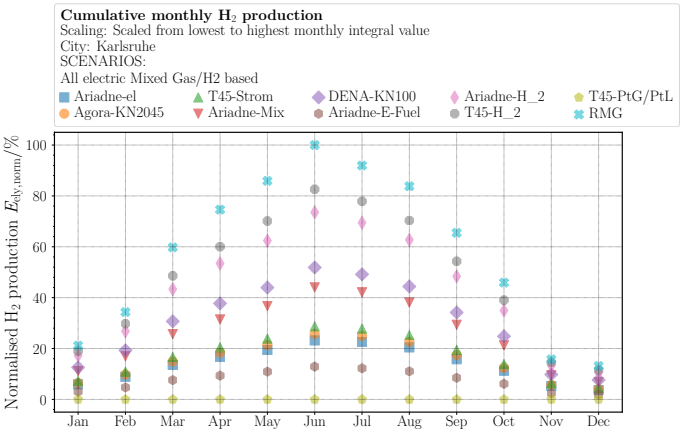

Figure A.6: Renewable H_2 production. Y axis values normalised according to eq. 6.27.

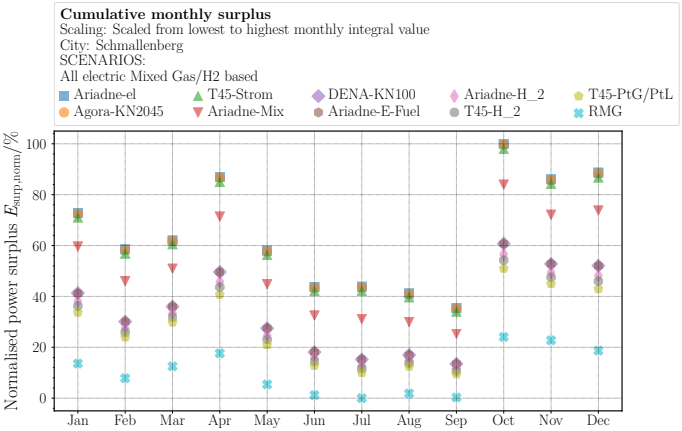

Figure A.7: Monthly integrated surplus power variations in a windy region. Y axis values normalised according to eq. 6.27.

List of Figures

List of Tables

Bibliography

[1] Jasmine Ramsebner, Reinhard Haas, Amela Ajanovic, and Martin Wietschel. The sector coupling concept: A critical review. *WIREs Energy Environ.*, 10(4), July 2021. ISSN 2041-8396, 2041-840X. doi: 10.1002/wene.396. URL https://onlinelibrary.wiley.com/doi/10.1002/wene.396.

[2] Verena Heinisch, Lisa Göransson, Rasmus Erlandsson, Henrik Hodel, Filip Johnsson, and Mikael Odenberger. Smart electric vehicle charging strategies for sectoral coupling in a city energy system. *Applied Energy*, 288:116640, 2021.

[3] Christiane Bernath, Gerda Deac, and Frank Sensfuß. Impact of sector coupling on the market value of renewable energies – a model-based scenario analysis. 281:115985.

ISSN 0306-2619. doi: 10.1016/j.apenergy.2020.115985. URL https://www.sciencedirect.com/science/article/pii/S0306261920314331.

[4] Martin Robinius, Alexander Otto, Konstantinos Syranidis, David S Ryberg, Philipp Heuser, Lara Welder, Thomas Grube, Peter Markewitz, Vanessa Tietze, and Detlef Stolten. Linking the power and transport sectors—part 2: Modelling a sector coupling scenario for germany. *Energies*, 10(7):957, 2017.

[5] T. Brown, D. Schlachtberger, A. Kies, S. Schramm, and M. Greiner. Synergies of sector coupling and transmission reinforcement in a cost-optimised, highly renewable european energy system. *Energy*, 160:720–739, 2018. ISSN 0360-5442. doi: 10.1016/j.energy.2018.06.222. URL https://www.sciencedirect.com/science/article/pii/S036054421831288X.

[6] European Technology and Innovation Platform. Sector coupling: Concepts and state-of-the-art and perspectives.

[7] Potentials of sector coupling for decarbonisation - assessing regulatory barriers in linking the gas and electricity sectors in the eu. final report. URL https://op.europa.eu/en/publication-detail/-/publication/60fadfee-216c-11ea-95ab-01aa75ed71a1/language-en.

[8] Juan Gea-Bermúdez, Ida Græsted Jensen, Marie Münster, Matti Koivisto, Jon Gustav Kirkerud, Yi-kuang Chen, and Hans Ravn. The role of sector coupling in the green transition: A least cost energy system development in northern-central europe towards 2050. 289:116685. ISSN 0306-2619. doi: 10.1016/j.apenergy.2021.116685. URL https://www.sciencedirect.com/science/article/pii/S0306261921002130.

[9] Gilbert Fridgen, Robert Keller, Marc-Fabian Körner, and Michael Schöpf. A holistic view on sector coupling. *Energy Policy*, 147:111913, 2020.

[10] Robert Schlögl. Chemical energy storage enables the transformation of fossil energy systems to sustainability. *Green Chemistry*, 23(4):1584–1593, 2021.

[11] E. van Steen and M. Claeys. Fischer-tropsch catalysts for the biomass-to-liquid (btl)-process. *Chemical Engineering & Technology*, 31(5):655–666, 2008. doi: 10.1002/ceat.200800067. URL https://onlinelibrary.wiley.com/doi/abs/10.1002/ceat.200800067.

[12] Felix Schorn, Janos L. Breuer, Remzi Can Samsun, Thorsten Schnorbus, Benedikt Heuser, Ralf Peters, and Detlef Stolten. Methanol as a renewable energy carrier: An assessment of production and transportation costs for selected global locations. *Advances in Applied Energy*, 3:100050, 2021. ISSN 2666-7924. doi: 10.1016/j.adapen.2021.100050. URL https://www.sciencedirect.com/science/article/pii/S2666792421000421.

[13] Praseeth Prabhakaran, Frank Graf, Wolfgang Koeppel, and Thomas Kolb. Modelling and validation of energy systems with dynamically operated power to gas plants for gas-based sector coupling in de-central energy hubs. *Energy Conversion and Management*, 276:116534, 2023. ISSN 0196-8904. doi: 10.1016/j.enconman.2022.116534. URL https://www.sciencedirect.com/science/article/pii/S0196890422013127.

[14] Readiness of gas infrastructure operators to safely cope with renewable gases including hydrogen. Technical report, Marcogaz, 2022. URL https://www.marcogaz.org/wp-content/uploads/2022/01/Readiness-of-gas-infrastructure-operators-to-safely-cope-with-renewable-gases-including-hydrogen.pdf.

[15] Jonathan Lefebvre, Siegfried Bajohr, and Thomas Kolb. Modelings of the transient behaviors of a slurry bubble column reactor for CO_2 methanation, and comparison with a tube bundle reactor. 151:118–136. ISSN 0960-1481. doi: 10.1016/j.renene.2019.11.008. URL http://www.sciencedirect.com/science/article/pii/S0960148119316830.

[16] Manuel Götz, Jonathan Lefebvre, Friedemann Mörs, Amy McDaniel Koch, Frank Graf, Siegfried Bajohr, Rainer Reimert, and Thomas Kolb. Renewable power-to-gas: A technological and economic review. 85:1371–1390. doi: 10.1016/j.renene.2015.07.066.

[17] Stefan Rönsch, Jens Schneider, Steffi Matthischke, Michael Schlüter, Manuel Götz, Jonathan Lefebvre, Praseeth Prabhakaran, and Siegfried Bajohr. Review on methanation – from fundamentals to current projects. *Fuel*, 166:276–296, 2016. ISSN 0016-2361. doi: 10.1016/j.fuel.2015.10.111. URL https://www.sciencedirect.com/science/article/pii/S0016236115011254.

[18] A hydrogen strategy for a climate-neutral europe. Technical report, European Commission, 2020. URL https://www.fch.europa.eu/sites/default/files/Hydrogen%20Roadmap%20Europe_Report.pdf.

[19] Hydrogen roadmap europe. a sustainable pathway for the european energy transition. Technical report, Fuel Cells and Hydrogen 2 Joint Undertaking, 2019. URL https://www.fch.europa.eu/sites/default/files/Hydrogen%20Roadmap%20Europe_Report.pdf.

[20] Andrew Chapman, Kenshi Itaoka, Katsuhiko Hirose, F. Todd Davidson, Kazunori Nagasawa, Alan C. Lloyd, Michael E. Webber, Zeynep Kurban, Shunsuke Managi, Tetsuya Tamaki, Michael C. Lewis, Robert E. Hebner, and Yasumasa Fujii. A review of four case studies assessing the potential for hydrogen penetration of the future energy system. *International Journal of Hydrogen Energy*, 44(13):6371–6382, mar 2019. doi: 10.1016/j.ijhydene.2019.01.168.

[21] The national hydrogen strategy. Technical report, Federal Ministry for Economic Affairs and Energy. URL https://www.bmwk.de/Redaktion/EN/Publikationen/Energie/the-national-hydrogen-strategy.pdf?__blob=publicationFile&v=6.

[22] Importstrategie für wasserstoff und wasserstoffderivate. URL https://www.bmwk.de/Redaktion/DE/Pressemitteilungen/2024/07/20240724-importstrategie-wasserstoff.html#:~:text=Die%20Bundesregierung%20geht%20von%20einem,Importanteil%20nach%202030%20weiter%20steigt. Accessed: 2024-08-11.

[23] Michael Steiner. Research project: Investigation of steel materials for gas pipelines and plants for assessment of their suitability with hydrogen. Technical report, Open Grid Europe, 2023. URL https://www.dvgw.de/medien/dvgw/forschung/berichte/g202006-sywesth2-steel-dvgw.pdf.

[24] Geographical analysis of biomethane potential and costs in europe in 2050. Technical report, Engie, 2021. URL https://www.engie.com/sites/default/files/assets/documents/2021-07/ENGIE_20210618_Biogas_potential_and_costs_in_2050_report_1.pdf.

[25] Alba Soler. Sustainable biomass availability in the eu towards 2050 (red ii annex ix, parts a and b). Technical report, Concawe Review, 2022.

[26] Valerie Eveloy and Tesfaldet Gebreegziabher. A Review of Projected Power-to-Gas Deployment Scenarios. *Energies*, 11(7):1824, July 2018. ISSN 1996-1073. doi: 10.3390/en11071824. URL https://www.mdpi.com/1996-1073/11/7/1824.

[27] M. Kopp, D. Coleman, C. Stiller, K. Scheffer, J. Aichinger, and B. Scheppat. Energiepark Mainz: Technical and economic analysis of the worldwide largest Power-to-Gas plant with PEM electrolysis. *International Journal of Hydrogen Energy*, 42(19):13311–13320, May 2017. ISSN 0360-3199. doi: 10.1016/j.ijhydene.2016.12.145. URL https://www.sciencedirect.com/science/article/pii/S0360319917300083.

[28] J Eichman, K Harrison, and Michael Peters. Novel electrolyzer applications: providing more than just hydrogen. Technical report, National Renewable Energy Lab.(NREL), Golden, CO (United States), 2014.

[29] Praseeth Prabhakaran, Dimitrios Giannopoulos, Wolfgang Köppel, Ushnik Mukherjee, Gopal Remesh, Frank Graf, Dimosthenis Trimis, Thomas Kolb, and Maria Founti. Cost optimisation and life cycle analysis of soec based power to gas systems used for seasonal energy storage in decentral systems. *Journal of Energy Storage*, 26:100987, 2019. ISSN 2352-152X. doi: 10.1016/j.est.2019.100987. URL https://www.sciencedirect.com/science/article/pii/S2352152X19302117.

[30] Johanna Cludius, Hauke Hermann, Felix Chr Matthes, and Verena Graichen. The merit order effect of wind and photovoltaic electricity generation in Germany 2008-2016 estimation and distributional implications. *Energy Economics*, 44(2014):302–313, 2014. ISSN 01409883. doi: 10.1016/j.eneco.2014.04.020. URL http://dx.doi.org/10.1016/j.eneco.2014.04.020.

[31] Eva Schmid, Anna Pechan, Marlene Mehnert, and Klaus Eisenack. Imagine all these futures: On heterogeneous preferences and mental models in the german energy transition. *Energy Research & Social Science*, 27:45–56, 2017. ISSN 2214-6296. doi: 10.1016/j.erss.2017.02.012. URL https://www.sciencedirect.com/science/article/pii/S2214629617300531.

[32] Marie Claire Brisbois. Decentralised energy, decentralised accountability? lessons on how to govern decentralised electricity transitions from multi-level natural resource governance. *Global Transitions*, 2:16–25, 2020. ISSN 2589-7918. doi: 10.1016/j.glt.2020.01.001. URL https://www.sciencedirect.com/science/article/pii/S2589791820300013.

[33] Maximilian Engelken, Benedikt Römer, Marcus Drescher, and Isabell Welpe. Transforming the energy system: Why municipalities strive for energy self-sufficiency. *Energy Policy*, 98:365–377, 2016. ISSN 0301-4215. doi: 10.1016/j.enpol.2016.07.049. URL https://www.sciencedirect.com/science/article/pii/S0301421516304104.

[34] Philipp Ringler, Hans Schermeyer, Manuel Ruppert, Marian Hayn, Valentin Bertsch, Dogan Keles, and Wolf Fichtner. Decentralized energy systems, market integration, optimization. Technical report, KIT, 2016.

[35] Jann Michael Weinand, Fabian Scheller, and Russell McKenna. Reviewing energy system modelling of decentralized energy autonomy. *Energy*, 203:117817, 2020. ISSN 0360-5442. doi: 10.1016/j.energy.2020.117817. URL https://www.sciencedirect.com/science/article/pii/S0360544220309245.

[36] Peter Alstone, Dimitry Gershenson, and Daniel M Kammen. Decentralized energy systems for clean electricity access. *Nature climate change*, 5(4):305–314, 2015.

[37] Md. Nasimul Islam Maruf. Sector Coupling in the North Sea Region—A Review on the Energy System Modelling Perspective. *Energies*, 12(22):4298, November 2019. ISSN 1996-1073. doi: 10.3390/en12224298. URL https://www.mdpi.com/1996-1073/12/22/4298.

[38] Arman Aghahosseini, Dmitrii Bogdanov, and Christian Breyer. Towards sustainable development in the MENA region: Analysing the feasibility of a 100% renewable electricity system in 2030. *Energy Strategy Reviews*, 28:100466, March 2020. ISSN 2211467X. doi: 10.1016/j.esr.2020.100466. URL https://linkinghub.elsevier.com/retrieve/pii/S2211467X20300201.

[39] Bernd Resch, Günther Sagl, Tobias Törnros, Andreas Bachmaier, Jan-Bleicke Eggers, Sebastian Herkel, Sattaya Narmsara, and Hartmut Gündra. Gis-based planning and modelings for renewable energy: Challenges and future research avenues. *ISPRS International Journal of Geo-Information*, 3(2):662–692, 2014. ISSN 2220-9964. doi: 10.3390/ijgi3020662. URL https://www.mdpi.com/2220-9964/3/2/662.

[40] Christina Kockel, Lars Nolting, Jan Priesmann, and Aaron Praktiknjo. Does renewable electricity supply match with energy demand? – a spatio-temporal analysis for the german case. *Applied Energy*, 308:118226, 2022. ISSN 0306-2619. doi: 10.1016/j.apenergy.2021.118226. URL https://www.sciencedirect.com/science/article/pii/S0306261921014914.

[41] Johannes Giehl, Tom Sudhaus, Ashlen Kurre, Flora v. Mikulicz-Radecki, Jeremias Hollnagel, Matthis Wacker, Jana Himmel, and Joachim Müller-Kichenbauer. Modelling the impact of the energy transition on gas distribution networks in germany. *Energy Strategy Reviews*, 38:100751, 2021. ISSN 2211-467X. doi: 10.1016/j.esr.2021.100751. URL https://www.sciencedirect.com/science/article/pii/S2211467X2100136X.

[42] Jakob Wachsmuth, Julia Michaelis, Fabian Neumann, Martin Wietschel, Vicki Duscha, Charlotte Degünther, Wolfgang Köppel, and Asif Zubair. *Roadmap Gas für die Energiewende - Nachhaltiger Klimabeitrag des Gassektors*. 2019. URL https://publica.fraunhofer.de/handle/publica/299768.

[43] Markus Reuß, Thomas Grube, Martin Robinius, and Detlef Stolten. A hydrogen supply chain with spatial resolution: Comparative analysis of infrastructure technologies in germany. *Applied Energy*, 247:438–453, 2019. ISSN 0306-2619. doi: 10.1016/j.apenergy.2019.04.064. URL https://www.sciencedirect.com/science/article/pii/S0306261919307111.

[44] International Energy Agency. *Harnessing Variable Renewables*. 2011. doi: 10.1787/9789264111394-en. URL https://www.oecd-ilibrary.org/content/publication/9789264111394-en.

[45] European Hydrogen Backbone. A european hydrogen infrastructure vision covering 28 countries, 2022. URL https://ehb.eu/files/downloads/ehb-report-220428-17h00-interactive-1.pdf.

[46] European Hydrogen Backbone. Extending the european hydrogen backbone, 2021. URL https://ehb.eu/files/downloads/European-Hydrogen-Backbone-April-2021-V3.pdf.

[47] European Hydrogen Backbone. Ehb 2023 implementation roadmap (part 1), 2023. URL https://ehb.eu/files/downloads/EHB-2023-Implementation-Roadmap-Part-1.pdf.

[48] European Commission. Repowereu plan — communication com(2022) 230 final, 2022. URL https://eur-lex.europa.eu/resource.html?format=PDF&uri=cellar:fc930f14-d7ae-11ec-a95f-01aa75ed71a1.0001.02/DOC_1.

[49] CEN-CENELEC and European Commission. Roadmap on hydrogen standardisation (ech2a/cen–cenelec), 2023. URL https://www.cencenelec.eu/media/CEN-

CENELEC/News/Press%20Releases/2023/20230301_ech2a_roadmaphydrogenstandardisation.pdf.

[50] Clean Hydrogen Partnership (FCH JU). Hydrogen valleys: Insights into the emerging hydrogen economies around the world, 2021. URL https://www.clean-hydrogen.europa.eu/system/files/2021-06/20210527_Hydrogen_Valleys_final_ONLINE.pdf.

[51] European Parliament and Council. Directive (eu) 2023/2413 on the promotion of the use of energy from renewable sources (recast), 2023. URL https://eur-lex.europa.eu/legal-content/EN/TXT/PDF/?uri=OJ:L_2023_2413.

[52] European Commission. Commission delegated regulation (eu) 2023/1184 on rfnbo rules, 2023. URL https://eur-lex.europa.eu/legal-content/EN/TXT/PDF/?uri=CELEX:32023R1184.

[53] Andrea Herbst, Felipe Toro, Felix Reitze, and Eberhard Jochem. Introduction to energy systems modelling. *Swiss journal of economics and statistics*, 148(2):111–135, 2012.

[54] Massimiliano Manfren, Paola Caputo, and Gaia Costa. Paradigm shift in urban energy systems through distributed generation: Methods and models. *Applied Energy*, 88(4): 1032–1048, 2011. ISSN 0306-2619. doi: 10.1016/j.apenergy.2010.10.018. URL https://www.sciencedirect.com/science/article/pii/S0306261910004204.

[55] Christoph Böhringer and Thomas F. Rutherford. Combining bottom-up and top-down. *Energy Economics*, 30(2):574–596, 2008. ISSN 0140-9883. doi: 10.1016/j.eneco.2007.03.004. URL https://www.sciencedirect.com/science/article/pii/S014098830700059X.

[56] Yeager Vogt PE, CEM, and MBA. Top-down energy modelings. *Strategic Planning for Energy and the Environment*, 24(1):66–80, 2004. doi: 10.1080/10485230409509656.

[57] Andrea Gatto and Carlo Drago. Measuring and modelings energy resilience. *Ecological Economics*, 172:106527, 2020. ISSN 0921-8009. doi: 10.1016/j.ecolecon.2019.106527. URL https://www.sciencedirect.com/science/article/pii/S0921800919301570.

[58] Paul E. Roege, Zachary A. Collier, James Mancillas, John A. McDonagh, and Igor Linkov. Metrics for energy resilience. *Energy Policy*, 72:249–256, 2014. ISSN 0301-4215. doi: 10.1016/j.enpol.2014.04.012. URL https://www.sciencedirect.com/science/article/pii/S0301421514002237.

[59] Anne Senkel, Carsten Bode, and Gerhard Schmitz. Quantification of the resilience of integrated energy systems using dynamic simulation. *Reliability Engineering & System Safety*, 209:107447, 2021. ISSN 0951-8320. doi: 10.1016/j.ress.2021.107447. URL https://www.sciencedirect.com/science/article/pii/S0951832021000168.

[60] Ayyoob Sharifi and Yoshiki Yamagata. Principles and criteria for assessing urban energy resilience: A literature review. *Renewable and Sustainable Energy Reviews*, 60:1654–1677, 2016. ISSN 1364-0321. doi: 10.1016/j.rser.2016.03.028. URL https://www.sciencedirect.com/science/article/pii/S136403211600263X.

[61] Hans-Kristian Ringkjøb, Peter M. Haugan, and Ida Marie Solbrekke. A review of modelling tools for energy and electricity systems with large shares of variable renewables. *Renewable and Sustainable Energy Reviews*, 96:440–459, 2018. ISSN 1364-0321. doi: 10.1016/j.rser.2018.08.002. URL https://www.sciencedirect.com/science/article/pii/S1364032118305690.

[62] David Grosspietsch, Marissa Saenger, and Bastien Girod. Matching decentralized energy production and local consumption: A review of renewable energy systems with conversion and storage technologies. *WIREs Energy and Environment*, 8(4):e336, 2019. doi: 10.1002/wene.336. URL https://wires.onlinelibrary.wiley.com/doi/abs/10.1002/wene.336.

[63] Matteo Giacomo Prina, Giampaolo Manzolini, David Moser, Benedetto Nastasi, and Wolfram Sparber. Classification and challenges of bottom-up energy system models - a review. *Renewable and Sustainable Energy Reviews*, 129:109917, 2020. ISSN 1364-0321. doi: 10.1016/j.rser.2020.109917. URL https://www.sciencedirect.com/science/article/pii/S1364032120302082.

[64] Anya Heider, Ricardo Reibsch, Philipp Blechinger, Avia Linke, and Gabriela Hug. Flexibility options and their representation in open energy modelling tools. *Energy Strategy Reviews*, 38:100737, 2021. ISSN 2211-467X. doi: 10.1016/j.esr.2021.100737. URL https://www.sciencedirect.com/science/article/pii/S2211467X2100122X.

[65] T. Brown, J. Hörsch, and D. Schlachtberger. PyPSA: Python for Power System Analysis. *Journal of Open Research Software*, 6(4), 2018. doi: 10.5334/jors.188.

[66] Leander Kotzur, Lars Nolting, Maximilian Hoffmann, Theresa Groß, Andreas Smolenko, Jan Priesmann, Henrik Büsing, Robin Beer, Felix Kullmann, Bismark Singh, Aaron Praktiknjo, Detlef Stolten, and Martin Robinius. A modeler's guide to handle complexity in energy systems optimization. *Advances in Applied Energy*, 4:100063, 2021. ISSN 2666-7924. doi: 10.1016/j.adapen.2021.100063. URL https://www.sciencedirect.com/science/article/pii/S266679242100055X.

[67] S. Lloyd. Measures of complexity: a nonexhaustive list. *IEEE Control Systems Magazine*, 21(4):7–8, 2001. doi: 10.1109/MCS.2001.939938.

[68] Paul Bachmann. *Zahlentheorie*, volume 5. Teubner, 1926.

[69] Peter Fritzson. *Principles of Object-Oriented Modelings and Simulation with Modelica 2.1*. IEEE. URL https://www.ida.liu.se/labs/pelab/modelica/OpenModelica/Documents/ModelicaBookExcerpts.pdf.

[70] François E Cellier and Ernesto Kofman. *Continuous system simulation*. Springer Science & Business Media, 2006.

[71] François E Cellier and Ernesto Kofman. *Continuous system simulation*. Springer Science & Business Media, 2006.

[72] Matthias Huber, Desislava Dimkova, and Thomas Hamacher. Integration of wind and solar power in europe: Assessment of flexibility requirements. *Energy*, 69:236–246, 2014. ISSN 0360-5442. doi: 10.1016/j.energy.2014.02.109. URL https://www.sciencedirect.com/science/article/pii/S0360544214002680.

[73] Jan Priesmann, Lars Nolting, and Aaron Praktiknjo. Are complex energy system models more accurate? an intra-model comparison of power system optimization models. *Applied Energy*, 255:113783, 2019. ISSN 0306-2619. doi: 10.1016/j.apenergy.2019.113783. URL https://www.sciencedirect.com/science/article/pii/S0306261919314709.

[74] Christoph F. Reinhart and Carlos Cerezo Davila. Urban building energy modelings – a review of a nascent field. *Building and Environment*, 97:196–202, 2016. ISSN 0360-1323. doi: 10.1016/j.buildenv.2015.12.001. URL https://www.sciencedirect.com/science/article/pii/S0360132315003248.

[75] Michael Wetter. Modelica-based modelling and simulation to support research and development in building energy and control systems. *Journal of Building Performance Simulation*, 2(2):143–161, 2009. doi: 10.1080/19401490902818259.

[76] Dirk Müller, Moritz Lauster, Ana Constantin, Marcus Fuchs, and Peter Remmen. Aixlib-an open-source modelica library within the iea-ebc annex 60 framework. *BauSIM 2016*, pages 3–9, 2016.

[77] Hassan Harb, Neven Boyanov, Luis Hernandez, Rita Streblow, and Dirk Müller. Development and validation of grey-box models for forecasting the thermal response of occupied buildings. *Energy and Buildings*, 117:199–207, 2016. ISSN 0378-7788. doi: 10.1016/j.enbuild.2016.02.021. URL https://www.sciencedirect.com/science/article/pii/S0378778816300688.

[78] Paul Strachan Georgios Kokogiannakis and Joe Clarke. Comparison of the simplified methods of the iso 13790 standard and detailed modelling programs in a regulatory context. *Journal of Building Performance Simulation*, 1(4):209–219, 2008. doi: 10.1080/19401490802509388.

[79] German Association of Engineers. Calculation of transient thermal response of rooms and buildings—modelling of rooms (vdi 6007-1), 2012.

[80] M. Lauster, J. Teichmann, M. Fuchs, R. Streblow, and D. Mueller. Low order thermal network models for dynamic simulations of buildings on city district scale. *Building and Environment*, 73:223–231, 2014. ISSN 0360-1323. doi: 10.1016/j.buildenv.2013.12.016. URL https://www.sciencedirect.com/science/article/pii/S0360132313003727.

[81] Marcus Fuchs, Jens Teichmann, Moritz Lauster, Peter Remmen, Rita Streblow, and Dirk Müller. Workflow automation for combined modelings of buildings and district energy systems. *Energy*, 117:478–484, 2016. ISSN 0360-5442. doi: 10.1016/j.energy.2016.04.023. URL https://www.sciencedirect.com/science/article/pii/S0360544216304297. The 28th International Conference on Efficiency, Cost, Optimization, Simulation and Environmental Impact of Energy Systems - ECOS 2015.

[82] Hassan Harb, Jan-Niklas Paprott, Peter Matthes, Thomas Schütz, Rita Streblow, and Dirk Müller. Decentralized scheduling strategy of heating systems for balancing the residual load. *Building and Environment*, 86:132–140, 2015. ISSN 0360-1323. doi: 10.1016/j.buildenv.2014.12.015. URL https://www.sciencedirect.com/science/article/pii/S0360132314004260.

[83] Steven Firth and Kevin Lomas. Investigating CO_2 emission reductions in existing urban housing using a community domestic energy model. *IBPSA 2009 - International Building Performance Simulation Association 2009*, 01 2009.

[84] Peter Remmen, Moritz Lauster, Michael Mans, Marcus Fuchs, Tanja Osterhage, and Dirk Mueller. Teaser: an open tool for urban energy modelling of building stocks. *Journal of Building Performance Simulation*, 11:1–15, 02 2017. doi: 10.1080/19401493.2017.1283539.

[85] Alessio Mastrucci, Olivier Baume, Francesca Stazi, Susanna Salvucci, and Ulrich Leopold. A gis-based approach to estimate energy savings and indoor thermal comfort for urban housing stock retrofitting. 01 2014.

[86] F rüdiger, F Casella, M Sielemann, et al. Standardization of thermo-fluid modelings in modelica. fluid. In *Proceedings 7th Modelica Conference*, pages 20–22, 2009.

[87] Marco Bonvini, Michael Wetter, Thierry S. Nouidui, 1Lawrence Berkeley, and National Laboratory. A modelica package for building-to-electrical grid integration. In *Fifth German-Austrian IBPSA Conference RWTH Aachen University*. IEEE.

[88] Christian Schulze. *A Contribution to Numerically Efficient Modelling of Thermodynamic Systems*. Dissertation, TU Braunschweig, 2013. URL https://publikationsserver.tu-braunschweig.de/receive/dbbs_mods_00057492?q=A%20Contribution%20to%20Numerically%20Efficient%20Modelling%20of%20Thermodynamic%20Systems.

[89] Christoph C. Richter. Proposal of new object oriented equation based model librariesfor thermodynamic systems. URL https://publikationsserver.tu-braunschweig.de/receive/dbbs_mods_00022296.

[90] Carsten Bode and Gerhard Schmitz. Influence of excess power utilization in power-to-heat units on an integrated energy system with 100 % renewables. Linköing University Electronic Press. doi: 10.3384/ecp19157413.

[91] Shalako Baggi, Davide Rivola, Davide Strepparava, and Roman Rudel. A modelica library for simulation of electrical energy storage coupled with photovoltaic systems. 2014.

[92] Max Bachmann, Yannick Fürst, Diana Stanica, and Martin Kriegel. dhcsim — a modelica library for simple modelings of complex dhc systems. *Energy Reports*, 7:294–303, 2021. ISSN 2352-4847. doi: 10.1016/j.egyr.2021.08.143. URL https://www.sciencedirect.com/science/article/pii/S2352484721007460. The 17th International Symposium on District Heating and Cooling.

[93] Queralt Altes-Buch, Sylvain Quoilin, and Vincent Lemort. Greenhouses: A modelica library for the simulation of greenhouse climate and energy systems. In *Proceedings of the 13th International Modelica Conference*. Walloon Region of Belgium - EcoSystemePass project (convention 1510610), March 2019. doi: 10.3384/ecp19157533.

[94] Willi Braun, Francesco Casella, and Bernhard Bachmann. Solving large scale modelica models: new approaches and experimental results using OpenModelica. doi: 10.3384/ecp17132557.

[95] Atiyah Elsheikh, Edmund Widl, and Peter Palensky. Simulating complex energy systems with modelica: A primary evaluation. In *2012 6th IEEE International Conference on Digital Ecosystems and Technologies (DEST)*, pages 1–6, 2012. doi: 10.1109/DEST.2012.6227921.

[96] Devendra K Chaturvedi. *Modelings and simulation of systems using MATLAB and Simulink*. CRC press, 2017.

[97] Juma Haydary. *Chemical process design and simulation: Aspen Plus and Aspen Hysys applications*. John Wiley & Sons, 2019.

[98] F. Casella and A. Leva. Object-oriented modelling and simulation of power plants with modelica. In *Proceedings of the 44th IEEE Conference on Decision and Control*, pages 7597–7602, 2005. doi: 10.1109/CDC.2005.1583388.

[99] Constantinos C. Pantelides. The consistent initialization of differential-algebraic systems. *SIAM Journal on Scientific and Statistical Computing*, 9(2):213–231, 1988. URL 10.1137/090901410.1137/0909014.

[100] Hilding Elmqvist, Martin Otter, Andrea Neumayr, and Gerhard Hippmann. Modia - equation based modelings and domain specific algorithms. In Martin Sjölund, Lena Buffoni, Adrian Pop, and Lennart Ochel, editors, *14th International Modelica Conference*, Linköping Electronic Conference Proceedings 181, pages 73–86. Linköping University Electronic Press, September 2021. URL https://elib.dlr.de/144872/.

[101] Ian H Bell, Sylvain Quoilin, Jorrit Wronski, and Vincent Lemort. Coolprop: An open-source reference-quality thermophysical property library. In *ASME ORC 2nd International Seminar on ORC Power Systems*, volume 44. sn, 2013.

[102] E. W. Lemmon, I. H. Bell, M. L. Huber, and M. O. McLinden. NIST Standard Reference Database 23: Reference Fluid Thermodynamic and Transport Properties-REFPROP, Version 10.0, National Institute of Standards and Technology, 2018. URL https://www.nist.gov/srd/refprop.

[103] Matthis Thorade, Ali Saadat, et al. Helmholtzmedia—a fluid properties library. In *Proceedings of the 9th International MODELICA Conference*, volume 10, page 3384, 2012.

[104] Til media suite, . URL https://www.tlk-thermo.com/index.php/en/tilmedia-suite/.

[105] TN Gartman, FS Sovetin, and DK Novikova. Experience in the application of the chemcad program to the modelings of reactor processes. *Theoretical Foundations of Chemical Engineering*, 43:944–954, 2009.

[106] Tadeusz Stolarski, Yuji Nakasone, and Shigeka Yoshimoto. *Engineering analysis with ANSYS software*. Butterworth-Heinemann, 2018.

[107] J Karl Johnson, John A Zollweg, and Keith E Gubbins. The lennard-jones equation of state revisited. *Molecular Physics*, 78(3):591–618, 1993.

[108] Marcia L Huber and James F Ely. A predictive extended corresponding states model for pure and mixed refrigerants including an equation of state for r134a. *International journal of refrigeration*, 17(1):18–31, 1994.

[109] R. Span, W. Wagner, E.W. Lemmon, and R.T. Jacobsen. Multiparameter equations of state — recent trends and future challenges. *Fluid Phase Equilibria*, 183-184:1–20, 2001. ISSN 0378-3812. doi: 10.1016/S0378-3812(01)00416-2. URL https://www.sciencedirect.com/science/article/pii/S0378381201004162. Proceedings of the fourteenth symposium on thermophysical properties.

[110] Francesco Casella, Martin Otterand, Katrin Proelss, Christoph Richter, and Hubertus Tummescheit. The modelica fluid and media library for modelings of incompressible and compressible thermo-fluid pipe networks. (Germany).

[111] Kai Wellner, Carsten Trapp, Gerhard Schmitz, Francesco Casella, et al. Interfacing models for thermal separation processes with fluid property data from external sources. In *10th International Modelica Conference*, pages 667–674, 2014.

[112] Matthis Thorade and Ali Saadat. Partial derivatives of thermodynamic state properties for dynamic simulation. *Environmental earth sciences*, 70:3497–3503, 2013.

[113] Jérôme Aicart, Stéphane Di Iorio, Marie Petitjean, Pascal Giroud, Géraldine Palcoux, and Julie Mougin. Transition cycles during operation of a reversible solid oxide electrolyzer/fuel cell (rsoc) system. *Fuel Cells*, 19(4):381–388, 2019.

[114] Charlotte van Leeuwen and Machiel Mulder. Power-to-gas in electricity markets dominated by renewables. *Applied Energy*, 232:258–272, 2018. ISSN 0306-2619. doi: 10.1016/j.apenergy.2018.09.217. URL https://www.sciencedirect.com/science/article/pii/S0306261918315319.

[115] Steffi Theurich, Stefan Rönsch, and Robert Güttel. Transient flow rate ramps for methanation of carbon dioxide in an adiabatic fixed-bed recycle reactor. *Energy Technology*, 8(3):1901116, 2020. doi: 10.1002/ente.201901116. URL https://onlinelibrary.wiley.com/doi/abs/10.1002/ente.201901116.

[116] Bjarne Kreitz, Jörn Brauns, Gregor D. Wehinger, and Thomas Turek. Modelings the dynamic power-to-gas process: Coupling electrolysis with CO_2 methanation. *Chemie Ingenieur Technik*, 92(12):1992–1997, 2020. doi: 10.1002/cite.202000019. URL https://onlinelibrary.wiley.com/doi/abs/10.1002/cite.202000019.

[117] Stefan Rönsch, Andreas Ortwein, and Sebastian Dietrich. Start-and-stop operation of fixed-bed methanation reactors – results from modelings and simulation. *Chemical Engineering & Technology*, 40(12):2314–2321, 2017. doi: 10.1002/ceat.201700229. URL https://onlinelibrary.wiley.com/doi/abs/10.1002/ceat.201700229.

[118] K Pedersen, A Skov, and J R Rostrup-Nielsen. Catalytic aspects of high temperature methanation. *Am. Chem. Soc., Div. Fuel Chem., Prepr.; (United States)*, 1 1979. URL https://www.osti.gov/biblio/5235839.

[119] Tanja Schaaf, Jochen Grünig, Markus Roman Schuster, Tobias Rothenfluh, and Andreas Orth. Methanation of CO_2 - storage of renewable energy in a gas distribution system. *Energy, Sustainability and Society*, 4(1):2, Dec 2014. ISSN 2192-0567. doi: 10.1186/s13705-014-0029-1.

[120] Emanuele Giglio, Raffaele Pirone, and Samir Bensaid. Dynamic modelling of methanation reactors during start-up and regulation in intermittent power-to-gas applications. *Renewable Energy*, 170:1040–1051, 2021. ISSN 0960-1481. doi: 10.1016/j.renene.2021.01.153. URL https://www.sciencedirect.com/science/article/pii/S0960148121002044.

[121] Jens Bremer and Kai Sundmacher. Operation range extension via hot-spot control for catalytic CO_2 methanation reactors. *Reaction Chemistry & Engineering*, 4(6):1019–1037, 2019.

[122] Maria Iglesias Gonzalez, Hilko Eilers, and Georg Schaub. Flexible operation of fixed-bed reactors for a catalytic fuel synthesis—CO_2 hydrogenation as example reaction. *Energy Technology*, 4(1):90–103, 2016. doi: 10.1002/ente.201500259. URL https://onlinelibrary.wiley.com/doi/abs/10.1002/ente.201500259.

[123] Marlotherm sh. URL https://www.eastman.com/en/products/product-detail?product=71114174&pn=marlotherm+sh+heat+transfer+fluid. Accessed: 2023-02-23.

[124] Duo Sun and David S.A. Simakov. Thermal management of a sabatier reactor for CO_2 conversion into CH_4: Simulation-based analysis. *Journal of* CO_2 *Utilization*, 21: 368–382, 2017. ISSN 2212-9820. doi: 10.1016/j.jcou.2017.07.015. URL https://www.sciencedirect.com/science/article/pii/S2212982016303614.

[125] Nicolaas Engelbrecht, Raymond C. Everson, and Dmitri Bessarabov. Thermal management and methanation performance of a microchannel-based sabatier reactor/heat exchanger utilising renewable hydrogen. *Fuel Processing Technology*, 208: 106508, 2020. ISSN 0378-3820. doi: 10.1016/j.fuproc.2020.106508. URL https://www.sciencedirect.com/science/article/pii/S0378382020307992.

[126] Axel Fache, Frédéric Marias, Vincent Guerré, and Stéphane Palmade. Optimization of fixed-bed methanation reactors: Safe and efficient operation under transient and steady-state conditions. *Chemical Engineering Science*, 192:1124–1137, 2018. ISSN 0009-2509. doi: 10.1016/j.ces.2018.08.044. URL https://www.sciencedirect.com/science/article/pii/S0009250918306237.

[127] Konrad L. Fischer and Hannsjörg Freund. On the optimal design of load flexible fixed bed reactors: Integration of dynamics into the design problem. *Chemical Engineering Journal*, 393:124722, 2020. ISSN 1385-8947. doi: 10.1016/j.cej.2020.124722. URL https://www.sciencedirect.com/science/article/pii/S1385894720307130.

[128] Mathias Held, Dominik Schollenberger, Simon Sauerschell, Siegfried Bajohr, and Thomas Kolb. Power-to-gas: CO_2 methanation concepts for SNG production at the engler-bunte-institut. *Chemie Ingenieur Technik*, 92(5):595–602, 2020.

[129] Simon Sauerschell, Siegfried Bajohr, and Thomas Kolb. Methanation pilot plant with a slurry bubble column reactor: Setup and first experimental results. *Energy & Fuels*, 0 (0):null, 0. doi: 10.1021/acs.energyfuels.2c00655. URL 10.1021/acs.energyfuels.2c00655.

[130] Jonathan Lefebvre, Manuel Götz, Siegfried Bajohr, Rainer Reimert, and Thomas Kolb. Improvement of three-phase methanation reactor performance for steady-state and transient operation. *Fuel processing technology*, 132:83–90, 2015.

[131] J.W.A. de Swart and R. Krishna. Simulation of the transient and steady state behaviour of a bubble column slurry reactor for fischer–tropsch synthesis. *Chemical Engineering and Processing: Process Intensification*, 41(1):35–47, 2002. ISSN 0255-2701. doi: 10.1016/S0255-2701(00)00159-8. URL https://www.sciencedirect.com/science/article/pii/S0255270100001598.

[132] Manuel Götz. *Methanisierung im Dreiphasen-Reaktor*. PhD thesis, 2014.

[133] Arsam Behkish, Romain Lemoine, Rachid Oukaci, and Badie I. Morsi. Novel correlations for gas holdup in large-scale slurry bubble column reactors operating under elevated pressures and temperatures. 115(3):157–171. ISSN 1385-8947. doi: 10.1016/j.cej.2005.10.006. URL http://www.sciencedirect.com/science/article/pii/S1385894705003633.

[134] Romain Lemoine, Arsam Behkish, Laurent Sehabiague, Yannick J. Heintz, Rachid Oukaci, and Badie I. Morsi. An algorithm for predicting the hydrodynamic and mass transfer parameters in bubble column and slurry bubble column reactors. 89(4):322–343. ISSN 0378-3820. doi: 10.1016/j.fuproc.2007.11.016. URL http://www.sciencedirect.com/science/article/pii/S0378382007002342. Special Issue in Honor of Professor Masakatsu Nomura.

[135] Manuel Götz, Felix Ortloff, Rainer Reimert, Omar Basha, Badie I. Morsi, and Thomas Kolb. Evaluation of organic and ionic liquids for three-phase methanation and biogas purification processes. *Energy & Fuels*, 27(8):4705–4716, 2013. doi: 10.1021/ef400334p.

[136] Rabya Aslam, Muhammad Hashim Khan, Muhammad Ishaq, and Karsten Müller. Thermophysical studies of dibenzyltoluene and its partially and fully hydrogenated derivatives. *Journal of Chemical & Engineering Data*, 63(12):4580–4587, Dec 2018. ISSN 0021-9568. doi: 10.1021/acs.jced.8b00652.

[137] M.C Ruzicka, J Zahradník, J Drahos, and N.H Thomas. Homogeneous–heterogeneous regime transition in bubble columns. *Chemical Engineering Science*, 56(15):4609–4626, 2001. ISSN 0009-2509. doi: 10.1016/S0009-2509(01)00116-6. URL https://www.sciencedirect.com/science/article/pii/S0009250901001166.

[138] A. C. Hindmarsh. The numerical method of lines: Integration of partial differential equations. *Mathematics of Computation*, 60(201):433–437, 1993. ISSN 00255718, 10886842. URL http://www.jstor.org/stable/2153182.

[139] C E Kees, M W Farthing, R C Berger, and T C Lackey. A review of methods for moving boundary problems. Technical report, Coastal and Hydraulics Laboratory U.S. Army Engineer Research and Development Center, 3909 Halls Ferry Road. Vicksburg, MS 39180-6199, July 2009.

[140] Adrian Bejan. *Advanced engineering thermodynamics*. John Wiley & Sons, 2016.

[141] S Wilcox and W Marion. Users manual for tmy3 data sets (revised). 5 2008. doi: 10.2172/928611. URL https://www.osti.gov/biblio/928611.

[142] Ladybug tools: Epw map. URL https://www.ladybug.tools/epwmap/. Accessed: 24-08-2024.

[143] Dymola. URL https://www.3ds.com/products/catia/dymola. Accessed: 24-08-2024.

[144] Michael Wetter, Christoph van Treeck, Lieve Helsen, Alessandro Maccarini, Dirk Saelens, Darren Robinson, and Gerald Schweiger. Ibpsa project 1: Bim/gis and modelica framework for building and community energy system design and operation–ongoing developments, lessons learned and challenges. In *Iop conference series: Earth and environmental science*, volume 323, page 012114. IOP Publishing, 2019.

[145] Filip Jorissen and Lieve Helsen. Integrated modelica model and model predictive control of a terraced house using ideas. In *https://modelica.org/events/modelica2019/subpages/modelica-conference-2019-proceedings*. Linköping University Electronic Press, 2018.

[146] Henrik Pieper, Igor Krupenski, Wiebke Brix Markussen, Torben Ommen, Andres Siirde, and Anna Volkova. Method of linear approximation of COP for heat pumps and chillers based on thermodynamic modelling and off-design operation. *Energy*, 230:120743, sep 2021. doi: 10.1016/j.energy.2021.120743.

[147] Z.Y. Xu, J.T. Gao, Bin Hu, and R.Z. Wang. Multi-criterion comparison of compression and absorption heat pumps for ultra-low grade waste heat recovery. *Energy*, 238:121804, jan 2022. doi: 10.1016/j.energy.2021.121804.

[148] Jiubing Shen, Ting Guo, Yafen Tian, and Ziwen Xing. Design and experimental study of an air source heat pump for drying with dual modes of single stage and cascade cycle. *Applied Thermal Engineering*, 129:280–289, 2018. ISSN 1359-4311. doi: 10.1016/j.applthermaleng.2017.10.047. URL https://www.sciencedirect.com/science/article/pii/S1359431117339078.

[149] Marcel Ulrich Ahrens, Sverre Stefanussen Foslie, Ole Marius Moen, Michael Bantle, and Trygve Magne Eikevik. Integrated high temperature heat pumps and thermal storage tanks for combined heating and cooling in the industry. *Applied Thermal Engineering*, 189:116731, may 2021. doi: 10.1016/j.applthermaleng.2021.116731.

[150] Mateo Jesper, Florian Schlosser, Felix Pag, Timothy Gordon Walmsley, Bastian Schmitt, and Klaus Vajen. Large-scale heat pumps: Uptake and performance modelling of market-available devices. *Renewable and Sustainable Energy Reviews*, 137:110646, 2021. ISSN

1364-0321. doi: 10.1016/j.rser.2020.110646. URL https://www.sciencedirect.com/science/article/pii/S1364032120309308.

[151] David Fischer, Tobias Wolf, Jeannette Wapler, Raphael Hollinger, and Hatef Madani. Model-based flexibility assessment of a residential heat pump pool. *Energy*, 118:853–864, 2017. ISSN 0360-5442. doi: 10.1016/j.energy.2016.10.111. URL https://www.sciencedirect.com/science/article/pii/S0360544216315572.

[152] Oliver Ruhnau, Lion Hirth, and Aaron Praktiknjo. Time series of heat demand and heat pump efficiency for energy system modelings. *Scientific Data*, 6(1), oct 2019. doi: 10.1038/s41597-019-0199-y.

[153] Esa Kari Vakkilainen. 3 - boiler processes. In Esa Kari Vakkilainen, editor, *Steam Generation from Biomass*, pages 57–86. Butterworth-Heinemann, 2017. ISBN 978-0-12-804389-9. doi: 10.1016/B978-0-12-804389-9.00003-4. URL https://www.sciencedirect.com/science/article/pii/B9780128043899000034.

[154] Dries Haeseldonckx and William D'haeseleer. The use of the natural-gas pipeline infrastructure for hydrogen transport in a changing market structure. *International Journal of Hydrogen Energy*, 32(10):1381–1386, 2007. ISSN 0360-3199. doi: 10.1016/j.ijhydene.2006.10.018. URL https://www.sciencedirect.com/science/article/pii/S0360319906004940. EHEC2005.

[155] Worcester bosch. the future of fuel; version: 2018. URL https://www.worcester-bosch.co.uk/img/documents/hydrogen/The_Future_of_Fuel.pdf. Version 2018.

[156] Fraunhofer institute for systems and innovation research (isi). enertile. version: November 07, 2019. URL https://www.enertile.eu/enertile-en/index.php. Version 2019.

[157] Jamie Speirs, Paul Balcombe, Erin Johnson, Jeanne Martin, Nigel Brandon, and Adam Hawkes. A greener gas grid: What are the options. *Energy Policy*, 118:291–297, 2018. ISSN 0301-4215. doi: 10.1016/j.enpol.2018.03.069. URL https://www.sciencedirect.com/science/article/pii/S0301421518302027.

[158] M. Jangsten, J. Kensby, J.-O. Dalenbäck, and A. Trüschel. Survey of radiator temperatures in buildings supplied by district heating. *Energy*, 137:292–301, oct 2017. doi: 10.1016/j.energy.2017.07.017.

[159] Mei Gong and Sven Werner. Exergy analysis of network temperature levels in swedish and danish district heating systems. *Renewable Energy*, 84:106–113, dec 2015. doi: 10.1016/j.renene.2015.06.001.

[160] Jochen Linssen, Peter Stenzel, and Johannes Fleer. Techno-economic analysis of photovoltaic battery systems and the influence of different consumer load profiles. *Applied Energy*, 185:2019–2025, jan 2017. doi: 10.1016/j.apenergy.2015.11.088.

[161] Valentin Bertsch, Jutta Geldermann, and Tobias Lühn. What drives the profitability of household PV investments, self-consumption and self-sufficiency? *Applied Energy*, 204: 1–15, oct 2017. doi: 10.1016/j.apenergy.2017.06.055.

[162] Open power system data, data package time series. version 2017-07-09. URL https://data.open-power-system-data.org/time_series/2017-07-09. Version 2017-07-09.

[163] European transmission system operators, country-specific hourly load data. URL https://www.entsoe.eu/data/data-portal/consumption/. Version 2011.

[164] Noah Pflugradt, Jens Teuscher, Bernd Platzer, and Wolfgang Schufft. Analysing low-voltage grids using a behaviour based load profile generator. In *International conference on renewable energies and power quality*, volume 11, page 5, 2013.

[165] Theresa Müller and Dominik Möst. Demand response potential: Available when needed? *Energy Policy*, 115:181–198, apr 2018. doi: 10.1016/j.enpol.2017.12.025.

[166] Vdi 4655 - reference load profiles of single-family and multi-family houses for the use of chp systems. URL https://books.google.co.in/books?id=MAcjswEACAAJ.

[167] Open power system data, when2heat heating profiles version 2019-08-06. Version 2019-08-06.

[168] BDEW Bundesverband der Energie- und Wasserwirtschaft. 20240322_lf_slp_gas_kov_xiv_final_clean. https://www.bdew.de/media/documents/20240322_LF_BKM_Gas_Teil1_KoV_XIV_final_clean_ARXhpZW.pdf, 2024. Gas standard load profiles and parameters (KoV XIV, Teil 1).

[169] Standard lastprofile strom bdew. URL https://www.bdew.de/energie/standardlastprofile-strom/.

[170] Johannes Schäuble, Thomas Kaschub, Axel Ensslen, Patrick Jochem, and Wolf Fichtner. Generating electric vehicle load profiles from empirical data of three ev fleets in southwest germany. *Journal of Cleaner Production*, 150:253–266, 2017. ISSN 0959-6526. doi: 10.1016/j.jclepro.2017.02.150. URL https://www.sciencedirect.com/science/article/pii/S0959652617303761.

[171] Clemens Düpmeier, Karl-Uwe Stucky, Ralf Mikut, and Veit Hagenmeyer. A concept for the control, monitoring and visualization center in energy lab 2.0. In Sebastian Gottwalt, Lukas König, and Hartmut Schmeck, editors, *Energy Informatics*, pages 83–94, Cham, 2015. Springer International Publishing. ISBN 978-3-319-25876-8.

[172] Hüseyin Cakmak, Anselm Erdmann, Michael Kyesswa, Uwe Kühnapfel, and Veit Hagenmeyer. A new distributed co-simulation architecture for multi-physics based energy

systems integration. *Automatisierungstechnik*, 67(11):972–983, 2019. ISSN 2196-677X, 0178-2312. doi: 10.1515/auto-2019-0081.

[173] Anselm Erdmann, Hüseyin K. Çakmak, Uwe Kuhnapfel, and Veit Hagenmeyer. A new communication concept for efficient configuration of energy systems integration co-simulation. In *2019 IEEE/ACM 23rd International Symposium on Distributed Simulation and Real Time Applications (DS-RT)*, page 8 Seiten. Institute of Electrical and Electronics Engineers (IEEE), 2019. ISBN 978-1-72812-923-5. doi: 10.1109/DS-RT47707.2019.8958665.

[174] Anselm Erdmann, Anna Marcellan, Dominik Hering, Michael Suriyah, Carolin Ulbrich, Martin Henke, André Xhonneux, Dirk Müller, Rutger Schlatmann, and Veit Hagenmeyer. On verification of designed energy systems using distributed co-simulations. In *2020 IEEE/ACM 24th International Symposium on Distributed Simulation and Real Time Applications (DS-RT)*, pages 25–32. Institute of Electrical and Electronics Engineers (IEEE), 2020. ISBN 978-1-72817-343-6. doi: 10.1109/DS-RT50469.2020.9213689.

[175] Veit Hagenmeyer, Hüseyin Kemal Cakmak, Clemens Düpmeier, Timm Faulwasser, Jörg Isele, Hubert B. Keller, Peter Kohlhepp, Uwe Kühnapfel, Uwe Stucky, Simon Waczowicz, and Ralf Mikut. Information and communication technology in energy lab 2.0: Smart energies system simulation and control center with an open-street-map-based power flow simulation example. *Energy Technology*, 4(1):145–162, 2016. ISSN 2194-4288. doi: 10.1002/ente.201500304. 37.98.10; LK 01.

[176] Tobias Kornrumpf, Jan Meese, Markus Zdrallek, Nils Neusel-Lange, and Marvin Roch. Economic dispatch of flexibility options for grid services on distribution level. In *2016 Power Systems Computation Conference (PSCC)*, pages 1–7, 2016. doi: 10.1109/PSCC.2016.7540836.

[177] Zhongkai Yi, Yinliang Xu, Jiefeng Hu, Mo-Yuen Chow, and Hongbin Sun. Distributed, neurodynamic-based approach for economic dispatch in an integrated energy system. *IEEE Transactions on Industrial Informatics*, 16(4):2245–2257, 2020. doi: 10.1109/TII.2019.2905156.

[178] Min Jae Kim, Tong Seop Kim, Robert J. Flores, and Jack Brouwer. Neural-network-based optimization for economic dispatch of combined heat and power systems. *Applied Energy*, 265:114785, 2020. ISSN 0306-2619. doi: 10.1016/j.apenergy.2020.114785. URL https://www.sciencedirect.com/science/article/pii/S030626192030297X.

[179] Naveed Ahmed Khan, Guftaar Ahmad Sardar Sidhu, and Feifei Gao. Optimizing combined emission economic dispatch for solar integrated power systems. *IEEE Access*, 4: 3340–3348, 2016.

[180] Shuiying Liang and Jing Zhu. Dynamic economic dispatch of microgrid with biomass power generation. In *Proceedings of the 2017 6th International Conference on Energy and*

Environmental Protection (ICEEP 2017), pages 635–645. Atlantis Press, 2017/06. ISBN 978-94-6252-392-0. doi: 10.2991/iceep-17.2017.113.

[181] Gui-Xiong He, Hua guang Yan, Lei Chen, and Wen-Quan Tao. Economic dispatch analysis of regional electricity–gas system integrated with distributed gas injection. *Energy*, 201:117512, 2020. ISSN 0360-5442. doi: 10.1016/j.energy.2020.117512. URL https://www.sciencedirect.com/science/article/pii/S0360544220306198.

[182] Guoqing Li, Rufeng Zhang, Tao Jiang, Houhe Chen, Linquan Bai, and Xiaojing Li. Security-constrained bi-level economic dispatch model for integrated natural gas and electricity systems considering wind power and power-to-gas process. *Applied Energy*, 194:696–704, 2017. ISSN 0306-2619. doi: 10.1016/j.apenergy.2016.07.077. URL https://www.sciencedirect.com/science/article/pii/S0306261916310194.

[183] Soheil Derafshi Beigvand, Hamdi Abdi, and Massimo La Scala. Economic dispatch of multiple energy carriers. *Energy*, 138:861–872, 2017. ISSN 0360-5442. doi: 10.1016/j.energy.2017.07.108. URL https://www.sciencedirect.com/science/article/pii/S0360544217312860.

[184] Liangce He, Zhigang Lu, Lijun Geng, Jiangfeng Zhang, Xueping Li, and Xiaoqiang Guo. Environmental economic dispatch of integrated regional energy system considering integrated demand response. *International Journal of Electrical Power and Energy Systems*, 116:105525, 2020. ISSN 0142-0615. doi: 10.1016/j.ijepes.2019.105525. URL https://www.sciencedirect.com/science/article/pii/S0142061519315352.

[185] Jörn Benthin, Annika Heyer, Philipp Huismann, Michael Djukow, Anne Hagemeier, and Klaus Görner. Demand oriented modelling of coupled energy grids. In *Proceedings of the 13th International Modelica Conference, Regensburg, Germany, March 4–6, 2019*, number 157. Linköping University Electronic Press, 2019.

[186] Carsten Bode. *Simulation of integrated energy systems with a focus on gas grids and heating technologies*. doctoralthesis, Technische Universität Hamburg, 2022. URL http://hdl.handle.net/11420/11769.

[187] A. Loewen. *Entwicklung eines Verfahrens zur Aggregation komplexer Fernwärmenetze*. UMSICHT-Schriftenreihe. Fraunhofer-IRB-Verlag, 2001. ISBN 9783816759096. URL https://books.google.de/books?id=igYVtwAACAAJ.

[188] Helge V. Larsen, Halldór Pálsson, Benny Bøhm, and Hans F. Ravn. Aggregated dynamic simulation model of district heating networks. *Energy Conversion and Management*, 43 (8):995–1019, 2002. ISSN 0196-8904. doi: 10.1016/S0196-8904(01)00093-0. URL https://www.sciencedirect.com/science/article/pii/S0196890401000930.

[189] Andrea Bartolini, Francesco Casella, Adrien Guironnet, et al. Towards pan-european power grid modelling in modelica: Design principles and a prototype for a reference

power system library. In *LINKÖPING ELECTRONIC CONFERENCE PROCEEDINGS*, volume 157, pages 627–636, 2019.

[190] Fuctional mock-up interface standard website. URL https://fmi-standard.org/. Accessed: 2023-02-19.

[191] Steffen Schütte, Stefan Scherfke, and Martin Tröschel. Mosaik: A framework for modular simulation of active components in smart grids. In *2011 IEEE First International Workshop on Smart Grid Modelings and Simulation (SGMS)*, pages 55–60. IEEE, 2011.

[192] Leon Thurner, Alexander Scheidler, Florian Schäfer, Jan-Hendrik Menke, Julian Dollichon, Friederike Meier, Steffen Meinecke, and Martin Braun. pandapower—an open-source python tool for convenient modelings, analysis, and optimization of electric power systems. *IEEE Transactions on Power Systems*, 33(6):6510–6521, 2018.

[193] Johannes Ruf, Martin Zimmerlin, Patrick S Sauter, Wolfgang Köppel, Michael R Suriyah, Mathias Kluwe, Sören Hohmann, Thomas Leibfried, and Thomas Kolb. Simulation framework for multi-carrier energy systems with power-to-gas and combined heat and power. In *2018 53rd International Universities Power Engineering Conference (UPEC)*, pages 1–6. IEEE, 2018.

[194] S. Steinle, J. Ruf, L. Vayas, V. Isik, J. Mohan, P. Jané-Soneira, A. J. Malan, R. Küchlin, S. Sauerschell, L. Herold, J. Walter, M. R. Suriyah, S. Bajohr, T. Kern, T. Kolb, S. Hohmann, W. Köppel, and T. Leibfried. Das verbundprojekt regenzell: Zellenübergreifende regionalisierung der energieversorgung durch betriebsoptimierte sektorenkopplung. In *ETG-Kongress 2021: das Gesamtsystem im Fokus der Energiewende : 18.–19. Mai 2021, Online*, pages 124–129. VDE Verlag, 2021. ISBN 978-3-8007-5549-3.

[195] Langfristszenarien 3. URL https://www.langfristszenarien.de/enertile-explorer-en/https://www.bdew.de/energie/standardlastprofile-strom/.

[196] Kopernikus ariadne szenarien. URL https://ariadneprojekt.de/themen/szenarien-pfade/.

[197] Agora klimaneutrales deutschland 2045. URL https://www.agora-energiewende.de/veroeffentlichungen/klimaneutrales-deutschland-2045/.

[198] Dena leitstudie. URL https://www.dena.de/newsroom/meldungen/dena-leitstudie-aufbruch-klimaneutralitaet/. Accessed: 2022-03-04.

[199] Road map gas. URL https://www.dvgw.de/themen/forschung-und-innovation/energieforschung/roadmap-gas-2050. Accessed: 2022-03-04.

[200] Energieatlas baden-württemberg, . URL https://www.energieatlas-bw.de. Accessed: 2024-08-11.

[201] Energieatlas nrw, . URL https://www.energieatlas.nrw.de/site. Accessed: 2024-08-11.

[202] Der energieleitplan der stadt karlsruhe. URL https://www.karlsruhe.de/umwelt-klima/klimaschutz-klimaanpassung/klimaschutzaktivitaeten/energieleitplan. Accessed: 2024-08-11.

[203] Zensus 2022. URL https://www.zensus2022.de/EN/Home/_node.html. Accessed: 2024-08-11.

[204] Philipp Moritz, Robert Nishihara, Stephanie Wang, Alexey Tumanov, Richard Liaw, Eric Liang, Melih Elibol, Zongheng Yang, William Paul, Michael I. Jordan, and Ion Stoica. Ray: a distributed framework for emerging ai applications. In *Proceedings of the 13th USENIX Conference on Operating Systems Design and Implementation*, OSDI'18, page 561–577, USA, 2018. USENIX Association. ISBN 9781931971478.

[205] K Vanaja and RH Shobha Rani. Design of experiments: concept and applications of plackett burman design. *Clinical research and regulatory affairs*, 24(1):1–23, 2007.

[206] Felipe AC Viana. A tutorial on latin hypercube design of experiments. *Quality and reliability engineering international*, 32(5):1975–1985, 2016.

[207] Iea: Electricity security. URL https://www.iea.org/reports/power-systems-in-transition/electricity-security-matters-more-than-ever. Accessed: 2023-02-16.

[208] Carlos M. Correa-Posada and Pedro Sánchez-Martín. Integrated power and natural gas model for energy adequacy in short-term operation. *IEEE Transactions on Power Systems*, 30(6):3347–3355, 2015. doi: 10.1109/TPWRS.2014.2372013.

[209] Y. M. Atwa, E. F. El-Saadany, and Anne-Claire Guise. Supply adequacy assessment of distribution system including wind-based dg during different modes of operation. *IEEE Transactions on Power Systems*, 25(1):78–86, 2010. doi: 10.1109/TPWRS.2009.2030282.

[210] M.V. Pereira, L.A. Barroso, and J. Rosenblatt. Supply adequacy in the brazilian power market. In *IEEE Power Engineering Society General Meeting, 2004.*, pages 1016–1021 Vol.1, 2004. doi: 10.1109/PES.2004.1372991.

[211] Bo Zeng, Geng Wu, Jianhui Wang, Jianhua Zhang, and Ming Zeng. Impact of behaviors-driven demand response on supply adequacy in smart distribution systems. *Applied Energy*, 202:125–137, 2017. ISSN 0306-2619. doi: 10.1016/j.apenergy.2017.05.098. URL https://www.sciencedirect.com/science/article/pii/S0306261917306025.

[212] W.-D. Deckwer. On the mechanism of heat transfer in bubble column reactors. 35 (6):1341–1346. ISSN 0009-2509. doi: 10.1016/0009-2509(80)85127-X. URL http://www.sciencedirect.com/science/article/pii/000925098085127X.

[213] Til library, . URL https://www.tlk-thermo.com/index.php/en/til-suite.

[214] Modelica standard library. URL https://github.com/modelica/ModelicaStandardLibrary.

[215] pandas: powerful data structures for data analysis, time series, and statistics. https://pandas.pydata.org/, .

[216] Numpy: The fundamental package for scientific computing with python. https://numpy.org/.

[217] Scipy: Scientific computing tools for python. https://scipy.org/.

[218] Matplotlib: Visualization with python. https://matplotlib.org/.

[219] Fmpy: Simulate functional mockup units (fmus) in python. https://github.com/CATIA-Systems/FMPy.

[220] Geopandas: Python tools for geographic data. https://geopandas.org/.

[221] pandapipes: An open source piping grid calculation package. https://www.pandapipes.org/, .

[222] Hdf5 for python. https://www.h5py.org/.